

# **Experimental Investigation of Propeller Wake Velocity Field**

by

© Mohammad Asif Amin

A thesis submitted to the School of Graduate Studies  
in partial fulfillment of the requirements for the degree of

**Master of Engineering**

**Faculty of Engineering and Applied Science**

Memorial University of Newfoundland

**May 2018**

St. John's

Newfoundland

Canada

## **ABSTRACT**

Propeller wake wash has been used as an operational ice management technique for many years, particularly in managing small and medium sizes ice floes in arctic and sub-arctic regions. Propeller wake wash is a complicated flow with axial, tangential and radial components of velocity. The jet velocity of a wash has a significant component that is directed upwards towards the free surface of the water. The component of the jet interacting with a free surface of water can be used for ice management, and this is of practical interest for the present investigation.

The current study is an experiment on the propeller wake velocity field to investigate the influence of factors affecting propeller wake wash. The experiment was done on a steady wake wash, in the absence of ice, to measure fluid velocity components downstream of the propeller. The investigation was done by varying the major factors affecting propeller wake wash, which were: the power delivered by the propeller, the inclination of the propeller, and the depth of submergence of the propeller. The power delivered by the propeller was measured as propeller shaft rotational speed. The response variables of interest were the mean velocity in the wake, the spatial distribution of velocity, and the variability of the wake flow. The experiment was designed by following the Central Composite Design (CCD) of Response Surface methodology, testing at five levels for each of the three factors. All the experimental data, and the results that were analyzed, are presented in an OERC test report (Amin et al., 2017), and in this thesis.

Dedicated to  
my parents  
and  
my wife

## **ACKNOWLEDGEMENTS**

First and foremost, I would like to thank the almighty God to provide me the intellectual capability and good health throughout the period of the Master's study to carry out this research. Then I express my heartiest gratitude to my research supervisors, Dr. Bruce Colbourne and Dr. Brian Veitch for their valued guidance, support, and motivation throughout the MEng program. Without their support this research work would not have been possible. Next I would like to thank the technicians of OERC (Ocean Engineering Research Centre) at Memorial University to help me to a great extent to do the commissioning of the equipment, and to run the experiment, particularly Mr. Matt Curtis and Mr. Trevor Clark. I also would like to extend my gratitude to Dr. Leonard Lye for having valuable discussions in designing the experiment.

I would like to render my gratitude to Dr. Brian Veitch, to provide me the opportunity to do an internship with HETC (Harsh Environment Technology Center) of ABS (American Bureau of Shipping), which was a very good learning experience too.

Above all, I owe my deepest thanks to my wife and my parents for their unconditional love, inspiration, and patience during my studies. Without my wife's longstanding inspiration and cordial support by accompanying me in Canada, it would be difficult for me to carry out the research smoothly.

# TABLE OF CONTENTS

ABSTRACT .....	ii
ACKNOWLEDGEMENTS .....	iv
TABLE OF CONTENTS .....	v
List of Tables .....	viii
List of Figures .....	ix
NOMENCLATURE AND ABBREVIATIONS .....	xvi
CHAPTER 1 - INTRODUCTION .....	1
1.1 Literature Review .....	1
1.2 Background .....	3
1.3 Purpose and Scope of Work .....	4
CHAPTER 2 - REVIEW OF THEORIES .....	6
2.1 Components of Propeller Jet Velocity: Axial, Tangential, and Radial .....	6
2.2 Efflux Velocity ( $V_0$ ) .....	13
2.3 Interaction of the Propeller Jet with Free Surface .....	14
2.4 Fluid Velocity Field Measurement Techniques .....	15
CHAPTER 3 - DESCRIPTION OF EXPERIMENT .....	17
3.1 Basis and Scope of Test Plan .....	17

3.2	Determination of the Factors and the Design of Experiment.....	24
3.3	Experimental Set-up.....	26
3.3.1	Open Boat Propulsion System .....	28
3.3.2	EMCM System.....	29
3.3.3	Data Acquisition System.....	31
CHAPTER 4 - EXPERIMENTAL RESULTS .....		32
4.1	Overview.....	32
4.2	Scaling Effect Requirement and Measurement of Max. Mean Axial Velocity .....	34
4.3	Analysis of Results of the Experiment.....	37
4.3.1	Characteristics of the Mean Axial Velocity and the Variability of Flow (Standard Deviation) along $x/D_p$ .....	37
4.3.2	Influence of Factors on Propeller Wake Field Individually.....	39
4.3.3	Comparison of Experimental Results with the Bastin (2014) Mathematical Model (TB Model).....	46
4.3.4	Mean Axial Velocity along transverse locations (along $y/D_p$ ) .....	48
4.3.5	The Characteristics of Mean Axial Velocity at the Depth of Measurement ( $d$ $= 0.25D_p$ ) Closest to the Fluid Surface .....	53
4.3.6	Relationship among Factors, Location and Response Variables of Flow.....	58
4.3.7	Characteristics of the Mean Axial Velocity of Flow along $d/D_p$ and near the Fluid Surface .....	67
CHAPTER 5 - DISCUSSION OF RESULTS .....		70

CHAPTER 6 - CONCLUSION .....	77
REFERENCES .....	79
APPENDICES .....	85
Appendix 'A' .....	86
Appendix 'B' .....	90
Appendix 'C' .....	95
Appendix 'D' .....	99
Appendix 'E' .....	104

## List of Tables

Table 3.1: List for the locations of readings for ‘Near Field’ at a particular depth .....	21
Table 3.2: List for locations of readings for ‘Intermediate Field’ at a particular depth ....	21
Table 3.3: List for locations of readings for ‘Far Field’ at a particular depth .....	22
Table 3.4: List of factors and levels considered to design the experiment .....	26
Table 4.1: Results for thrust and torque coefficient.....	35
Table 4.2: Calculation of Reynolds numbers.....	35
Table 4.3: Comparison results for the measured maximum axial velocity for flow and corresponding calculated efflux velocity .....	36
Table 4.4: Combinations of experimental runs considered to apply OFAT in order to illustrate the individual effect of factors .....	40
Table 4.5: List of coefficients $K$ , $a$ , $b$ , $c$ and $a_1$ along the centre of the wake field .....	59
Table 4.6: List of coefficients $b_1$ , $c_1$ , $a_2$ , $b_2$ and $c_2$ along the centre of the wake field .....	61
Table 4.7: Validation of prediction equations at the centre of the wake field .....	64

## List of Figures

Figure 2.1: Schematic of velocity components of fluid particles in a wake field and Efflux Plane (Y-Z plane at $x = 0$ ).....	6
Figure 2.2: Schematic of showing propeller wake field zones and velocity distribution ....	7
Table 3.1: List for the locations of readings for ‘Near Field’ at a particular depth .....	21
Table 3.2: List for locations of readings for ‘Intermediate Field’ at a particular depth ....	21
Table 3.3: List for locations of readings for ‘Far Field’ at a particular depth .....	22
Figure 3.1: Dimension and measurement locations for ‘Near Field’ .....	22
Figure 3.2: Dimension and measurement locations for ‘Intermediate Field’ .....	23
Figure 3.3: Dimension and measurement locations for ‘Far Field’ .....	23
Table 3.4: List of factors and levels considered to design the experiment .....	26
Figure 3.4: Schematic diagram for the experimental set-up .....	27
Figure 3.5: Open boat propulsion system .....	28
Figure 3.6: EMC system, supporting frame, and tank platform .....	30
Figure 3.7: EMC sensors and built-in frame, except batteries and other accessories ....	30
Figure 3.8: Data acquisition system .....	31
Table 4.1: Results for thrust and torque coefficient .....	35
Table 4.2: Calculation of Reynolds numbers .....	35
Table 4.3: Comparison results for the measured maximum axial velocity for flow and corresponding calculated efflux velocity .....	36
Figure 4.1: Mean axial velocity, and mean axial velocity $\pm$ standard deviation as a function of $x/D_p$ at a depth $0.25D_p$ and transversely at $y/D_p = 0.0$ .....	38

Figure 4.2: Mean axial velocity, and mean axial velocity $\pm$ standard deviation as a function of $x/D_p$ at a depth $0.55D_p$ and transversely at $y/D_p = 0.0$ .....	38
Figure 4.3: Mean axial velocity, and mean axial velocity $\pm$ standard deviation as a function of $x/D_p$ at a depth $1.05D_p$ and transversely at $y/D_p = 0.0$ .....	39
Table 4.4: Combinations of experimental runs considered to apply OFAT in order to illustrate the individual effect of factors .....	40
Figure 4.4a: Mean axial velocity along $x/D_p$ at different rotational speeds for $H = 350$ mm and $\theta = 4.5^\circ$ at a depth of $0.25D_p$ from the water surface and at $y/D_p = 0.0$ .....	41
Figure 4.5a: Mean axial velocity at different rotational speeds along $x/D_p$ for $H = 350$ mm and $\theta = 4.5^\circ$ at a depth of $0.55D_p$ from water surface and at $y/D_p = 0.0$ .....	42
Figure 4.6a: Mean axial velocity at different rotational speeds along $x/D_p$ for $H = 350$ mm and $\theta = 4.5^\circ$ at a depth of $1.05D_p$ from water surface and at $y/D_p = 0.0$ .....	42
Figure 4.4b: Mean axial velocity at different propeller inclinations along $x/D_p$ for $H = 350$ mm and $n = 9$ rps at a depth of $0.25D_p$ from water surface and at $y/D_p = 0.0$ .....	43
Figure 4.5b: Mean axial velocity at different propeller inclinations along $x/D_p$ for $H = 350$ mm and $n = 9$ rps at a depth of $0.55D_p$ from the water surface and at $y/D_p = 0.0$ .....	43
Figure 4.6b: Mean axial velocity at different propeller inclinations along $x/D_p$ for $H = 350$ mm and $n = 9$ rps at a depth of $1.05D_p$ from the water surface and at $y/D_p = 0.0$ .....	44
Figure 4.4c: Mean axial velocity at different propeller submergences along $x/D_p$ for $\theta = 4.5^\circ$ and $n = 9$ rps at a depth of $0.25D_p$ from the water surface and at $y/D_p = 0.0$ .....	44
Figure 4.5c: Mean axial velocity at different propeller submergences along $x/D_p$ for $\theta = 4.5^\circ$ and $n = 9$ rps at a depth of $0.55D_p$ from the water surface and at $y/D_p = 0.0$ .....	45

Figure 4.6c: Mean axial velocity at different propeller submergences along $x/D_p$ for $\theta = 4.5^\circ$ and $n = 9$ rps at a depth of $1.05D_p$ from the water surface and at $y/D_p = 0.0$ .....	45
Figure 4.7a: Comparison plot for the mean axial velocity (m/s) along $x/D_p$ at a depth of $0.25D_p$ from the water surface and at $y/D_p = 0.0$ .....	46
Figure 4.7b: Comparison plot for the mean axial velocity (m/s) along $x/D_p$ at a depth of $0.55D_p$ from the water surface and at $y/D_p = 0.0$ .....	47
Figure 4.7c: Comparison plot for the mean axial velocity (m/s) along $x/D_p$ at a depth of $1.05D_p$ from the water surface and at $y/D_p = 0.0$ .....	47
Figure 4.8a: Mean axial velocity along $y/D_p$ at $x/D_p = 0.5$ .....	48
Figure 4.8b: Mean axial velocity along $y/D_p$ at $x/D_p = 1.5$ .....	49
Figure 4.8c: Mean axial velocity along $y/D_p$ at $x/D_p = 2.5$ .....	49
Figure 4.8d: Mean axial velocity along $y/D_p$ at $x/D_p = 3.5$ .....	50
Figure 4.8e: Mean axial velocity along $y/D_p$ at $x/D_p = 7.5$ .....	50
Figure 4.8f: Mean axial velocity along $y/D_p$ at $x/D_p = 11.5$ .....	51
Figure 4.8g: Mean axial velocity along $y/D_p$ at $x/D_p = 15.5$ .....	51
Figure 4.8h: Mean axial velocity along $y/D_p$ at $x/D_p = 20.5$ .....	52
Figure 4.8i: Mean axial velocity along $y/D_p$ at $x/D_p = 25.5$ .....	52
Figure 4.8j: Mean axial velocity along $y/D_p$ at $x/D_p = 30.5$ .....	53
Figure 4.9b: Mean axial velocity along $y/D_p$ at $x/D_p = 11.50, 15.50, 20.50, 25.50$ and $30.50$ ; for $n = 6$ rps, $\theta = 4.5^\circ$ and $H = 350$ mm.....	55
Figure 4.10a: Mean axial velocity with $y/D_p$ at $x/D_p = 0.50, 1.50, 2.50, 3.50$ and $7.50$ ; for $n = 9$ rps, $\theta = 4.5^\circ$ and $H = 350$ mm.....	55

Figure 4.10b: Mean axial velocity with $y/D_p$ at $x/D_p = 11.50, 15.50, 20.50, 25.50$ and $30.50$ ; for $n = 9$ rps, $\theta = 4.5^\circ$ and $H = 350$ mm.....	56
Figure 4.11a: Mean axial velocity with $y/D_p$ at $x/D_p = 0.50, 1.50, 2.50, 3.50$ and $7.50$ ; for $n = 12$ rps, $\theta = 4.5^\circ$ and $H = 350$ mm.....	56
Figure 4.11b: Mean axial velocity with $y/D_p$ at $x/D_p = 11.50, 15.50, 20.50, 25.50$ and $30.50$ ; for $n = 12$ rps, $\theta = 4.5^\circ$ and $H = 350$ mm.....	57
Table 4.5: List of coefficients $K, a, b, c$ and $a_1$ along the centre of the wake field .....	59
Table 4.6: List of coefficients $b_1, c_1, a_2, b_2$ and $c_2$ along the centre of the wake field.....	61
Table 4.7: Validation of prediction equations at the centre of the wake field .....	64
Figure 4.12: 3D surface plot at location #9 ( $x/D_p = 2.50, d/D_p = 1.05,$ and $y/D_p = 0.0$ ), showing the change of non-dimensional mean axial velocity with non-dimensional shaft rotational speed and propeller inclination.....	66
Figure 4.13: Mean axial velocity along $x/D_p$ at $y/D_p = 0.0$ for 3 depths, for propeller condition: $n = 9$ rps, $\theta = 4.5^\circ,$ and $H = 350$ mm .....	67
Figure 4.14: Mean axial velocity along $x/D_p$ at $y/D_p = 0.0$ for 3 depths, at propeller condition: $n = 6$ rps, $\theta = 4.5^\circ,$ and $H = 350$ mm .....	68
Figure 4.15: Mean axial velocity along $x/D_p$ at $y/D_p = 0.0$ for 3 depths, at propeller condition: $n = 9$ rps, $\theta = 9^\circ,$ and $H = 350$ mm .....	68
Figure 4.16: A Minitab plot showing the trend of the mean axial velocity against $x/D_p$ and $d/D_p$ at $y/D_p = 0.0,$ for propeller condition: $n = 9$ rps, $\theta = 4.5^\circ,$ and $H = 350$ mm .....	69
Figure A1: Mean axial velocity and mean velocity incorporating standard deviation along $x/D_p$ at a depth of $0.25D_p$ from water surface and at $y/D_p = 0.0$ for Case 1 .....	86

Figure A2: Mean axial velocity and mean velocity incorporating standard deviation along  $x/D_p$  at a depth of  $0.55D_p$  from the water surface and of  $y/D_p = 0.0$  for Case 1 .....87

Figure A3: Mean axial velocity and mean velocity incorporating standard deviation against  $x/D_p$  at a depth of  $1.05D_p$  from the water surface and at  $y/D_p = 0.0$  for Case 1 ....87

Figure A4: Mean axial velocity and mean velocity incorporating standard deviation against  $x/D_p$  at depth of  $0.25D_p$  from the water surface and at  $y/D_p = 0.0$  for Case 2.....88

Figure A5: Mean axial velocity and mean velocity incorporating standard deviation along  $x/D_p$  at depth of  $0.55D_p$  from the water surface and at  $y/D_p = 0.0$  for Case 2 .....88

Figure A6: Mean axial velocity and mean velocity incorporating standard deviation along  $x/D_p$  at a depth of  $1.05D_p$  from the water surface and at  $y/D_p = 0.0$  for Case 2 .....89

Figure B1: Mean axial velocity at different rotational speeds along  $x/D_p$  for  $H = 350$  mm and  $\theta = 4.5^\circ$  at a depth of  $0.25D_p$  from the water surface and at  $y/D_p = 1.0$ .....90

Figure B2: Mean axial velocity at different rotational speeds along  $x/D_p$  for  $H = 350$  mm and  $\theta = 4.5^\circ$  at a depth of  $0.55D_p$  from the water surface and at  $y/D_p = 1.0$ .....91

Figure B3: Mean axial velocity at different rotational speeds along  $x/D_p$  for  $H = 350$  mm and  $\theta = 4.5^\circ$  at a depth of  $1.05D_p$  from the water surface and at  $y/D_p = 1.0$ .....91

Figure B4: Mean axial velocity at different propeller inclinations along  $x/D_p$  for  $H = 350$  mm and  $\theta = 4.5^\circ$  at a depth of  $0.25D_p$  from the water surface and at  $y/D_p = 1.0$  .....92

Figure B5: Mean axial velocity at different propeller inclinations along  $x/D_p$  for  $H = 350$  mm and  $\theta = 4.5^\circ$  at a depth of  $0.55D_p$  from the water surface and at  $y/D_p = 1.0$  .....92

Figure B6: Mean axial velocity at different propeller inclinations along  $x/D_p$  for  $H = 350$  mm and  $\theta = 4.5^\circ$  at a depth of  $1.05D_p$  from the water surface and at  $y/D_p = 1.0$  .....93

Figure B7: Mean axial velocity at different propeller submergence along $x/D_p$ for $H = 350$ mm and $\theta = 4.5^\circ$ at a depth of $0.25D_p$ from the water surface and at $y/D_p = 1.0$ .....	93
Figure B8: Mean axial velocity at different propeller submergence along $x/D_p$ for $H = 350$ mm and $\theta = 4.5^\circ$ at a depth $0.55D_p$ from the water surface and at $y/D_p = 1.0$ .....	94
Figure B9: Mean axial velocity at different propeller submergence along $x/D_p$ for $H = 350$ mm and $\theta = 4.5^\circ$ at a depth of $1.05D_p$ from the water surface and at $y/D_p = 1.0$ .....	94
Figure C1: Mean axial velocity (m/s) along $x/D_p$ at a depth of $0.25D_p$ from the water surface and at $y/D_p = 0.0$ for Case 1 .....	95
Figure C2: Mean axial velocity (m/s) along $x/D_p$ at a depth of $0.55D_p$ from the water surface and at $y/D_p = 0.0$ for Case 1 .....	96
Figure C3: Mean axial velocity (m/s) along $x/D_p$ at a depth of $1.05D_p$ from the water surface and at $y/D_p = 0.0$ for Case 1 .....	96
Figure C4: Mean axial velocity (m/s) along $x/D_p$ at a depth of $0.25D_p$ from the water surface and at $y/D_p = 0.0$ for Case 2 .....	97
Figure C5: Mean axial velocity (m/s) along $x/D_p$ at a depth of $0.55D_p$ from water surface and at $y/D_p = 0.0$ for Case 2.....	97
Figure C6: Mean axial velocity (m/s) along $x/D_p$ at a depth of $1.05D_p$ from the water surface and at $y/D_p = 0.0$ for Case 2 .....	98
Figure D1: Mean axial velocity along $y/D_p$ at $x/D_p = 0.50, 1.50, 2.50, 3.50$ and $7.50$ ; for $n = 9$ rps, $\theta = 0^\circ$ and $H = 350$ mm.....	99
Figure D2: Mean axial velocity along $y/D_p$ at $x/D_p = 11.50, 15.50, 20.50, 25.50$ and $30.50$ ; for $n = 9$ rps, $\theta = 0^\circ$ and $H = 350$ mm.....	100

Figure D3: Mean axial velocity along $y/D_p$ at $x/D_p = 0.50, 1.50, 2.50, 3.50$ and $7.50$ ; for $n = 9$ rps, $\theta = 9^\circ$ and $H = 350$ mm.....	100
Figure D4: Mean axial velocity along $y/D_p$ at $x/D_p = 11.50, 15.50, 20.50, 25.50$ and $30.50$ ; for $n = 9$ rps, $\theta = 9^\circ$ and $H = 350$ mm.....	101
Figure D5: Mean axial velocity along $y/D_p$ at $x/D_p = 0.50, 1.50, 2.50, 3.50$ and $7.50$ ; for $n = 9$ rps, $\theta = 4.5^\circ$ and $H = 200$ mm.....	102
Figure D6: Mean axial velocity with $y/D_p$ at $x/D_p = 11.50, 15.50, 20.50, 25.50$ and $30.50$ ; for $n = 9$ rps, $\theta = 4.5^\circ$ and $H = 200$ mm.....	102
Figure D7: Mean axial velocity along $y/D_p$ at $x/D_p = 0.50, 1.50, 2.50, 3.50$ and $7.50$ ; for $n = 9$ rps, $\theta = 4.5^\circ$ , and $H = 500$ mm.....	103
Figure D8: Mean axial velocity with $y/D_p$ at $x/D_p = 11.50, 15.50, 20.50, 25.50$ and $30.50$ ; for $n = 9$ rps, $\theta = 4.5^\circ$ , and $H = 500$ mm.....	103

## NOMENCLATURE AND ABBREVIATIONS

### Nomenclatures

$B_T$	Breadth of OERC tow tank
$c$	Chord length of a propeller blade
$C_t$	Thrust coefficient of the propeller
$d$	Vertical distance (along propeller depth) from the water surface at which the readings were taken (3#) during experiment
$D_T$	Depth of OERC tow tank
$D_p$	Propeller diameter (m)
$D_h$	Propeller hub diameter (m)
$h_d$	Helical distance from blade section leading edge to rake datum
$h_t$	Helical distance from blade section leading edge to position of maximum thickness
$H$	The depth of submergence of propeller (mm)
$L_T$	Length of OERC tow tank
$n$	Propeller Rotational Speed (rps)
$P$	Pitch of blade
$y$	Transverse distance from the center of the wake field, at which the readings were taken during experiment
rps	Rotation per second
$R_{MaxAxial}$	Position of Maximum Axial Velocity
$R_{MaxTang}$	Radial position of Maximum Tangential Velocity

$Re_{\text{flow}}$	Flow Reynolds Number
$Re_{\text{prop}}$	Propeller Reynolds Number
$R_p$	Propeller Radius
$t$	Thickness of blade
$V_o$	Efflux Velocity
$V_{\text{Axial}}$	Axial Velocity in the Wake
$V_{\text{MaxAxial}}$	Maximum Axial Velocity
$V_{\text{Tang}}$	Tangential Velocity in the Wake
$V_{\text{MaxTang}}$	Maximum Tangential Velocity
$V_{x,r}$	Velocity at 'x' longitudinal distance from the propeller face, and 'r' radial distance from the propeller rotation axis
$x$	Distance along the direction at which wake is propagating
$Z$	Number of Propeller Blades
$\beta$	Propeller Blade Area Ration
$\sigma$	Standard deviation (variability of flow)
$\zeta$	Efflux coefficient
$\mu$	Kinematic Viscosity of Fluid ( $\text{Kg.m}^{-1}\text{s}^{-1}$ )
$\nu$	Viscosity of Fluid ( $\text{Kg.m}^2\text{s}^{-1}$ )

## **Abbreviations**

FPSO	Floating Production Storage Offloading vessel
LDA / LDV	Laser Doppler Anemometry (Velocimetry)
OERC	Ocean Engineering Research Centre (Memorial University)
PIV	Particle Image Velocimetry
TB model	Tony Bastin's (mathematical) model
ZEF	Zone of Established Flow
ZFE	Zone of Flow Establishment

## **CHAPTER 1 - INTRODUCTION**

### **1.1 Literature Review**

Investigations have shown that the operational limit and the duration of operations in arctic and sub-arctic oceans can be increased considerably through proper sea ice management. Ice management can be used to reduce ice-induced mooring loads on an FPSO, and ice management is a proven technique to defend stationary ships and structures in moving pack ice (Martin et al., 2008). Also, it has been demonstrated practically that using ice breakers to break and clear pack ice enables a drillship or similar floating platform to operate beyond that structure's independent operational limit (Martin et al., 2008; Hamilton et al., 2011). Without any ice management, some offshore oil and gas activities are impossible, such as those on Grand Banks (Timco et al., 2007), where iceberg management is required. Ice management requirements and techniques mostly depend on the meteorological condition of the region, available resources, and the ice-strengthening of the vessel.

Usually ice breakers are used to break and manage ice in shipping channels and operational fields, where conventional ice breaking operations largely depend on the strength, power, and maneuvering capability of vessel. Propeller wake wash can be used as an effective means of clearing pack ice, and even breaking level ice. Numerous investigations have been done on propeller wake effect by researchers in the past (Albertson et al., 1950; Wagnanski et al., 1969; Blaauw and Van de Ka., 1978; Verhey et al., 1983; Fuehrer et al., 1977; Madnia and Bernal, 1994; Hamill et al., 1987). Most of the past work has involved sea bed scour, rather than the propeller wake field. In 1986 (Anderson et al., 1986) research on various pack ice management

techniques on the Newfoundland-Labrador shelf was performed, and propeller wake wash (named as 'Prop-Wash') was found to be the only mechanism having a noticeable degree of success. The technique was successfully used in clearing small ice floes within close proximity to a vessel, where the vessel was dynamically positioned. In more recent studies of various ice management techniques applied in different arctic regions in full-scale operations, it was found that the wake of an azimuth thruster can be more useful than the hull of an ice breaker in breaking ice (Keinonen and Lohi, 2000; Keinonen et al., 2008), in addition to clearing ice from designated areas. Also, propeller wake wash was found to be an effective means of dismantling severe ice ridges, pushing away medium sized ice floes, or even glacial ice. The biggest advantage of this technique is that it enables ice management, without having any physical interaction with ice.

One of the most recent studies on propeller wake wash was a laboratory experiment done by Ferrieri (Ferrieri et al., 2013). In that experiment, change in ice concentration was investigated as a function of different factors affecting propeller wake wash: propeller shaft rotational speed, inclination angle of propeller, initial ice concentration, and distance to the ice edge from propeller. Propeller shaft speed was found to be the most influential factor affecting propeller wake to clear ice. Bastin (2014) did follow-up research on propeller wake wash, and developed a semi-empirical mathematical model of propeller wake wash for pack ice management.

A detailed study on the propeller wake field can be done by performing measurements on the fluid velocity field. Various experimental techniques can be applied, which require the application of advanced equipment to determine the velocity in a flow, such as Laser-Doppler Velocimetry (LDV), PIV (Particle Image Velocimetry), Hot

Wire Anemometry, and Current Meters (Acoustic Doppler or Electromagnetic). Investigations on fluid velocity field measurement (Lam et al., 2010; 2012a; 2013) of a propeller jet showed that, LDV (LDA) can successfully be used to determine the fluid velocity in a propeller wake field.

## **1.2 Background**

Several researchers have studied ice management using propeller wake wash. Research has been done by performing experiments and developing a semi-empirical mathematical model covering the field near the propeller, as well as far downstream of the propeller. The laboratory experiment conducted by Ferrieri (2012) was designed by considering four factors, as described earlier. The response variable of the experiment was ‘change in ice concentration’ in terms of the variation of the factors. The results of the experiment provided practical information about the change of ice concentration throughout a propeller wake field in terms of the factors. Based on the experimental results, Ferrieri (2012) and Ferrieri et al. (2013) developed some regression equations illustrating the relationships among the factors influencing propeller wake wash downstream of a propeller wake field, and the change in ice concentration. Bastin (2014) did follow-up research on propeller wake wash, and developed a mathematical model of propeller wake wash for pack ice management. The output of the mathematical model developed by Bastin (2014) was compared to the experimental results obtained from the laboratory experiment done by Ferrieri (2012).

Bastin reported that the semi-empirical model can be upgraded by incorporating the effect of turbulence, particularly for the vicinity area of propeller. The works reported

by Ferrieri (2012) and Bastin (2014) were based on the interaction of propeller wake with ice floes, but neither provided any data regarding the distribution of fluid velocity and variability throughout the wake field, nor their relationship with the factors. If the distribution of fluid velocity throughout the wake field, and the effect of factors on the fluid velocity are known, then propeller wake wash can be applied more effectively for clearing pack ice.

### **1.3 Purpose and Scope of Work**

The purpose of the present research is to investigate the characteristics of a velocity field generated in a propeller wake in terms of the factors influencing propeller wake wash, and to develop prediction models for the propeller wake velocity field. In the experiment, the components of fluid velocity were measured at a number of locations covering the entire effective wake field. Measurements were also done vertically at three different depths in the 3D wake field. The effective wake field was also divided into three different zones along the downstream of propeller wake field, and measurements were done at different locations in these three zones longitudinally, transversely, and vertically. The total number of measurement locations within the 3D propeller wake field was 168. The experimental results are presented with a number of graphs, tables, and equations.

The results of the experiment are also compared with the results obtained from the mathematical model of Bastin (2014) for several conditions. Bastin's model was developed on the basis of empirical and semi-empirical equations. Some suggestions are made to improve the model on the basis of the comparison plots showing the difference between the experimental results and model (Bastin, 2014) results.

All the experimental data and analyzed results of this study are presented in a test report (Amin et al., 2017). In this thesis, the background of the research, the design and set-up of the experiment, the various aspects of data analysis, and some results with validation are presented. The characteristics of the propeller wake velocity field near the fluid surface with the variation of the factors were of particular interest for the experimental study. Results were analyzed only for the mean axial flow downstream of the propeller wake field.

## CHAPTER 2 - REVIEW OF THEORIES

### 2.1 Components of Propeller Jet Velocity: Axial, Tangential, and Radial

Propeller wake velocity is a complex flow having major components of velocity along axial, tangential, and radial directions. The axial component of velocity is the major contributor to the total fluid velocity in a wake field. Researchers have been historically particularly interested in the axial component of velocity. The three velocity components of fluid particles along three directions downstream of a 3D wake field are shown in Figure 2.1, as below:

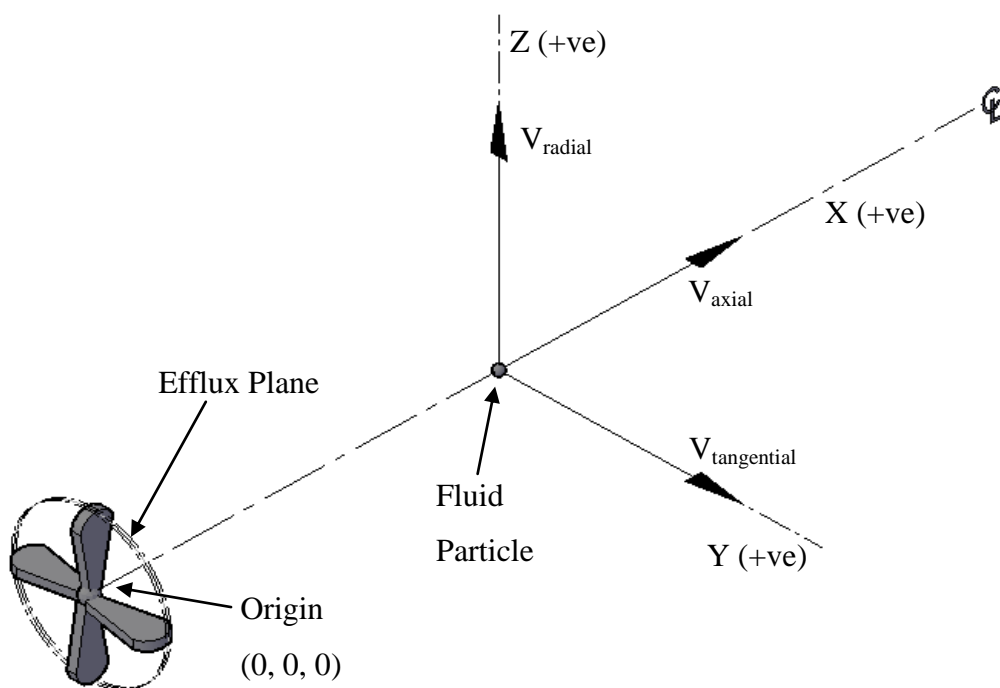


Figure 2.1: Schematic of velocity components of fluid particles in a wake field and Efflux Plane (Y-Z plane at  $x = 0$ )

Albertson (1950) used a plain water jet to investigate the velocity field within the jet based on axial momentum theory, and that was the basis of most of the subsequent works on propeller jet velocity. Albertson (1950) divided the wake field into two zones on the basis of the pattern of the distribution of fluid axial velocity: ZFE (Zone of Flow Establishment) and ZEF (Zone of Established Flow). Later Blaauw and van de Kaa (1978), Verhey (1983), Hamill (1987), and Lam et al. (2010, 2011, 2012 and 2012a) investigated the velocity field within a propeller jet, and proposed similar zones as Albertson (1950). Figure 2.2 shows the different wake field zones (ZFE and ZEF), and the patterns of fluid velocity distribution in those zones.

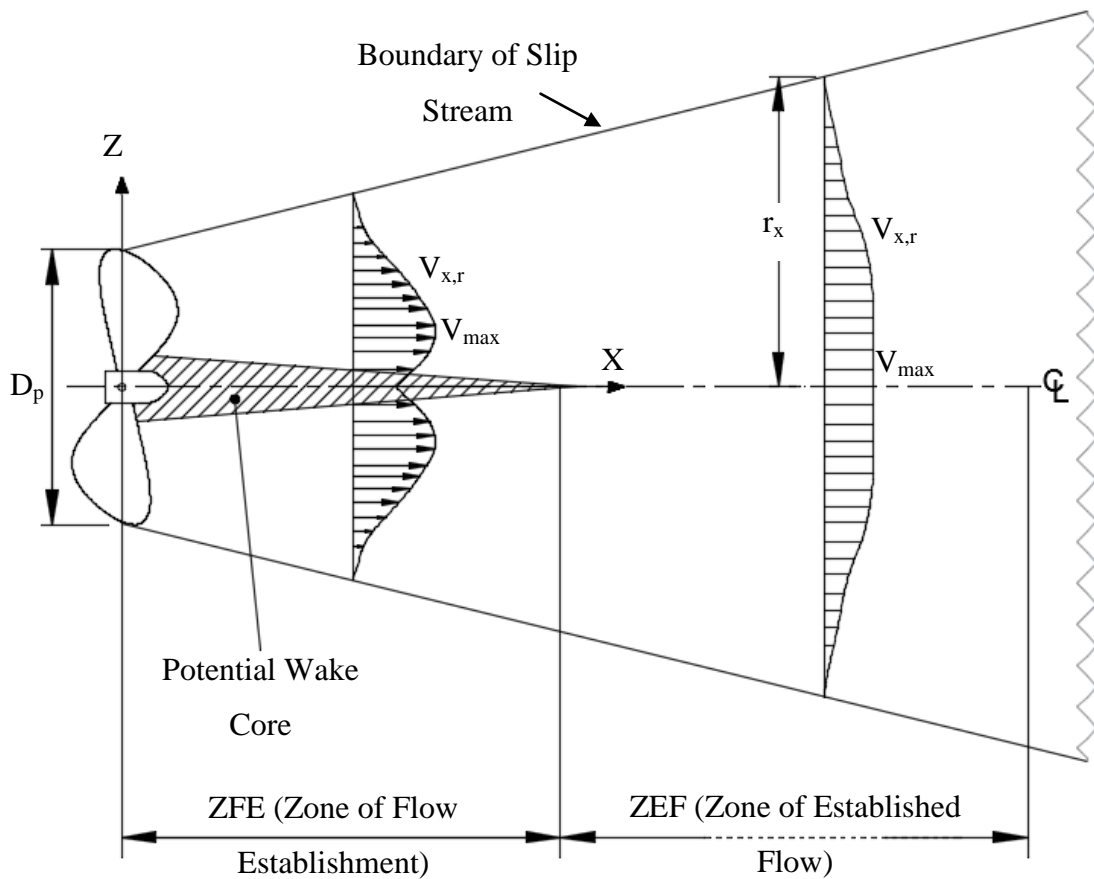


Figure 2.2: Schematic of showing propeller wake field zones and velocity distribution (Hamill, 1987)

ZFE can be defined as the zone within the jet, where the jet is under development, and ZEF is the zone where the jet is fully developed. Lam et al. (2011) reported that, maximum axial velocity decays in ZFE and ZEF at different rates, through experimental investigation. The experiment showed an in-depth study of maximum velocity and maximum turbulent fluctuation in axial, tangential and radial components, and the decay of the maximum turbulent energy at these zones. At the initial stage of ship's propeller jet (ZFE), the maximum axial velocity was considered as constant by some researchers (Albertson, 1950; Blaauw and Van de Kaa, 1978; Verhey, 1983), and some researchers (Hamill and Johnson, 1993; Hamill et al., 2013; Stewart, 1992; Hashmi, 1993) disagree with that opinion.

Propeller wake has a rotational feature, which makes it different from a plain water jet. Within the ZFE the pattern of velocity distribution in a wake is axisymmetric about the axis of rotation. The length of ZFE along the wake field, and the distribution of the axial velocity in ZFE were investigated by a number of researchers (Albertson, 1950; Fuehrer and Romisch, 1977; Blaauw and Van de Kaa, 1978; Hamill, 1987; Stewart, 1992; Hashmi, 1993; Lam et al., 2011 and 2012) with increasingly improved experiments. In one of the latest investigations done by Lam et al. (2012a), it was reported that the extent of ZFE can be approximately up to  $x/D_P = 2.63$  downstream of a propeller wake, where 'x' denotes longitudinal distance along the propagation of jet, and 'D<sub>P</sub>' denotes propeller diameter.

### Axial Velocity

Axial velocity is the velocity along the direction at that the wake propagates. Figure 2.2 shows the profile for the distribution of axial velocity in ZFE and ZEF. Within the ZFE, axial velocity distribution at the efflux plane (at  $x/D_P = 0$ ) shows two peaked ridges (Figure 2.2) having low velocity core at the axis of rotation. The low velocity core is due to the hub of the propeller (Lam et al., 2010), and as the wake propagates, the peaks merge into one. After merging, the highest velocity is now at the rotation axis of the wake, which is the maximum axial velocity at the plane. If the plane is efflux plane, then it is known as efflux velocity. Maximum axial velocity in a wake field is the same as efflux velocity. Due to the effect of maximum axial velocity, researchers have concentrated on developing empirical equations of maximum axial velocity ( $V_{MaxAxial}$ ) in terms of efflux velocity ( $V_0$ ) and other variables. The major empirical equations obtained from the previous research are as follows:

$$\frac{V_{MaxAxial}}{V_0} = 1 \quad \text{[for } 0 \leq \frac{x}{D_P} < 0.35, \text{ by Hamill (1987)]}$$

$$\frac{V_{MaxAxial}}{V_0} = 0.87 \left( \frac{x}{D_P} \right)^{-\frac{\beta}{4}} \quad \text{[for } 0.35 \leq \frac{x}{D_P} < 2, \text{ by Hamill (1987)]}$$

$$\frac{V_{MaxAxial}}{V_0} = A' \left( \frac{x}{D_P} \right)^{B'} \quad \text{[for } \frac{x}{D_P} \geq 2, \text{ by Hamill (1987)]}$$

$$\frac{V_{MaxAxial}}{V_0} = 1.0172 - 0.1835 \left( \frac{x}{D_P} \right) \quad \text{[for } 0 \leq \frac{x}{D_P} < 3.25, \text{ by Stewart (1992)]}$$

$$\frac{V_{MaxAxial}}{V_0} = 0.638 e^{-\frac{0.097x}{D_P}} \quad \text{[for } 3.25 \leq \frac{x}{D_P} < 16, \text{ by Hashmi (1993)]}$$

$$\frac{V_{MaxAxial}}{V_0} = 1 - 0.1592 \left( \frac{x}{D_P} \right) \quad \text{[for } 0 \leq \frac{x}{D_P} < 3.68, \text{ by Lam et al. (2011)]}$$

The latest investigation (Lam et al., 2011) validated Stewart's (1992) suggestion regarding the rejection of the constant velocity idea throughout the ZFE. Hamill (1987) found that the idea of constant velocity was correct up to the  $x/D_p = 0.35$  downstream, where maximum axial velocity was equal to the efflux velocity. After this distance the maximum velocity decays steadily along the jet. For velocity predicting for the extent of ZEF, Albertson (1950) proposed a semi-empirical equation, which was accepted by other researchers (Hamill, 1987; Stewart, 1992; McGarvey, 1996; Lam et al., 2011):  $\frac{V_{x,r}}{V_{Max}} = e^{[-22.2(\frac{r}{x})^2]}$ .

### **Tangential Velocity**

The tangential component of velocity is typically the second largest contributor to the total velocity field of a propeller wake, estimated to be about 82% and 78% of maximum axial velocity by Lam et al., 2011 and Lam et al., 2013, respectively. The magnitude of tangential velocity downstream  $x/D_p = 3.68$  diminishes rapidly (Lam et al., 2011). Brewster (1997) reported that the decay of maximum tangential velocity is exponential along the longitudinal axis from the initial efflux plane and suggested the below equations:

$$\frac{V_{MaxTang}}{nD_p} = 0.38e^{-0.3(\frac{x}{D_p})} \quad \left[ \text{for } 0 \leq \frac{x}{D_p} < 0.79, \text{ by Brewster (1997)} \right]$$

$$\frac{V_{MaxTang}}{nD_p} = 0.47e^{-0.35(\frac{x}{D_p})} \quad \left[ \text{for } 0.79 \leq \frac{x}{D_p} < 6.32, \text{ by Brewster (1997)} \right]$$

Further investigation had been carried out in the latest study by Lam (2011), where he proposed a linear equation representing the tangential decay of wake flow until  $x/D_p = 0.79$  downstream, and exponential equation representing the decay afterwards. The proposed models were as follows:

$$\frac{V_{\text{MaxTang}}}{V_0} = -0.6492 \left( \frac{x}{D_p} \right) + 0.9749 \quad \left[ \text{for } 0 \leq \frac{x}{D_p} < 0.79, \text{ by Lam et al. (2011)} \right]$$

$$\frac{V_{\text{MaxTang}}}{V_0} = 0.7031 e^{-0.4998 \left( \frac{x}{D_p} \right)} \quad \left[ \text{for } 0.79 \leq \frac{x}{D_p} < 6.32, \text{ by Lam et al. (2011)} \right]$$

Lam et al. (2011) reported that the radial distance of the maximum tangential velocity increased along  $x/D_p$ . The position of the maximum tangential velocity at the efflux plane was at a radial distance  $r/R_p = 0.13$ . In the report, it was also shown that the tangential velocity within a propeller wake did not have a consistent trend, rather the maximum velocity fluctuated randomly.

### **Radial Velocity**

The radial velocity component is the reason for the expansion of the propeller jet radially. Lam et al. (2010) performed an experiment on the axisymmetric characteristics of a ship's propeller jet. Lam determined the magnitudes of axial, tangential, and radial turbulence intensities (dimensionless turbulence stress) at the rotation axis through the experiment, which were 0.28, 0.88 and 5.86 respectively. Thus the turbulence intensity of the radial component of total velocity is higher than the other components. McGarvey (1996) reported that the magnitude of radial component of velocity was around 30% of the axial velocity along the face of the propeller. Lam et al. (2010) also reported that the average radial velocity closer to propeller face (within ZFE) was 14% of the axial velocity. McGarvey, 1996;

Brewster, 1997; and Lam et al., 2011 and 2013 agreed that the radial component of velocity was insignificant at a small distance away from the propeller face (efflux plane). McGarvey and Brewster found this distance as approximately between  $\frac{x}{D_p} = 0.3$  and  $\frac{x}{D_p} = 1.5$  downstream. As the maximum amount of the radial component of velocity decays within the vicinity area of propeller, the flow consequently becomes very turbulent closer to propeller.

McGarvey (1996) measured the radial component of velocity using LDA and established a relationship based on propeller blade characteristics to determine the distribution of radial velocity:

$$\frac{V_{r(x,r)}}{nZR} = 0.768 \left(\frac{P}{R}\right)^{-1.241} \left(\frac{C}{R}\right)^{6.177} \left(\frac{t}{R}\right)^{-1.002} \left(\frac{h_d}{R}\right)^{-1.286} \left(\frac{h_t}{c}\right)^{5.291}$$

McGarvey found this equation underestimated the radial distance along the propeller blade to the peak velocity, and overestimated the magnitude of overall velocity distribution. He suggested further investigation in improving the equation.

Besides factors affecting propeller wake velocity field, propeller geometry also has significant influence to the axial, tangential, and radial components of velocity (Lam et al., 2010). The maximum tangential and the maximum radial components of fluid velocity are approximately 78% and 3% of the maximum axial velocity (Lam et al., 2013), where the tangential velocity diminishes within the close proximity of efflux plane and the radial velocity diminishes at the vicinity of propeller face. Therefore the axial velocity of fluid is the major contributor to the velocity field downstream of a propeller, and the tangential velocity is significant for the investigations in ZFE.

## 2.2 Efflux Velocity ( $V_0$ )

The term “efflux” was used by Albertson (1950), but the equations for efflux velocity were developed later based on the axial momentum theory, which was accepted by most subsequent researchers to predict efflux velocity. Efflux velocity is defined as the maximum velocity at the face of the propeller. The maximum velocity obtained from a time-averaged velocity distribution along the initial propeller plane, which is known as efflux plane. Hence, efflux plane is the initial plane immediately downstream of the propeller jet, and efflux velocity is measured at efflux plane. Efflux velocity is the velocity predicted by the early pioneering investigations for the fluid field near to propeller based on axial momentum theory. Later, when it was found that the behavior of an actual ship propeller jet contradicted most of the assumptions made within axial momentum theory, the efflux velocity was replaced in the equations to predict maximum velocities. Researchers still use the efflux velocity as a multiplier in calculating maximum axial velocity (see equation of maximum axial velocity). Near the propeller face, maximum axial velocity is the same as efflux velocity, but far downstream of the propeller the prediction equations for maximum velocity are different. Fuehrer and Romisch (1977) first developed the equation to predict efflux velocity based on axial momentum theory, which was refined by Hamill (1987), Stewart (1992), and Hashmi (1993) through experimental investigations. The evolution of equations predicting efflux velocity is shown below:

$$V_0 = 1.59nD_P\sqrt{C_t} \quad [\text{By Fuehrer et al. (1977)}]$$

$$V_0 = 1.33nD_P\sqrt{C_t} \quad [\text{By Hamill (1987)}]$$

$$V_0 = \zeta nD_P\sqrt{C_t} \quad [\text{By Stewart (1992)}]$$

$$\text{Where, } \zeta = D_P^{-0.0686} P^{1.519} \beta^{-0.323}$$

$$V_0 = E_0 n D_P \sqrt{C_t} \quad [\text{By Hashmi (1993)}]$$

$$\text{Where, } E_0 = \left(\frac{D_P}{D_h}\right) C_t^{-0.403} \beta^{0.744}$$

The latest research by Lam et al., 2013 is in agreement with the prediction equation obtained through axial momentum theory having only 2% difference.

### **2.3 Interaction of the Propeller Jet with Free Surface**

Propeller wake is a complicated flow having two major components: one directing towards the fluid surface and another towards the sea bed. In the case of ice management, typically the component interacting with fluid surface is more important. The component interacting with fluid surface causes turbulence at the interaction region, which was studied by numerous researchers including Anthony (1990), Anthony and Willmarth (1992), Madina and Bernal (1994), Walker, Chen and Willmarth (1995), and Bernal and Scherer (1997). One of the latest studies by Tian (2011) reported that when the jet interacts with the free surface, a surface current is produced which occupied a thin layer beneath the surface. When the surface wave and surface currents move in the same direction, the wave amplitude decreases and wave length increases. Madina and Bernal (1994) reported that surface waves are propagated as large scale vortical structures in the jet flow as they interact with water surface. They also reported that the waves propagate at an angle with respect to the direction of flow, which increases against the increase of Flow Froude number. The investigation made a comparison of jet interacting with the fluid surface against free jet, and it was found that the decay rate of the maximum mean velocity at the far field is reduced by a factor  $\sqrt{2}$  comparing to free jet. The average growth rate of turbulent jet within the region of  $\frac{x}{D_P} \leq 24$  downstream was almost the same as free jet.

Bernal and Scherer (1997) performed a similar experiment considering Froude number, and reported that at high Froude number the surface disturbances increase and radiate energy away from the flow in the form of waves. Again as the Reynolds number was increased, the growth and decay of jet were decreased along the downstream. Based on the significant influence of Froude number on the turbulent behavior of jet interacting with free surface, Walker (1995) found that for the high Froude number case, turbulent energy can be reduced by up to 20%.

Tian (2011) characterized the jet as a large scale coherent structure. He reported that as the downstream distance increases, which means  $\frac{x}{D_p}$  increases, the spreading of turbulent jet near the region of the fluid surface is more than that for a free jet, and turbulent intensity is reduced by the effect of free surface confinement.

## **2.4 Fluid Velocity Field Measurement Techniques**

To assess the strength of a wake, fluid velocity measurement is important. Different techniques have been developed to measure the fluid velocity field. The first anemometer to measure wind velocity was developed in 1845, followed by major improvements in 1926, 1935 and 1991. Meanwhile after the innovation and some improvements of air anemometer, Hot Wire Anemometer (HWA) was developed to measure fluid particle velocity. This technique is based on the heat transfer from a sensing element and for this reason is very sensitive to ambient temperature changes. The use of HWA is therefore not usually recommended for the measurement of mean flow properties. Laufer (1953) and his contemporary researchers used hot wire anemometer to do some velocity, momentum, and energy measurements in a plain or in a propeller jet. But no validations of the results were done during that time.

Innovation of LDA (Laser Doppler Anemometry) added a new dimension in measuring fluid flow velocity accurately without affecting the flow. Lam et al. (2013) performed an experiment measuring the time-averaged velocity, and the turbulent intensity at the initial plane from a ship's propeller using both CFD analysis and LDA measurements. The predicted velocities were found quite in agreement to each-other. Lam also did numerous experiments using LDA measurement verifying the measured data against results obtained using empirical equations derived by earlier researchers. PIV (Particle Image Velocimetry) and UDV (Ultrasonic Doppler Velocimeter) have also been used to measure the fluid particle velocity, which are quite similar in mechanism to LDA. Although application of PIV is not very common in fluid field velocity measurement comparing to LDA, different researchers used this technique in measuring velocity. Hout et al. (2001) measured the velocity field around the Taylor bubble using PIV technique. Similarly UDV is another technique to measure velocity field (Alfonsi et al., 2003), which is the latest version of fluid velocity field measurement technique.

## CHAPTER 3 - DESCRIPTION OF EXPERIMENT

### 3.1 Basis and Scope of Test Plan

The experiment was performed in the tow tank of OERC (Ocean Engineering Research Centre) of Memorial University. The dimensions of the tank are  $L_T \times B_T \times D_T = 58.27 \times 4.57 \times 3.04$  meter. The propeller wake was generated using an existing B-series propeller (B4-55) of diameter 250 mm in order to investigate the wake wash in stationary, or bollard, condition. Measurements of the fluid velocity were taken using a pair of EMCM (Electro-magnetic Current Meter). The EMCM package was capable of measuring three (x, y, z) components of velocity in a fluid field.

In order to control the factors of the experiment (power delivered by the propeller, inclination of propeller, and submergence of propeller), an open boat propulsion system was used. This system includes a propeller, propeller drive, a frame for adjusting the propeller depth and inclination angle, dynamometers for measuring propeller thrust, torque, and global loads, as well as means to measure shaft speed.

The measurements of fluid velocity were done at 3 different depths in the 3D wake field. The first measurement depth (the depth of measurement that was closest to the fluid surface) was intended to capture the free surface velocity field, which is of particular practical interest in terms of ice management. As the EMCM sensors (5.5 cm disks) had to be entirely submerged under the water in order to get the readings, it was not possible practically to capture the readings exactly at the free surface. The sensors were put at a depth of  $0.25D_p$  below the water surface, which provided readings as close to the fluid (water) surface as possible. The second measurement depth was taken at  $0.55D_p$  (137.5 mm) depth from the water surface. The third

measurement was at  $1.05D_p$  (262.5 mm) from the water surface. Readings were also taken longitudinally and transversely covering half-width of the wake field. The decision to survey only the half width required an assumption of axial symmetry in the wake. Although this is not true in the field near the propeller, it is a reasonable assumption for the far downstream. Furthermore this allowed a more detailed survey of the flow within the limitations of time and resources.

In order to take readings longitudinally, the length of the effective wake field was considered up to  $x/D_p = 30.5$  downstream of the propeller. Here 'x' is the longitudinal distance along the propagation of the wake from propeller plane, and 'D<sub>p</sub>' is the propeller diameter. For convenience, this large area (up to  $x/D_p = 30.5$  along the propeller wake field) was divided into 3 zones. Readings were taken at a series of points in those zones, as defined in Tables 3.1 to 3.3.

The 3 zones considered longitudinally (along the length of tow tank) are as follows:

- (i) Near Field (4#): from  $x/D_p = 0.5$  to  $x/D_p = 3.5$  (at 250 mm interval)
- (ii) Intermediate Field (4#): from  $x/D_p = 3.5$  to  $x/D_p = 15.5$  (at 1000 mm interval)
- (iii) Far Field (4#): from  $x/D_p = 15.5$  to  $x/D_p = 30.5$  (at 1250 mm interval)

The 3 zones were also split transversely (along the breadth of tow tank) as follows:

- (i) Near Field (4#): from  $y/D_p = 0.0$  to  $y/D_p = 1.5$  (at 125 mm interval)
- (ii) Intermediate Field (5#): from  $y/D_p = 0.0$  to  $y/D_p = 3.0$  (at 187.5 mm interval)
- (iii) Far Field (5#): from  $y/D_p = 0.0$  to  $y/D_p = 4.0$  (at 250 mm interval)

The transverse location for the measurement is expressed in terms of  $y/D_p$ , where 'y' is the transverse distance along the propeller plane from the centre of the wake field.

The total number of locations at which the readings were taken under an experimental run within the entire effective wake field was  $[(4 \times 4) + (4 \times 5) + (4 \times 5)] \times 3 = 168$ . There were nine of the locations coincide, so the total number of locations becomes  $(168 - 9) = 159$ .

The experiment was a follow-up study of earlier research on propeller wake wash (Ferrieri, 2012 and Bastin, 2014), and the experimental runs were determined using the Design Expert 9.0 (DE 9.0) software. The division of zones was done on the basis of the rate of change of fluid velocity in the wake field. Based on earlier investigation, it was expected that the rate of change of fluid velocity, particularly tangential and radial components, would be high at the near field, and then gradually decrease at the intermediate and far field zones downstream of the propeller wake. The pattern of propeller wake can be considered as axisymmetric at the initial stage of the decay, due to the presence of turbulence (Wygnański and Fiedler, 1969), and then it becomes symmetric (Blaauw and van de Kaa, 1978; Verhey, 1983; Stewart, 1992; Hashmi, 1993; McGarvey, 1996; Brewster, 1997; Lam et al., 2011 and 2012). The length of the effective wake field was considered as  $x/D_p = 30.50$ , which was based on the experiment performed by Ferrieri (2012). Ferrieri (2012) did an experiment considering an area from  $x/D_p = 0.50$  to  $x/D_p = 19.50$ . It was found in the experiment that the wake at the far field downstream of propeller wake was too weak to clear the ice floes. Therefore, the length of wake field (up to  $x/D_p = 30.50$ ) considered in the experiment, was expected to be adequate for the present study, as the size of the effective wake field should not be larger than  $x/D_p = 30.50$ . The near field was considered up to  $x/D_p = 3.50$  downstream the wake field, where the decay of axial, tangential, and radial components of velocities was expected to be high. The

consideration was based on the experiment performed by Stewart (1992), which was validated with slight amendment by Lam et al. (2011). The intermediate field was considered from  $x/D_p = 3.5$  to  $x/D_p = 15.5$ . This zone was expected to be the most influential field particularly from the context of ice management using propeller wake wash. Hashmi (1993) reported that the ZEF (Zone of Established Flow) could be considered as  $3.25 \leq x/D_p \leq 16$ , and proposed an exponential equation replacing the linear equation proposed by Stewart (1992), which was validated by Lam et al. (2012). In the experiment, the measurement was taken up to  $x/D_p = 30.50$ , dividing in to 3 zones: near field ( $0 \leq x/D_p \leq 3.5$ ), intermediate field ( $3.5 \leq x/D_p \leq 15.5$ ), and far field ( $15.5 \leq x/D_p \leq 30.5$ ). It was expected that the extent of the wake field ( $x/D_p \leq 30.5$ ) considered for the study should cover all the effective wake fields for all the combinations of factors.

In order to determine the extent of measurement transversely, different measuring widths were considered for 3 zones, which increased along  $x/D_p$  from the propeller plane. For near field, fluid velocity was measured transversely up to  $y/D_p = 1.50$ . It was assumed that at  $x/D_p = 3.50$  downstream the wake field, the approximate transverse width of wake field would be:  $b_{3.50} = \{D_p/2 + 0.32*(x/D_p)\} = 385$  mm. The semi-empirical formula used for the calculation was reported in Bastin (2014). For near field, the maximum width from the propeller rotation axis was  $= (385/2) = 192.5$  mm ( $0.77 \frac{y}{D_p}$ ), and the measurement during the experiment was taken up to 375 mm ( $1.5 \frac{y}{D_p}$ ) from the axis of propeller rotation. Figure 3.1 illustrates the pattern of the predicted effective wake field, and the locations where measurements were taken at the near field zone.

Similarly, the extent of measurements transversely were determined for intermediate and far field zones, on the basis of the semi-empirical formula by Bastin (2014). Maximum width of the wake plume intersecting with the water surface for the intermediate field zone was calculated as 1345 mm, and thus with respect to the propeller rotation axis the width was 672.5 mm ( $2.69\frac{y}{D_p}$ ). During the experiment, the width of measurement throughout the intermediate field zone was 750 mm ( $3\frac{y}{D_p}$ ). Similarly, the width of measurement for far field zone was determined. Figure 3.2 and Figure 3.3 illustrate the intermediate field and far field zones, respectively. Tables 3.1 to 3.3 show the list of locations where the measurements were taken, followed by the figures (from Figure 3.1 to Figure 3.3).

Table 3.1: List for the locations of readings for ‘Near Field’ at a particular depth

$x/D_p$	$y/D_p$			
0.50	0.00	0.50	1.00	1.50
1.50	0.00	0.50	1.00	1.50
2.50	0.00	0.50	1.00	1.50
3.50	0.00	0.50	1.00	1.50

Table 3.2: List for locations of readings for ‘Intermediate Field’ at a particular depth

$x/D_p$	$y/D_p$				
3.50	0.00	0.75	1.50	2.25	3.00
7.50	0.00	0.75	1.50	2.25	3.00
11.50	0.00	0.75	1.50	2.25	3.00
15.50	0.00	0.75	1.50	2.25	3.00

Table 3.3: List for locations of readings for 'Far Field' at a particular depth

x/Dp	y/Dp				
15.50	0.00	1.00	2.00	3.00	4.00
20.50	0.00	1.00 <td 2.00	3.00	4.00	
25.50	0.00	1.00	2.00	3.00	4.00
30.50	0.00	1.00	2.00	3.00	4.00

The number of readings at each depth of measurement was  $(16 + 20 + 20) = 56$ . These locations and the expected pattern of wake are illustrated in: Figure 3.1, Figure 3.2, and Figure 3.3.

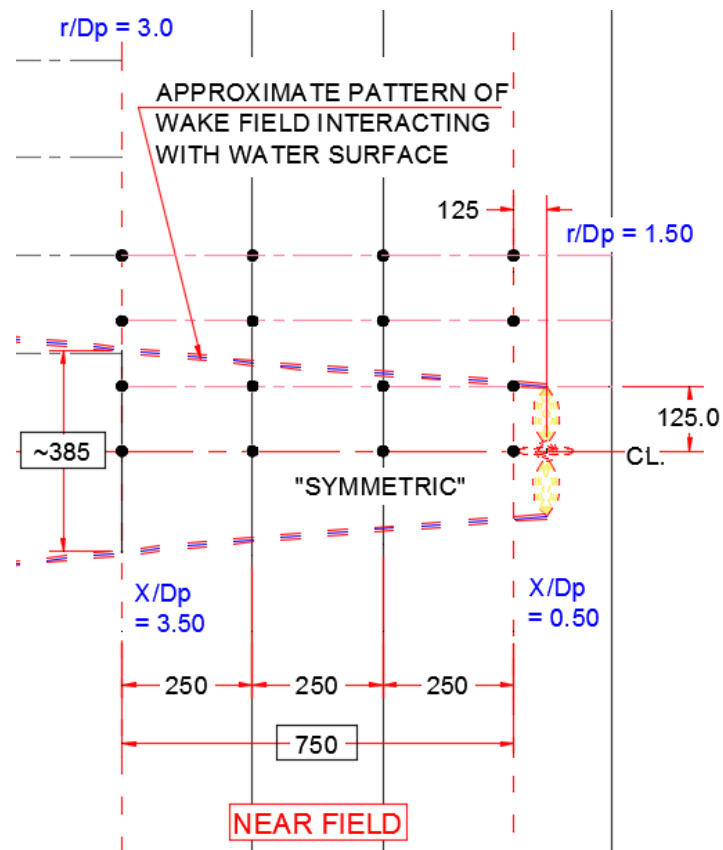


Figure 3.1: Dimension and measurement locations for 'Near Field'

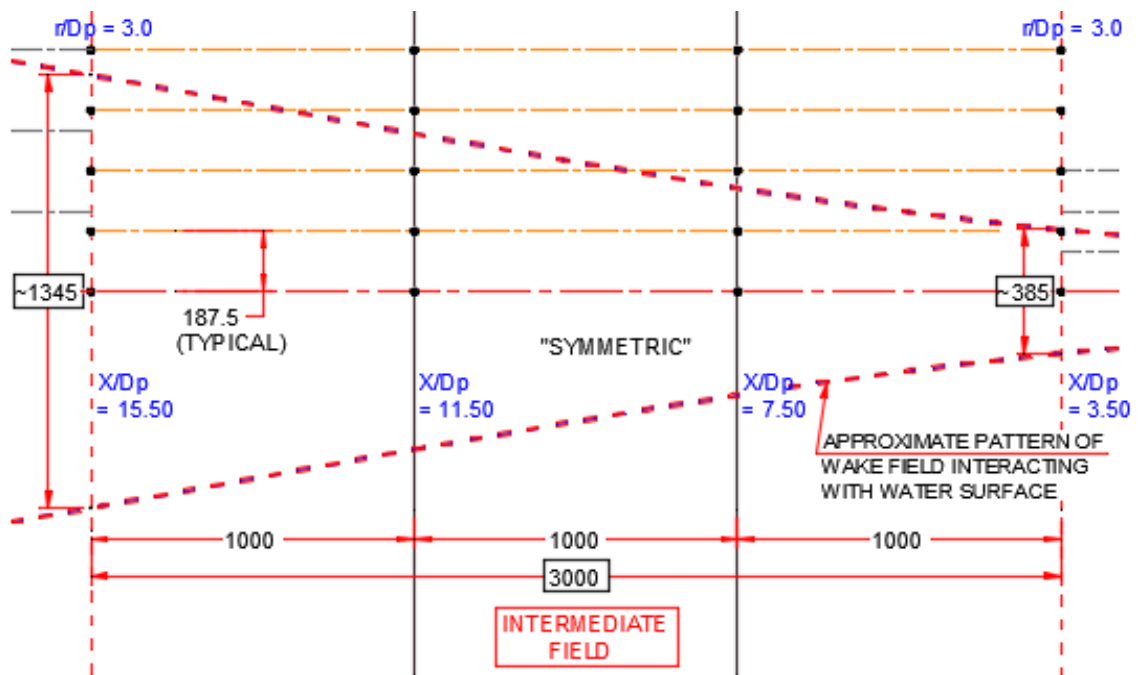


Figure 3.2: Dimension and measurement locations for 'Intermediate Field'

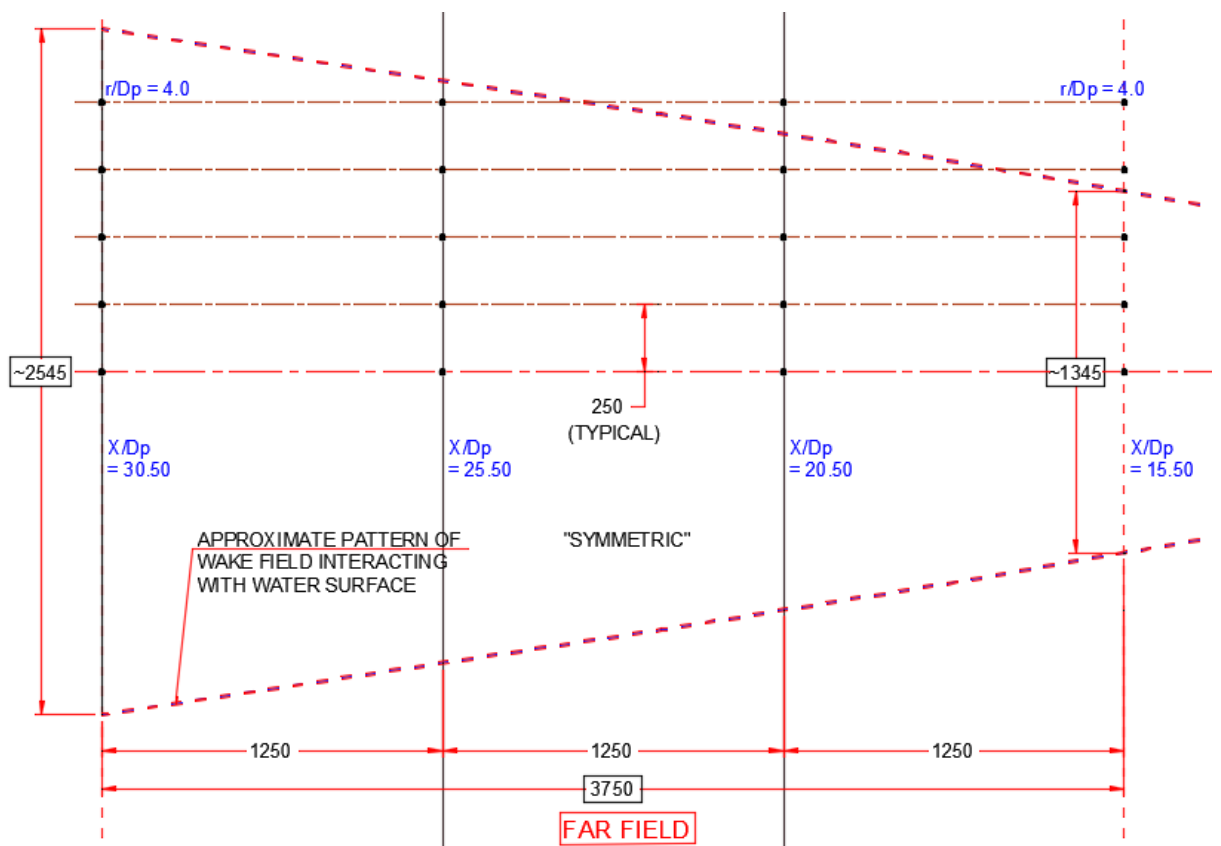


Figure 3.3: Dimension and measurement locations for 'Far Field'

### 3.2 Determination of the Factors and the Design of Experiment

The experiment was designed using the central composite design technique of response surface methodology for 5 levels and 3 factors. The total experimental runs were  $\{2^3 + (2 \times 3) + (1 + 3)\} = 18$ , having 8 factorial runs, 6 axial point runs, and 4 central point runs. Central composite designs require 5 levels for each factor: low axial, low level (-1), center level (0), high level (+1), and high axial. For ensuring a rotatable design, the low axial and the high axial levels were set to (-1.5) and (+1.5) respectively. The factorial runs are the experimental runs for low, center, and high levels. The axial points were tested with only one factor at a low (-1.5) or high (+1.5) axial level, while the remainder were at the center level (0). Three (3) extra center point runs were considered in the experiment to ensure an accurate estimation of experimental error (Montgomery, 2009; Lye, 2011). The 3 factors were: propulsive power of open boat propulsion system in bollard pull condition, which was reported as shaft rotational speed (in rps), inclination angle of propeller (in degree), and depth of submergence of the propeller from the fluid surface (in mm).

In the experiment, the lowest propeller rotational speed was 6.0 rps, which was calculated on the basis of the formula (Verhey, 1983) for Reynolds numbers (propeller Reynolds number ' $Re_{prop}$ ', and flow Reynolds number ' $Re_{flow}$ ') to meet the requirement for minimum  $Re_e$ , for avoiding significant viscous scaling effect. Section 4.2 of the thesis describes the calculation for Reynolds number in detail.

The highest rotational speed in the experiment was 12.0 rps, which was found as the maximum speed at which the open boat propulsion system could be run smoothly. Minimum and maximum inclination angles of the propeller were respectively  $0^\circ$  and  $9^\circ$ . Depth of submergence of the propeller rotation axis from the water surface was

considered from minimum of 200 mm to maximum of 500 mm. The limiting values for the 3 factors were considered to ensure the optimum utilization of the facility. Table 3.4 shows the list of the 5 levels, and the 3 factors used in the experimental study.

Lam et al. (2011 and 2013) reported that after  $x/D_p = 3.68$  tangential velocity becomes less significant, having a magnitude of about 9% of the averaged maximum tangential velocity. Also McGarvey (1996) and Brewster (1997) reported that the radial velocity decays to a very low magnitude (near to zero) after  $x/D_p = 1.50$ , and it decays by about 80% within  $x/D_p = 0.30$  from the efflux plane ( $x/D_p = 0$ ). Hence, the effects of radial and tangential components of velocity are insignificant after  $x/D_p = 1.50$  and  $x/D_p = 3.68$ , respectively. The near field considered in the experiment was located within  $x/D_p = 0.5$  and  $3.5$ , where the maximum portion of the tangential and the radial velocities were expected to decay. The axial component of velocity dominates throughout a considerable region of a propeller wake field, which is of particular interest for the present study. During the experiment besides measuring the axial velocity in the propeller wake, another component of velocity was measured in the plane perpendicular to the axial velocity, which is reported as the tangential / radial component of velocity in the thesis and the test report (Amin et al., 2017). The experimental results were analyzed only for the axial velocity of flow.

Table 3.4: List of factors and levels considered to design the experiment

Factors	Levels				
	Low axial (-1.5)	Low (-1)	Center (0)	High (+1)	High axial (+1.5)
Power rotational speed (rps)	6.0	7.0	9.0	11.0	12.0
Propeller inclination (degree)	0.0	1.5	4.5	7.5	9.0
Submergence of propeller (mm)	200	250	350	450	500

### 3.3 Experimental Set-up

The experiment was done in the tow tank ( $L_T \times B_T \times D_T = 58.27 \times 4.57 \times 3.04$  meter) of the OERC (Ocean Engineering Research Centre). A list of equipment and facilities that were used for the experiment can be listed below:

1. A propeller of B4-55 series of diameter  $\phi 250$  mm;
2. Open boat propulsion unit, and the frame to mount and to operate the open boat unit on the OERC tank carriage;
3. EMCM equipment, the tank platform, and the frame for installation and operation of EMCM sensors mounted on the platform;
4. OERC Data acquisition system / terminal (RS 232,  $\pm 5$  V) with a desktop computer to record the experimental data collected by using EMCM sensors;
5. Linear variable displacement transducer, to measure the transverse displacement of EMCM sensors from datum (center of wake field), etc.

This section contains a brief description of the major systems and facilities that were used during the experiment. The overall set-up for the experiment is shown by a schematic diagram in Figure 3.4, where all the major components of the entire set-up are shown.

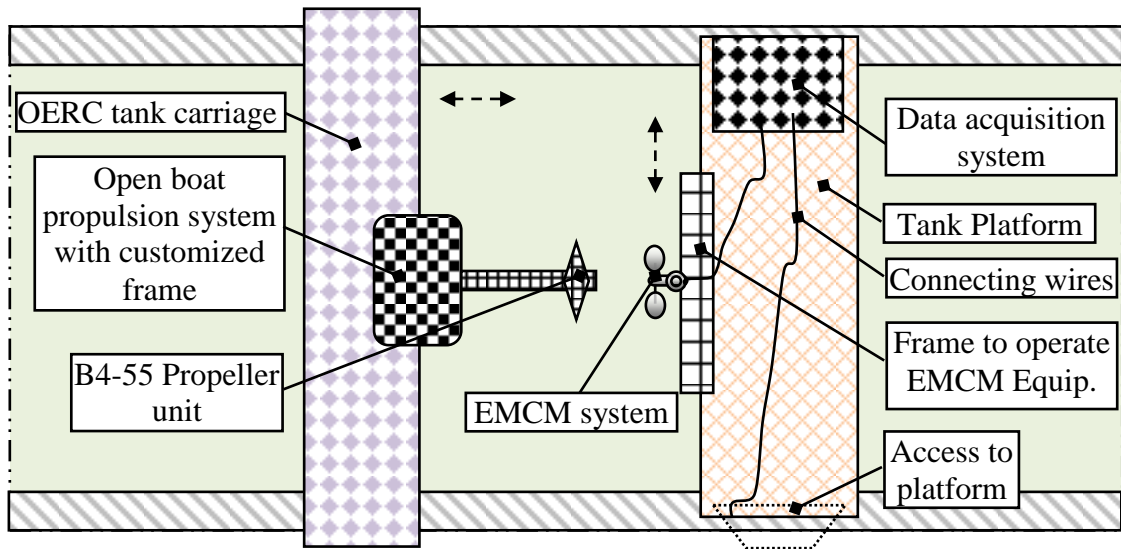


Figure 3.4: Schematic diagram for the experimental set-up

The experimental data along  $x/D_p$  were collected by moving the OERC tank carriage back and forth following a pre-marked scale, the data along  $y/D_p$  were collected by sliding the EMCM sensors along the tank platform by using the frame built to operate the EMCM equipment, and the data along  $d/D_p$  were collected by adjusting the position (vertically) of the mounting rod installed to the built-in frame of sensors. Propeller inclination ' $\theta$ ' was adjusted by using the customized frame to install the open boat unit on the tank carriage. Propeller depth of submergence ' $H$ ' was adjusted by adjusting the water depth of OERC tank. The propeller shaft speed (rotational) ' $n$ ' was measured with a tachometer.

### 3.3.1 Open Boat Propulsion System

The open boat propulsion system integrates all the equipment that was used to generate the propeller wake under a particular propulsion condition. This unit consisted of the propeller, the open boat propulsion unit, and the frame to put the open boat unit on the carriage installed on the sidewall of the OERC tow tank. The propeller was a B4-55 series of diameter  $\text{Ø}250$  mm. The frame had the mechanism of adjusting the inclination of propeller. The power of the unit was adjustable, which was related to the rotational speed of propeller. The unit was pre-calibrated, and thus it was not calibrated prior to the experiment. Figure 3.5 shows the image of the integrated system, where the different components of the open boat propulsion system are highlighted.

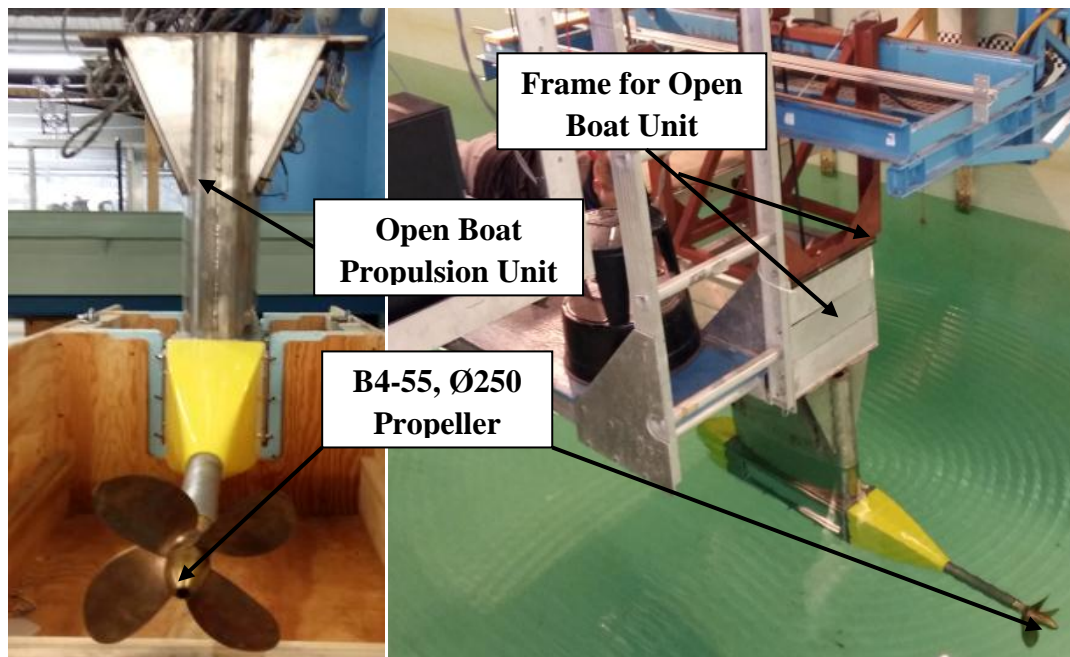


Figure 3.5: Open boat propulsion system

### 3.3.2 EMCM System

The EMCM system was used to measure and store the experimental data during the experiment. This system included: EMCM package (EMCM sensors, built-in mounting to maintain the orientation of sensors and a rod, batteries, other accessories) to measure the mean axial velocity of flow, the spatial distribution of velocity, and the variability of flow, a frame to mount and operate the sensors, a linear displacement transducer to measure the transverse displacement of the sensors, OERC tank platform to support the entire arrangement under the EMCM system, and connecting wires. The tank platform was installed along the breadth of the tank (4.57 meter), on the top of which the EMCM equipment with the supporting frame, and the data acquisition system were installed. The EMCM sensors were facilitated to slide on the frame installed along the tank platform, with respect to a datum. The datum was marked at the centre of the wake field ( $y = 0$ ). Thus the readings along the transverse direction of the propeller wake (along  $y/D_p$ ) were collected by sliding the sensors following a pre-marked scale on the frame. Figure 3.6 shows the major components of the EMCM package, a frame to mount and operate the sensors, and the tank platform that supported the components of the system.

The EMCM package was new equipment, and it was pre-calibrated by the vendor. The certificate of calibration for the equipment is shown in Appendix 'E'. The vendor also provided the calculation for calibration of the equipment, which was followed prior to the experiment for doing the calibration of the equipment.

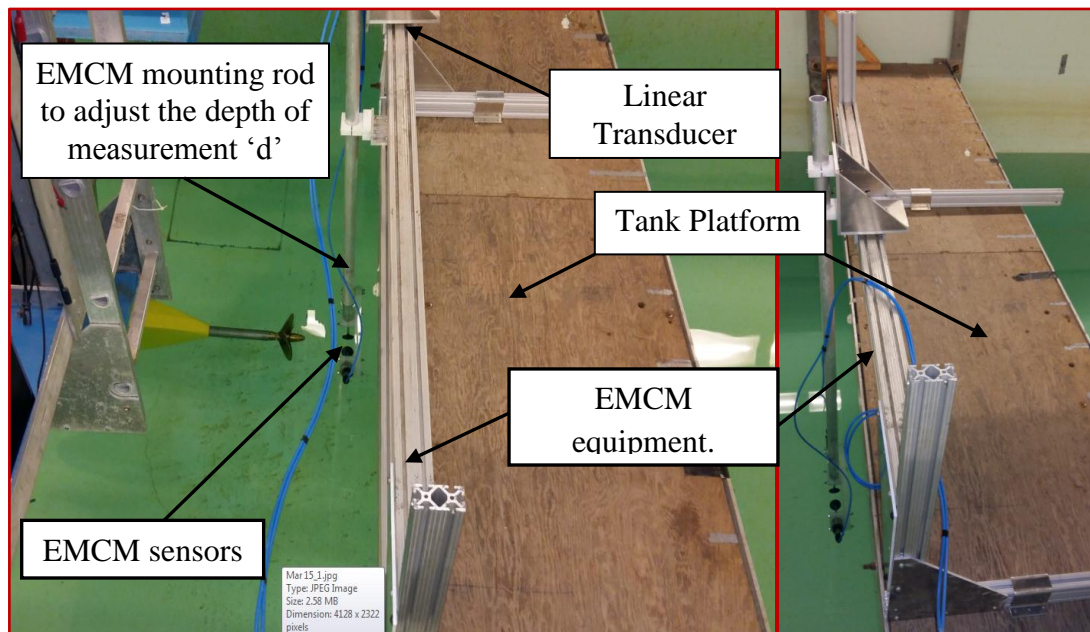


Figure 3.6: EMC system, supporting frame, and tank platform

The sensors were mounted by maintaining a consistent orientation by using a built-in mounting provided by the supplier with the EMC package. Then a rod was installed to adjust the depth of measurement 'd'. Figure 3.7 shows the EMC sensors with built-in frame, and an added rod to adjust 'd'. The disks (dia. 5.5 cm) of the sensors were required to be submerged into water in order to get the reading accurately.

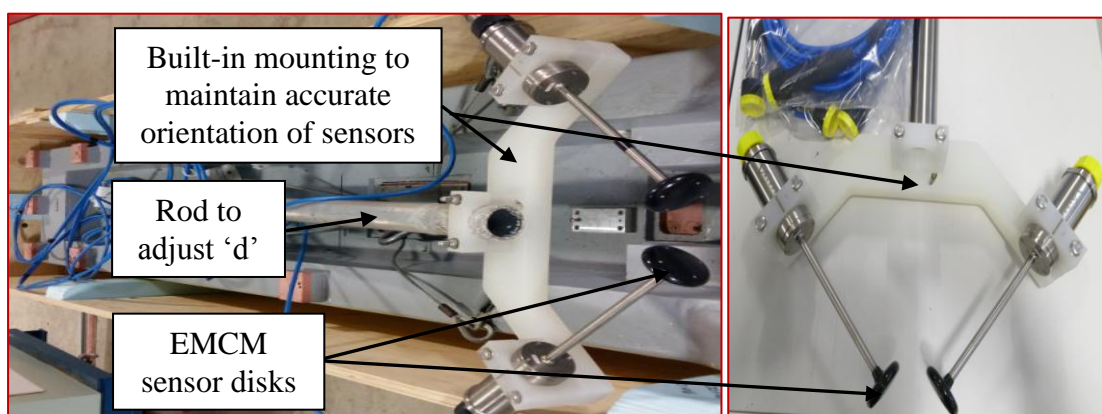


Figure 3.7: EMC sensors and built-in frame, except batteries and other accessories

### 3.3.3 Data Acquisition System

This system was used to collect and store the experimental data during the experiment. The system was part of the in-house facilities of OERC. RS-232 data acquisition system was used to record the output received from the sensors.

The output of the EMCM equipment was of analogue type ranging from -5 V to +5 V, which was converted to match for the range from -5.0 m/s to +5.0 m/s output, by using the software of the system. The output received in 'm/s' was the velocity of flow. Figure 3.8 shows the desktop computer and other accessories of RS232 system, which were used to collect and record the experimental data.



Figure 3.8: Data acquisition system

## CHAPTER 4 - EXPERIMENTAL RESULTS

### 4.1 Overview

This section of the thesis covers the description of the results that were analyzed using the experimental data, which are presented in the test report (Amin et al., 2017). Some of the results presented in the test report are used, to present the different aspects of data analysis with a detailed description of the study. The results of the experiment are presented in 2 parts. The first part (Section 4.2) illustrates the assessment for the viscous scaling effect of the results, and compares the measured and the calculated maximum mean axial flow velocities. The comparison is made for the different propeller rotational speeds that were used in the experiment.

The experimental results that are presented in the second part (Section 4.3) are used to explain the various aspects of data analysis. The detailed results of the experiment for all the 18 experimental configurations are incorporated in the test report (Amin et al., 2017), but no detailed descriptions or data analyses are given in that report. Analyses are done only for the axial component of fluid velocity.

In summary, the following studies are done and reported in the thesis:

- Section 4.2 contains the assessment of the viscous scaling effect, and compares the measured maximum fluid velocities with the velocities calculated using the formulae for efflux velocity, as mentioned above.
- Section 4.3 covers the various studies carried out using the experimental results.
- In Section 4.3.1, an assessment is presented for the mean axial velocity along the longitudinal positions downstream of wake field, and the variability of the flow. As a criterion of measuring the variability of flow, standard deviation is used and analysis

has been shown for 3 experimental cases in the thesis. Results for all the 18 cases are shown in Amin et al. (2017).

- In Section 4.3.2, the experimental data are assessed to check the individual influence of the 3 factors considered in the experiment. The OFAT (One Factor At a Time) approach is used, where the change of the response variable (non-dimensionalized velocity component) is presented for the change of a particular factor. The mean axial velocities are considered along  $x/D_p$ . In Section 4.3.6 and Section 4.3.7, some analyses are shown to explain the interaction effects of the factors on the response variable.

- In Section 4.3.3, a comparison of the experimental results to the results obtained from the semi-empirical mathematical model developed by Bastin (2014) is shown for 3 conditions.

- In Section 4.3.4, an assessment of the mean velocity of flow as a function of transverse positions (along  $y/D_p$ ) is presented for 3 cases.

- In Section 4.3.5, analyses are done using the data collected at the level closest to the fluid surface (at  $0.25D_p$ ) in order to investigate the behavior of the axial fluid velocity component against individual factor. The approach is the same as OFAT.

- Section 4.3.6 describes the functional relationship among the non-dimensionalized factors  $\left(\frac{nD_p^2}{v}, \theta, \frac{H}{D_p}\right)$ , and the non-dimensionalized response variables of the experiment. The response variables of the experiment are: the mean axial fluid velocity  $\left(\frac{V_a D_p}{v}\right)$ , the tangential / radial component of fluid velocity  $\left(\frac{V_{t/r} D_p}{v}\right)$ , the corresponding variability  $\left(\frac{\sigma D_p}{v}\right)$  of flow; which also depend on the location of the response variable  $\left(\frac{x}{D_p}, \frac{y}{D_p}, \frac{d}{D_p}\right)$ .

- Section 4.3.7 describes the relationship among the response variable, depth of measurement ( $d/D_p$ ) and the factors, particularly for a level near the fluid surface.

## 4.2 Scaling Effect Requirement and Measurement of Maximum Mean Axial Velocity

Firstly, data were collected to calculate the thrust and torque coefficients of the propeller to calculate the propeller and flow Reynolds numbers ( $Re_{prop}$  and  $Re_{flow}$ ). As the experiment was designed at 5 levels, calculations for the coefficients are done for 5 different rotational speeds of the propeller, as shown in Table 4.1. The average of the thrust and the torque coefficients were 0.306 and 0.041 respectively, for the 250 mm diameter B4-55 propeller that was used for the experiment. Then  $Re_{prop}$  and  $Re_{flow}$  are calculated using the formulae (Verhey, 1983).

Verhey (1983) suggested that the scaling effect due to viscosity is negligible, if the Reynolds number of the propeller ( $Re_{prop}$ ) and the Reynolds number of the flow ( $Re_{flow}$ ) are greater than  $7 \times 10^4$  and  $3 \times 10^3$  respectively, for a propeller wake. Verhey used the formulae:  $Re_{flow} = \frac{V_0 D_p}{\nu}$  and  $Re_{prop} = \frac{n L_m D_p}{\nu}$ . Where  $V_0$  = efflux velocity of propeller jet;  $D_p$  = Propeller diameter;  $n$  = propeller rotational speed (rps);  $L_m$  = length term dependent on blade area ratio ( $\beta$ ), number of blades of propeller ( $N$ ), diameter of hub ( $D_h$ ) and  $D_p$ .  $L_m$  is defined (Blaauw and van de Kaa, 1978) as:  $L_m = \beta \cdot D_p \cdot \pi \cdot \left\{ 2N \left( 1 - \frac{D_h}{D_p} \right) \right\}^{-1}$ . Using the mentioned formulas, the  $Re$  values were calculated as:  $Re_{flow} = 2.87 \times 10^5$  and  $Re_{prop} = 8.54 \times 10^4$ , which are larger than the corresponding minimum required values. Therefore, the results of the experiment

meet the requirements for minimum Reynolds numbers for neglecting viscous scaling effect.

Table 4.1: Results for thrust and torque coefficient

Propeller Rotational Speed, n (rps)	Propeller Power, P (Watt)	Thrust, T (N)	Torque, Q (N-m)	Thrust Coefficient, $C_t$	Torque Coefficient, $C_q$
6.0	57.7	42.218	1.530	0.300	0.044
7.0	87.7	57.175	1.995	0.299	0.042
9.0	182.2	99.663	3.222	0.315	0.041
11.0	317.6	146.434	4.596	0.310	0.039
12.0	408.7	171.567	5.422	0.305	0.039

Table 4.2: Calculation of Reynolds numbers

Propeller Rotational Speed, n (rps)	Thrust Coefficient, $C_t$	Torque Coefficient, $C_q$	Propeller Reynold's number $Re_{prop}$	Flow Reynold's number $Re_{flow}$
6.0	0.300	0.044	8.54E+04	2.87E+05
7.0	0.299	0.042	9.96E+04	3.33E+05
9.0	0.315	0.041	1.28E+05	4.40E+05
11.0	0.310	0.039	1.56E+05	5.34E+05
12.0	0.305	0.039	1.71E+05	5.78E+05

Then as a simple check of the reliability of the EMCM sensors, the measured maximum mean axial velocities are compared with the calculated efflux velocities for

the 5 rotational speeds considered in the experiment. Efflux velocities were calculated by using the following formula, as described in Section 2.2:

$$V_0 = 1.59nD_P\sqrt{C_t}$$

Table 4.3: Comparison results for the measured maximum axial velocity for flow and corresponding calculated efflux velocity

Propeller Rotational Speed, n (rps)	Thrust Coefficient, $C_t$	Calculated Efflux Velocity, $V_{0_c}$ (m/s)	Measured Efflux Velocity, $V_{0_m}$ (m/s)	Difference (%)
6.0	0.300	1.307	1.257	3.82%
7.0	0.299	1.521	1.450	4.65%
9.0	0.315	2.008	1.859	7.41%
11.0	0.310	2.434	2.254	7.39%
12.0	0.305	2.634	2.419	8.17%

It is noted from Table 4.3 that the differences between the measured values and the calculated values are not large. The maximum difference is 8.17% for the highest rotational speed. Also, all measured values are slightly lower than the corresponding calculated values, which may be due to the difficulty of placing the EMCM sensors as close to the propeller efflux plane as it should be, in order to measure the efflux velocity accurately. If the sensors were put closer to the rotating propeller to read the fluid axial velocity, then the measured maximum axial flow velocities might be closer to the calculated efflux velocities.

### 4.3 Analysis of Results of the Experiment

This section describes the various analyses that were done on the data collected during the experiments, as outlined in Section 4.1.

#### 4.3.1 Characteristics of the Mean Axial Velocity and the Variability of Flow (Standard Deviation) along $x/D_p$

Assessments of the mean axial velocity and the variability of flow are carried out for three cases, among which only one case is shown in this section. The other two cases are presented in Appendix 'A'. Also the test report (Amin et al., 2017) contains the plots for all the cases, for the same locations (at three depths of measurement and at  $y/D_p = 0.0$ , or centre of the wake field). Here 'y' is the distance transversely from the center axis of the wake field (propeller), as described in Section 3.1. The case that is shown in this section is for the configuration of factors: propeller rotational speed = 9.0 rps, inclination angle =  $4.5^\circ$ , and depth of submergence of propeller rotation axis = 350 mm. There are three plots (from Figure 4.1 to Figure 4.3) are developed for three depths of measurement (at  $0.25D_p$ ,  $0.55D_p$  and  $1.05D_p$  from fluid surface) at centre of the wake field, showing the 'mean velocity' and 'mean  $\pm$  standard deviation' against  $x/D_p$ . As a measurement of variability of the flow, standard deviation was measured. In the analysis, only the axial velocity is considered. In the plots ' $V_a$ ' and ' $\sigma$ ' are the mean axial velocity and the standard deviation as measured during experiment, which are non-dimensionalized.

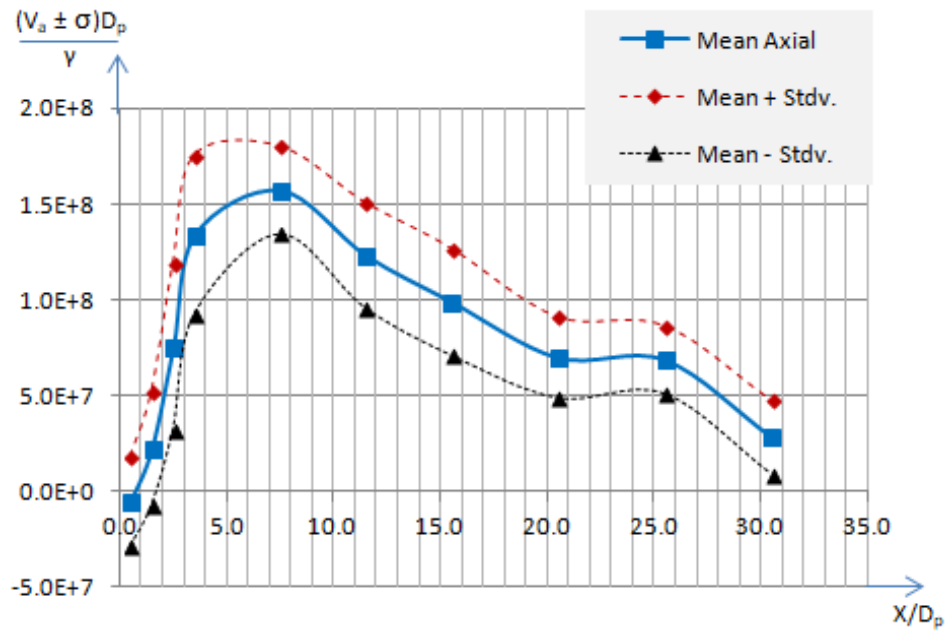


Figure 4.1: Mean axial velocity, and mean axial velocity  $\pm$  standard deviation as a function of  $x/D_p$  at a depth  $0.25D_p$  and transversely at  $y/D_p = 0.0$

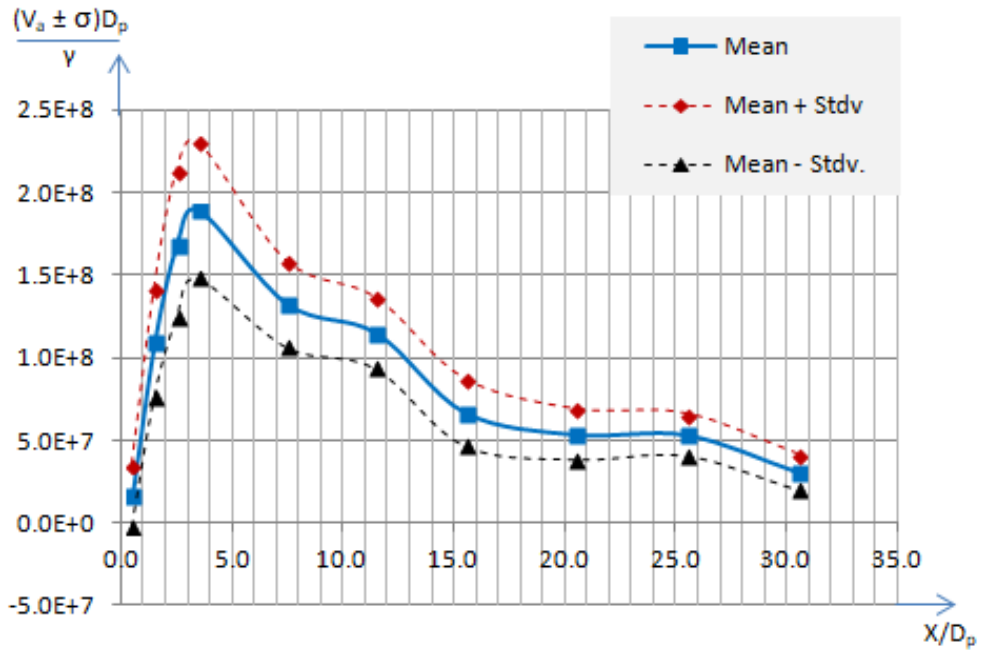


Figure 4.2: Mean axial velocity, and mean axial velocity  $\pm$  standard deviation as a function of  $x/D_p$  at a depth  $0.55D_p$  and transversely at  $y/D_p = 0.0$

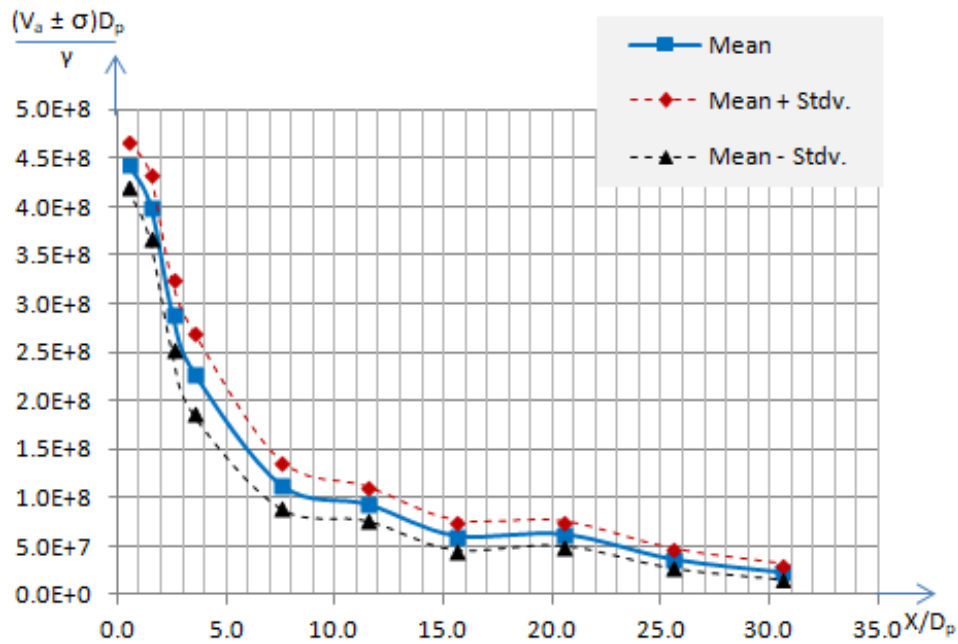


Figure 4.3: Mean axial velocity, and mean axial velocity  $\pm$  standard deviation as a function of  $x/D_p$  at a depth  $1.05D_p$  and transversely at  $y/D_p = 0.0$

#### 4.3.2 Influence of Factors on Propeller Wake Field Individually

This section of the thesis describes the analysis that is carried out to illustrate the influence of individual factors on the wake velocity field. The approach to do the analysis is known as OFAT (One Factor At a Time), where only one factor is changing, keeping the other two factors unchanged. Among 18 experimental configurations, four are CP (Centre Point) configurations, having the same combinations of factors. The average values of the four CP configurations (experimental run #4, #7, #15 and #17) are considered in the analysis. Thus there are basically 15 unique experimental configurations that were considered in the experiment. Among the 15 combinations, three are considered for each factor of the experiment to apply OFAT, and to illustrate the individual effect of the three factors considered in the experiment. Table 4.4 shows the combination of experimental

configurations, which are considered to demonstrate the influence of each factor individually on the wake velocity field.

Table 4.4: Combinations of experimental runs considered to apply OFAT in order to illustrate the individual effect of factors

4.3.2a Influence of Propeller rotational speed 'n' on the wake velocity field			
Selected Runs	'n' in rps	' $\theta$ ' in degree	'H' in mm
#1	6	4.5	350
Average of #4, #7, #15 & #17	9	4.5	350
#16	12	4.5	350
4.3.2b Influence of Propeller inclination angle ' $\theta$ ' on the wake velocity field			
Selected Runs	'n' in rps	' $\theta$ ' in degree	'H' in mm
#5	9	0.0	350
Average of #4, #7, #15 & #17	9	4.5	350
#2	9	9.0	350
4.3.2c Influence of Propeller depth of submergence 'H' on the wake velocity field			
Selected Runs	'n' in rps	' $\theta$ ' in degree	'H' in mm
#14	9	4.5	200
Average of #4, #7, #15 & #17	9	4.5	350
#13	9	4.5	500

To illustrate the individual effect of factors, plots are developed only at  $y/D_p = 0$  or centre of the wake field. More plots are shown in Appendix 'B' for a different transverse location (250 mm offset from the centre of the wake field).

Firstly in the plots, from Figure 4.4a to Figure 4.6a, the trend of mean axial velocity is shown along  $x/D_p$  for three different propeller rotational speeds (6 rps, 9 rps and 12 rps) at the three depths of measurement ( $0.25D_p$ ,  $0.55D_p$  and  $1.05D_p$ ) respectively, by applying the principle of OFAT. Then similarly, in the next three plots (from Figure 4.4b to Figure 4.6b), the change of axial velocity in terms of  $x/D_p$  is shown at three different propeller inclinations ( $0^\circ$ ,  $4.5^\circ$  and  $9^\circ$ ). The last three plots of the section, from Figure 4.4c to 4.6c, the change of axial velocity with  $x/D_p$  is shown at three different propeller depths of submergences (200 mm, 350 mm and 500 mm) for three depths of measurement.

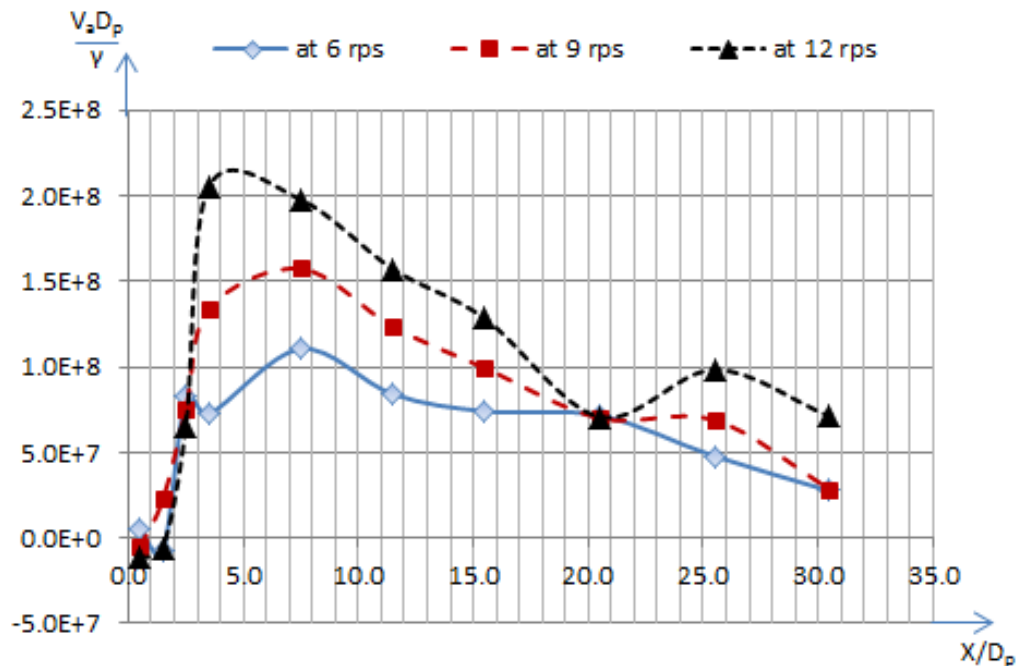


Figure 4.4a: Mean axial velocity along  $x/D_p$  at different rotational speeds for  $H = 350$  mm and  $\theta = 4.5^\circ$  at a depth of  $0.25D_p$  from the water surface and at  $y/D_p = 0.0$

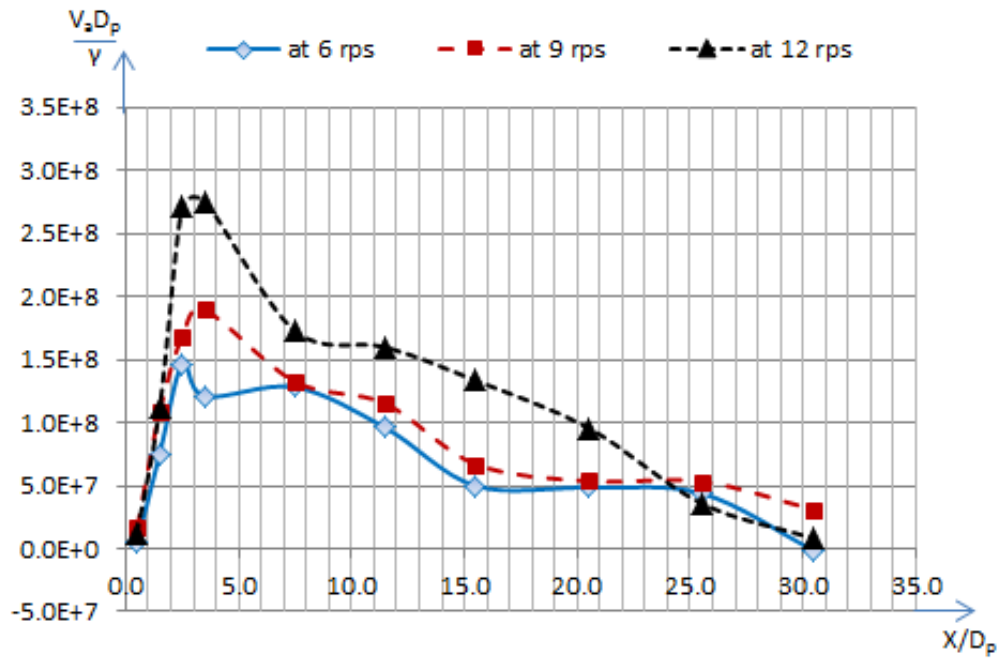


Figure 4.5a: Mean axial velocity at different rotational speeds along  $x/D_p$  for  $H = 350$  mm and  $\theta = 4.5^\circ$  at a depth of  $0.55D_p$  from water surface and at  $y/D_p = 0.0$

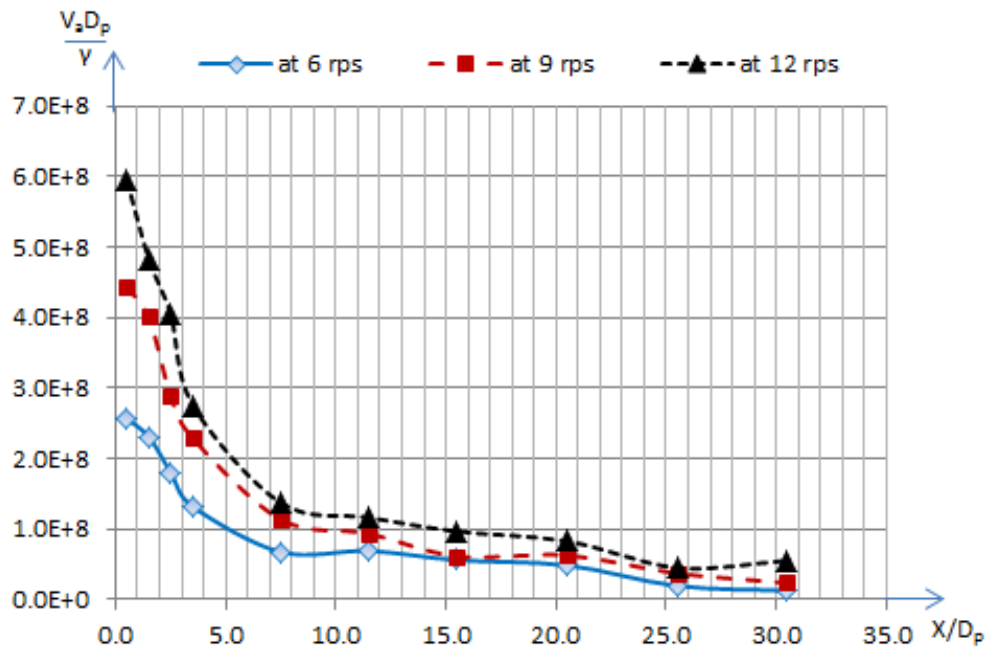


Figure 4.6a: Mean axial velocity at different rotational speeds along  $x/D_p$  for  $H = 350$  mm and  $\theta = 4.5^\circ$  at a depth of  $1.05D_p$  from water surface and at  $y/D_p = 0.0$

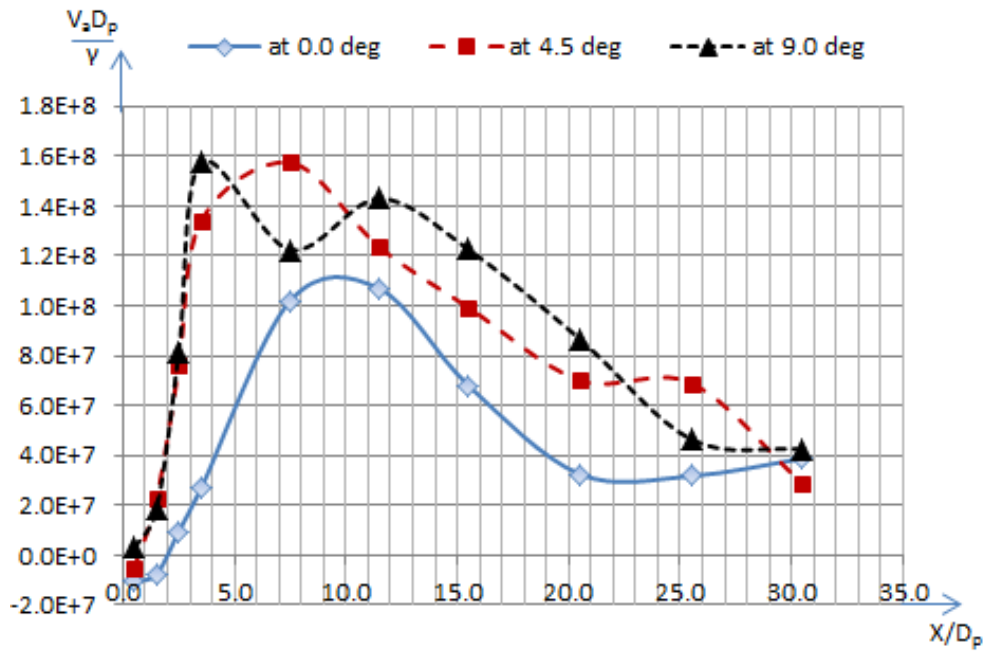


Figure 4.4b: Mean axial velocity at different propeller inclinations along  $x/D_p$  for  $H = 350$  mm and  $n = 9$  rps at a depth of  $0.25D_p$  from water surface and at  $y/D_p = 0.0$

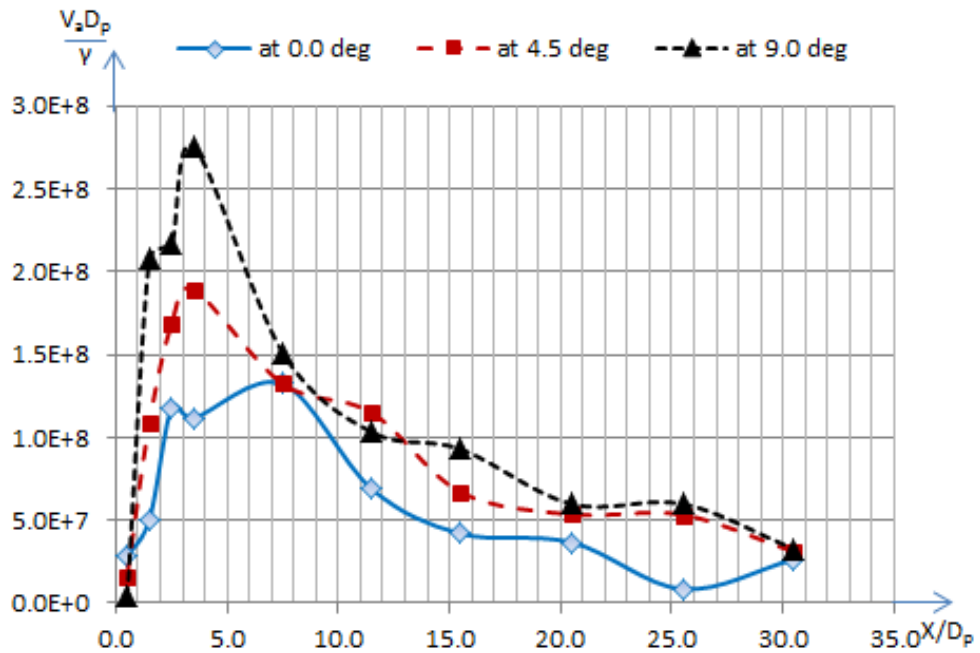


Figure 4.5b: Mean axial velocity at different propeller inclinations along  $x/D_p$  for  $H = 350$  mm and  $n = 9$  rps at a depth of  $0.55D_p$  from the water surface and at  $y/D_p = 0.0$

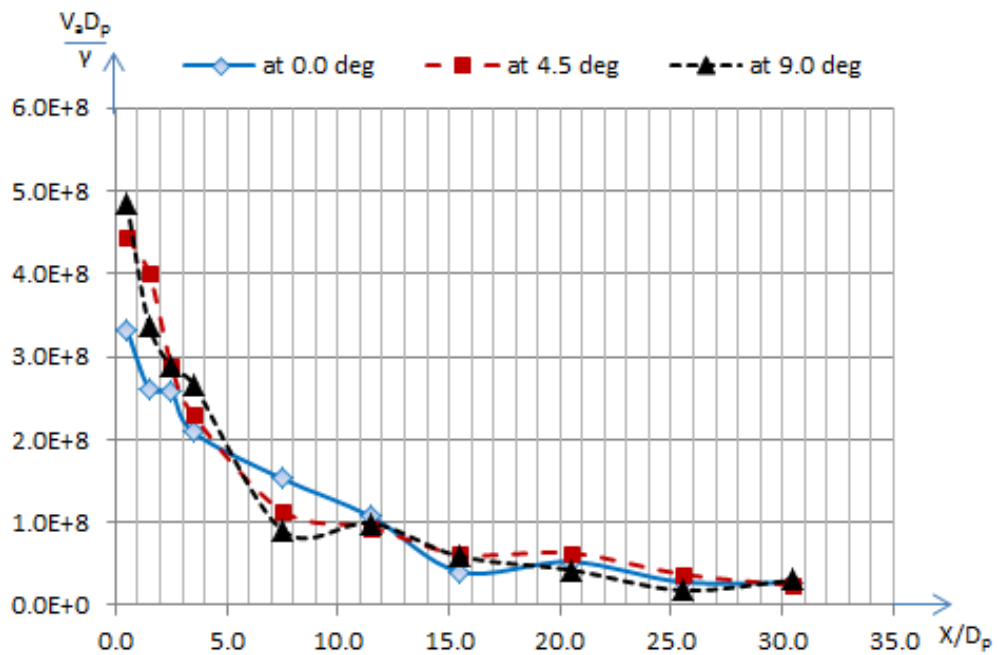


Figure 4.6b: Mean axial velocity at different propeller inclinations along  $x/D_p$  for  $H = 350$  mm and  $n = 9$  rps at a depth of  $1.05D_p$  from the water surface and at  $y/D_p = 0.0$

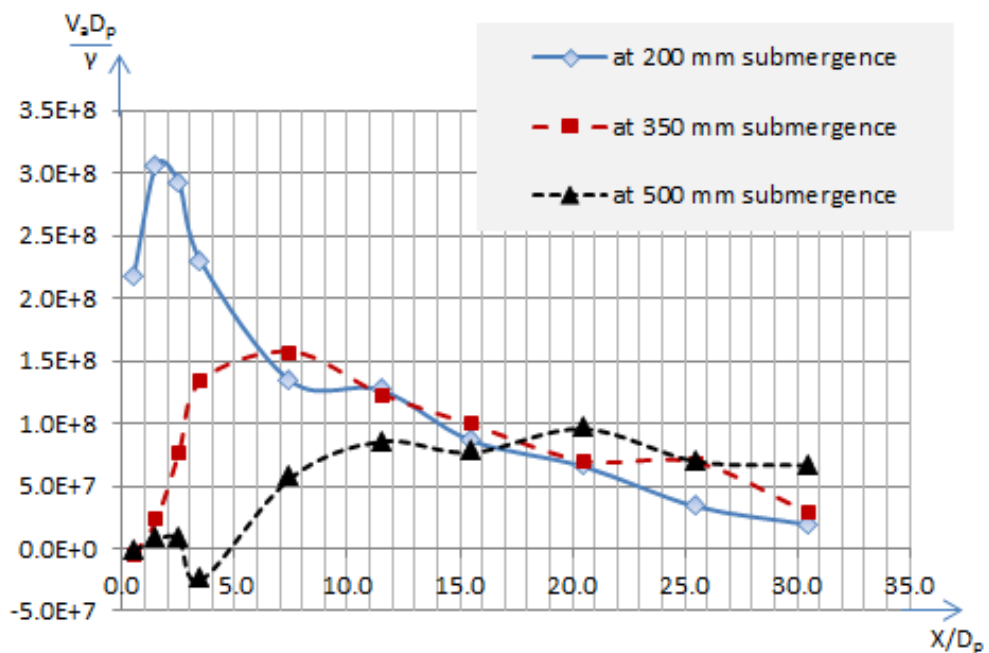


Figure 4.4c: Mean axial velocity at different propeller submergences along  $x/D_p$  for  $\theta = 4.5^\circ$  and  $n = 9$  rps at a depth of  $0.25D_p$  from the water surface and at  $y/D_p = 0.0$

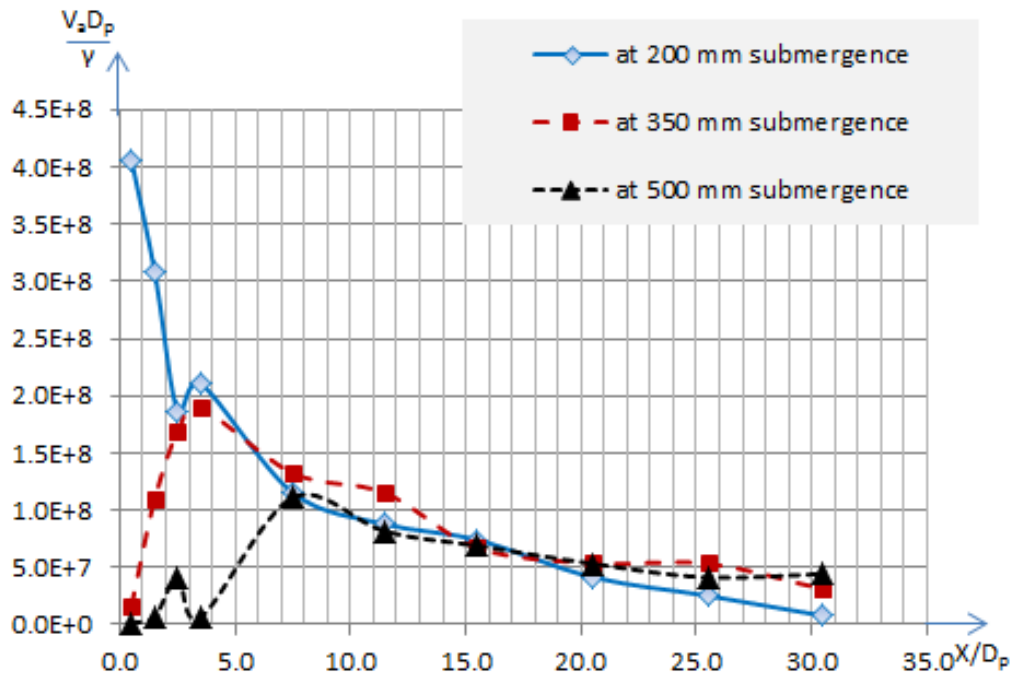


Figure 4.5c: Mean axial velocity at different propeller submergences along  $x/D_p$  for  $\theta = 4.5^\circ$  and  $n = 9$  rps at a depth of  $0.55D_p$  from the water surface and at  $y/D_p = 0.0$

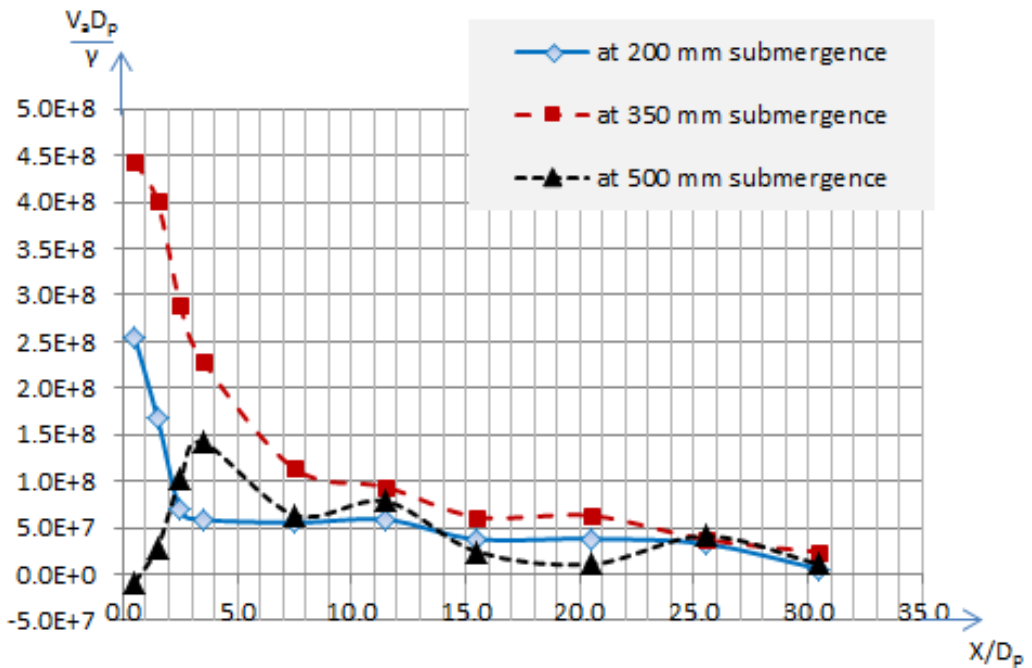


Figure 4.6c: Mean axial velocity at different propeller submergences along  $x/D_p$  for  $\theta = 4.5^\circ$  and  $n = 9$  rps at a depth of  $1.05D_p$  from the water surface and at  $y/D_p = 0.0$

### 4.3.3 Comparison of Experimental Results with the Bastin (2014) Mathematical Model (TB Model)

The experimental results were compared with the simulated results obtained by using the semi-empirical mathematical model of Bastin (2014) for three cases. In this section, only one case is shown and the other two cases are shown in Appendix ‘C’. The plots below illustrate the mean axial velocity (m/s) along  $x/D_p$  at the centre of the wake field for the configuration: shaft rotational speed = 9 rps, propeller inclination =  $4.5^\circ$ , and propeller depth of submergence = 350 mm.

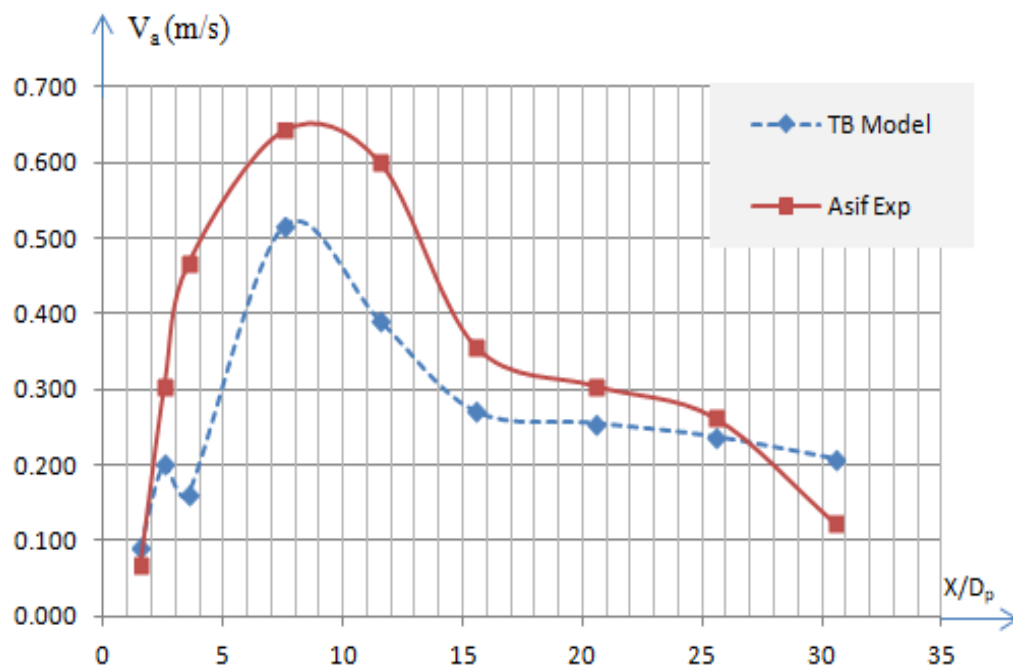


Figure 4.7a: Comparison plot for the mean axial velocity (m/s) along  $x/D_p$  at a depth of  $0.25D_p$  from the water surface and at  $y/D_p = 0.0$

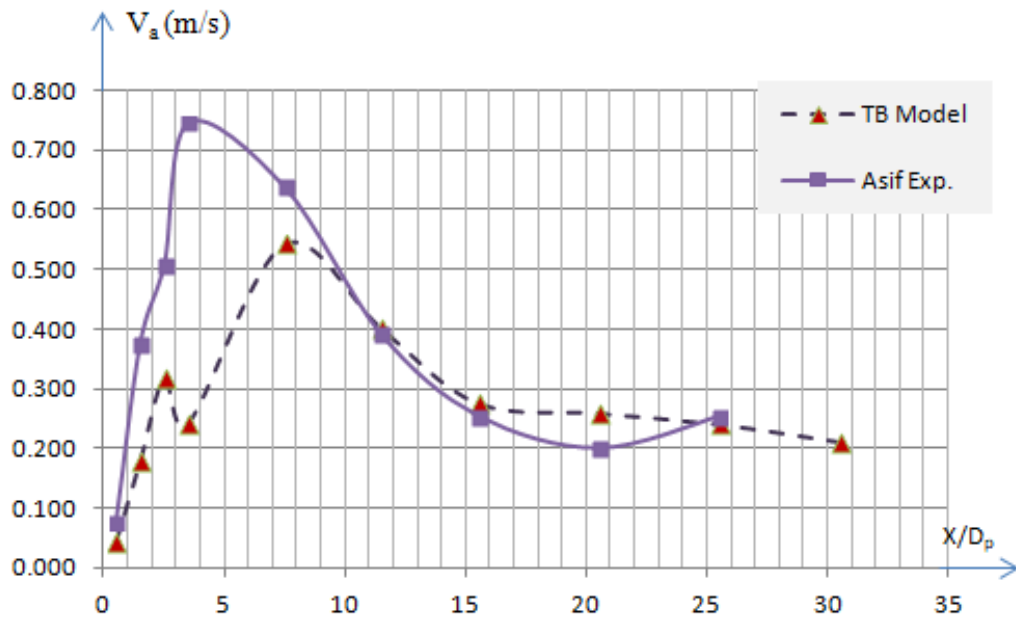


Figure 4.7b: Comparison plot for the mean axial velocity (m/s) along  $x/D_p$  at a depth of  $0.55D_p$  from the water surface and at  $y/D_p = 0.0$

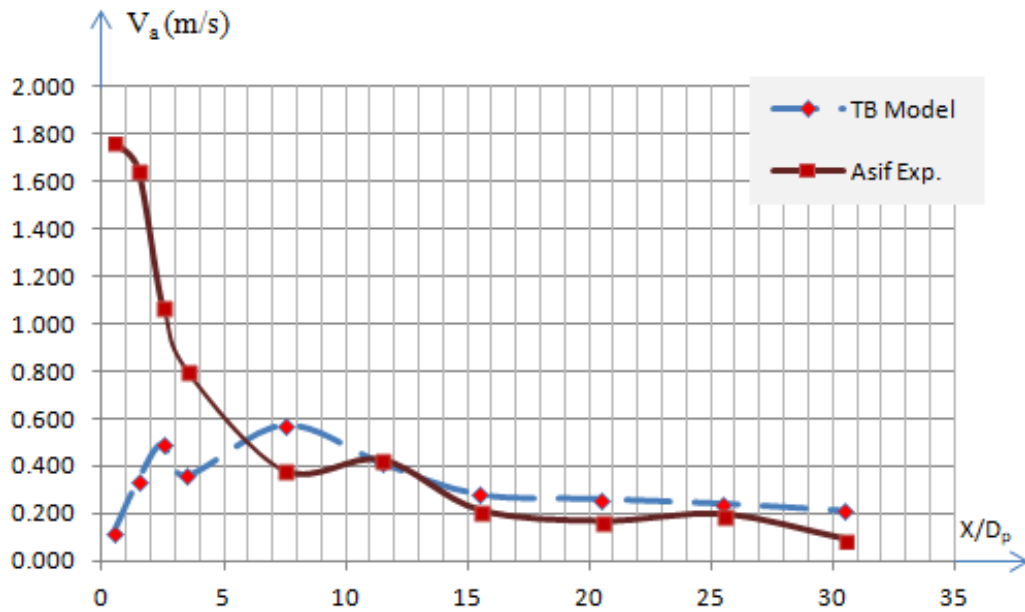


Figure 4.7c: Comparison plot for the mean axial velocity (m/s) along  $x/D_p$  at a depth of  $1.05D_p$  from the water surface and at  $y/D_p = 0.0$

#### 4.3.4 Mean Axial Velocity along transverse locations (along $y/D_p$ )

In this section, the change of mean axial velocity along  $y/D_p$  for all the longitudinal locations (at  $x/D_p$ ) where measurements were taken are shown for one experimental configuration of factors, which is: shaft rotational speed = 9 rps, propeller inclination =  $4.5^\circ$ , and propeller depth of submergence = 350 mm. All the longitudinal locations considered in the experiment, where the measurements were taken are: at  $x/D_p = 0.5, 1.5, 2.5, 3.5, 7.5, 11.5, 15.5, 20.5, 25.5$  and  $30.5$ . Plots for all these ten locations are presented showing the mean axial velocities along  $y/D_p$  for the three depths of measurements: at  $d/D_p = 0.25, 0.55$  and  $1.05$ .

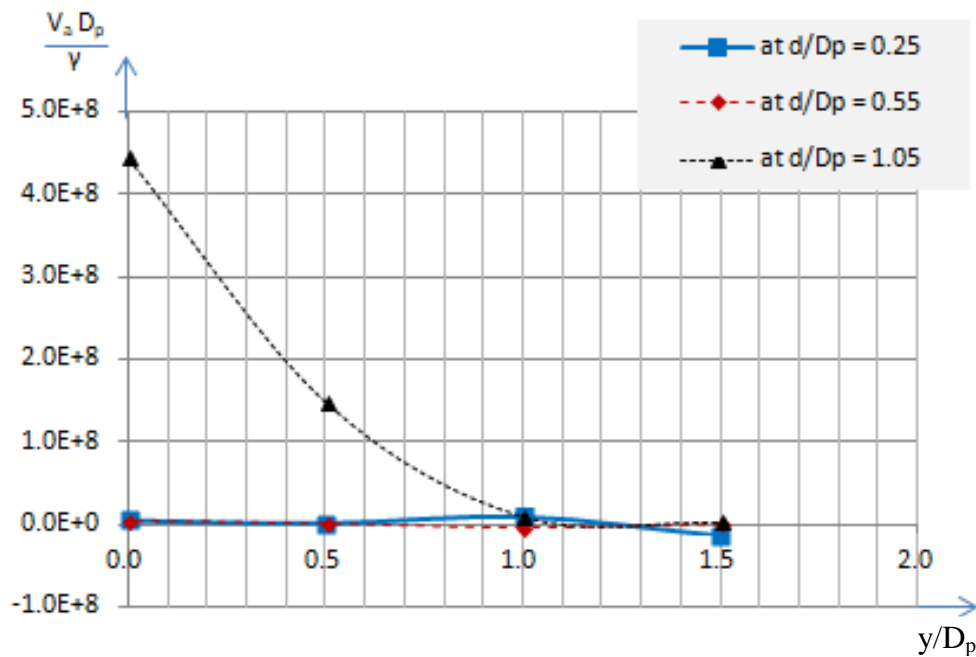


Figure 4.8a: Mean axial velocity along  $y/D_p$  at  $x/D_p = 0.5$

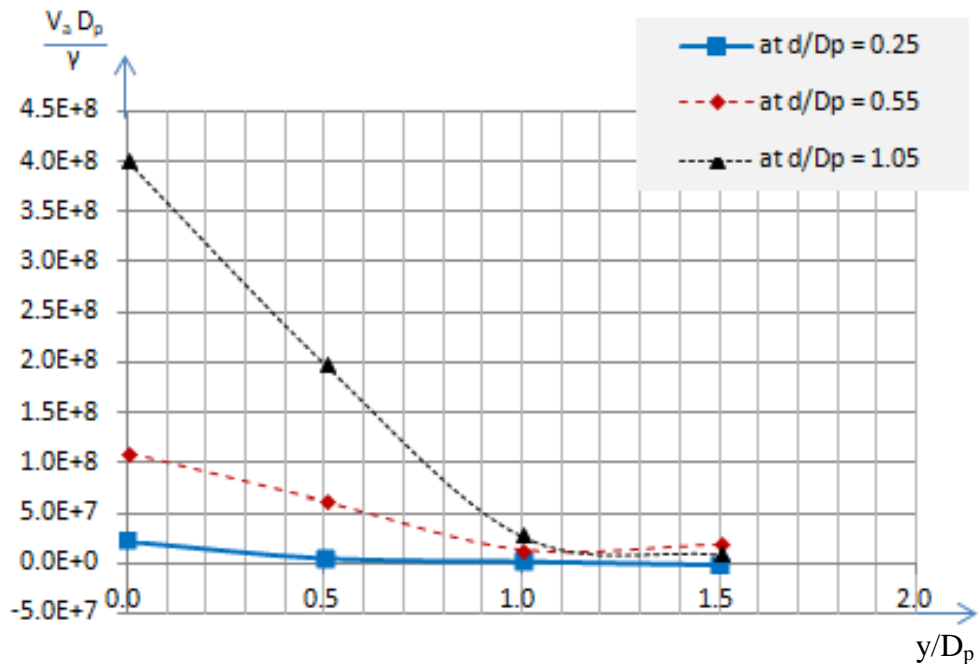


Figure 4.8b: Mean axial velocity along  $y/D_p$  at  $x/D_p = 1.5$

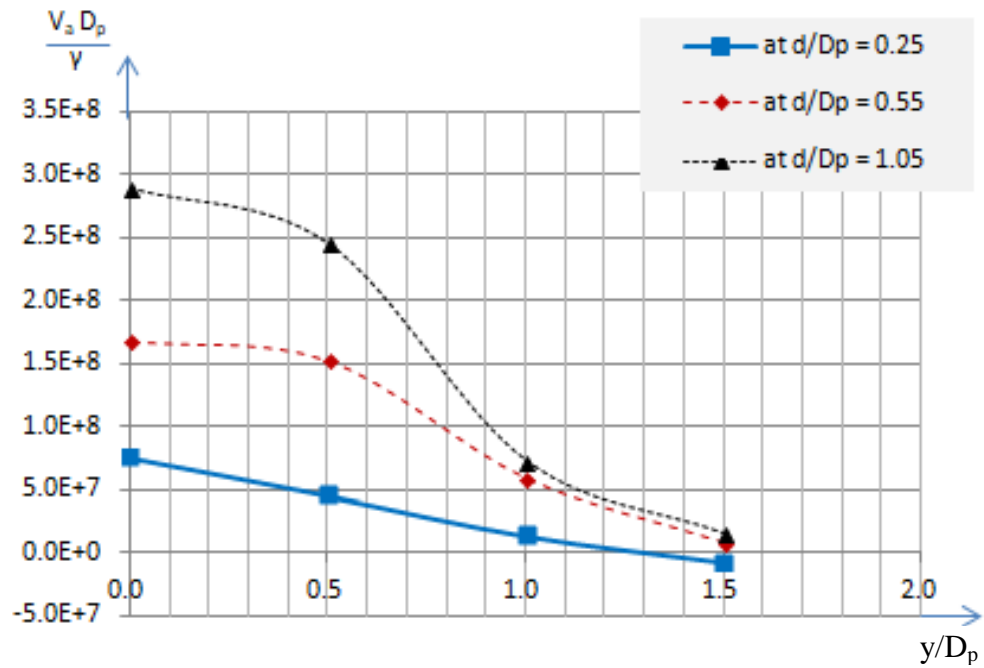


Figure 4.8c: Mean axial velocity along  $y/D_p$  at  $x/D_p = 2.5$

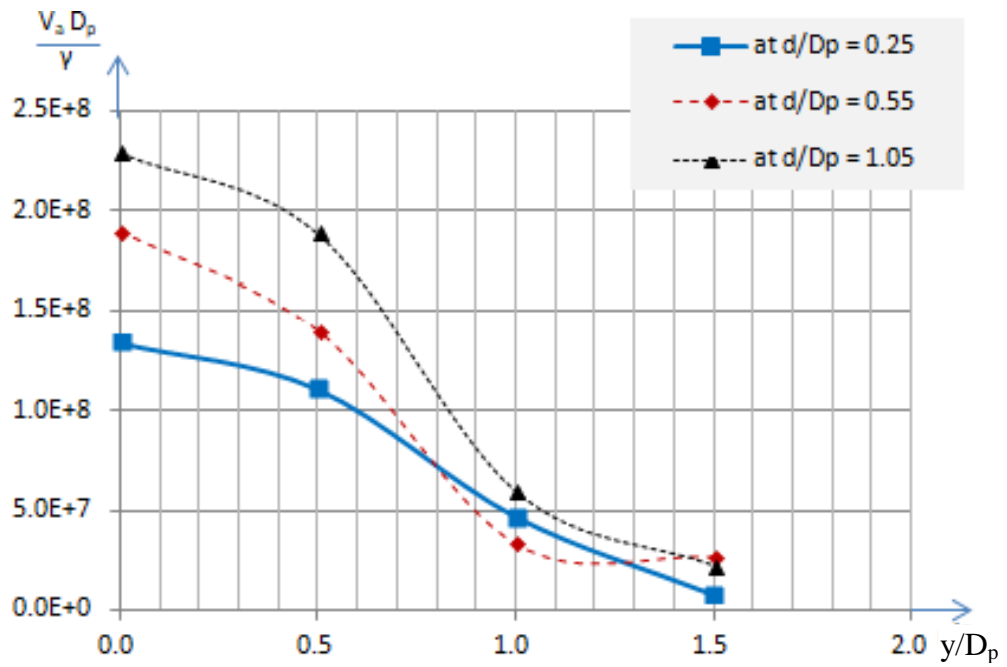


Figure 4.8d: Mean axial velocity along  $y/D_p$  at  $x/D_p = 3.5$

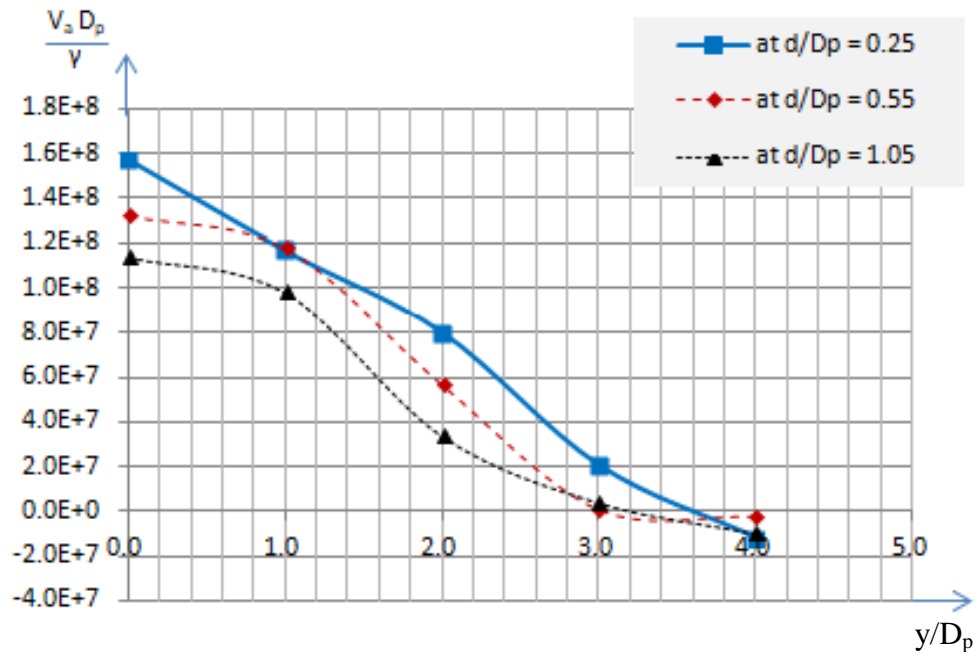


Figure 4.8e: Mean axial velocity along  $y/D_p$  at  $x/D_p = 7.5$

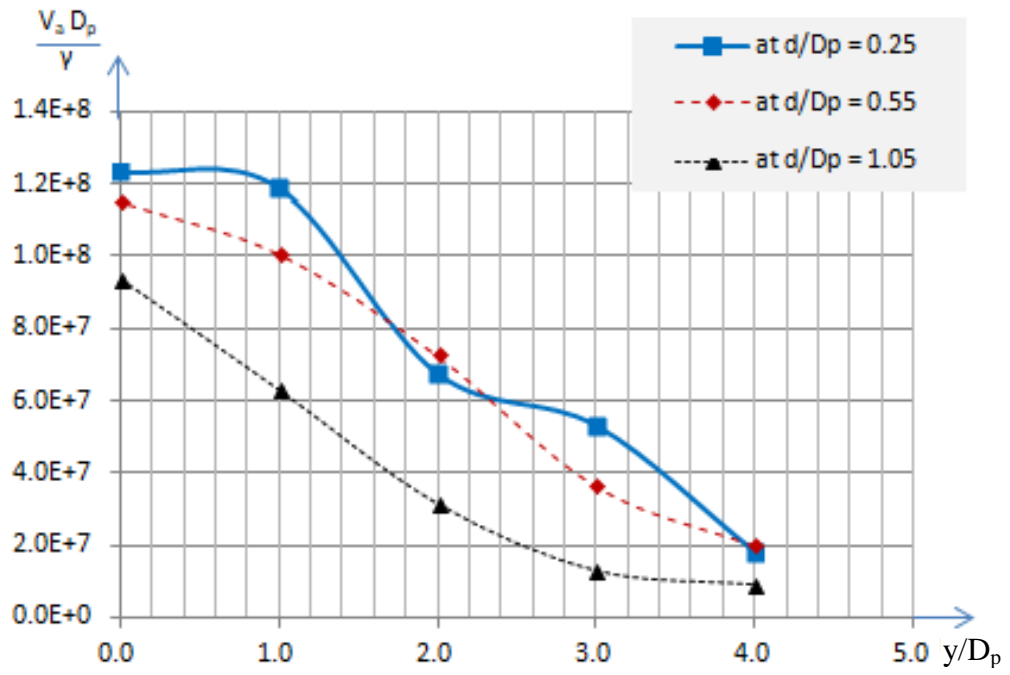


Figure 4.8f: Mean axial velocity along  $y/D_p$  at  $x/D_p = 11.5$

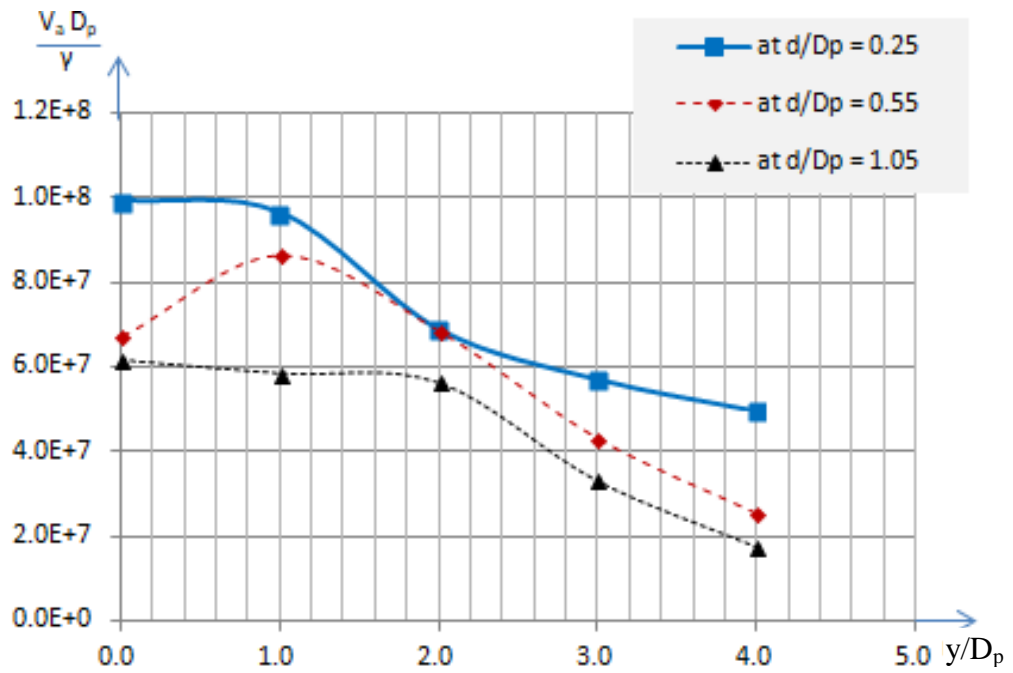


Figure 4.8g: Mean axial velocity along  $y/D_p$  at  $x/D_p = 15.5$

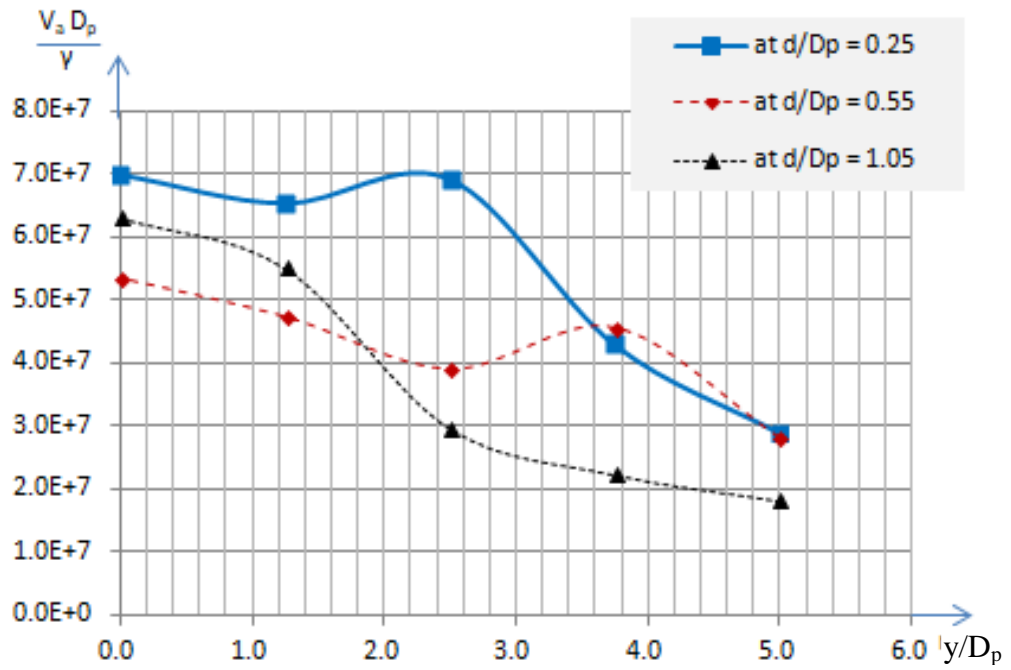


Figure 4.8h: Mean axial velocity along  $y/D_p$  at  $x/D_p = 20.5$

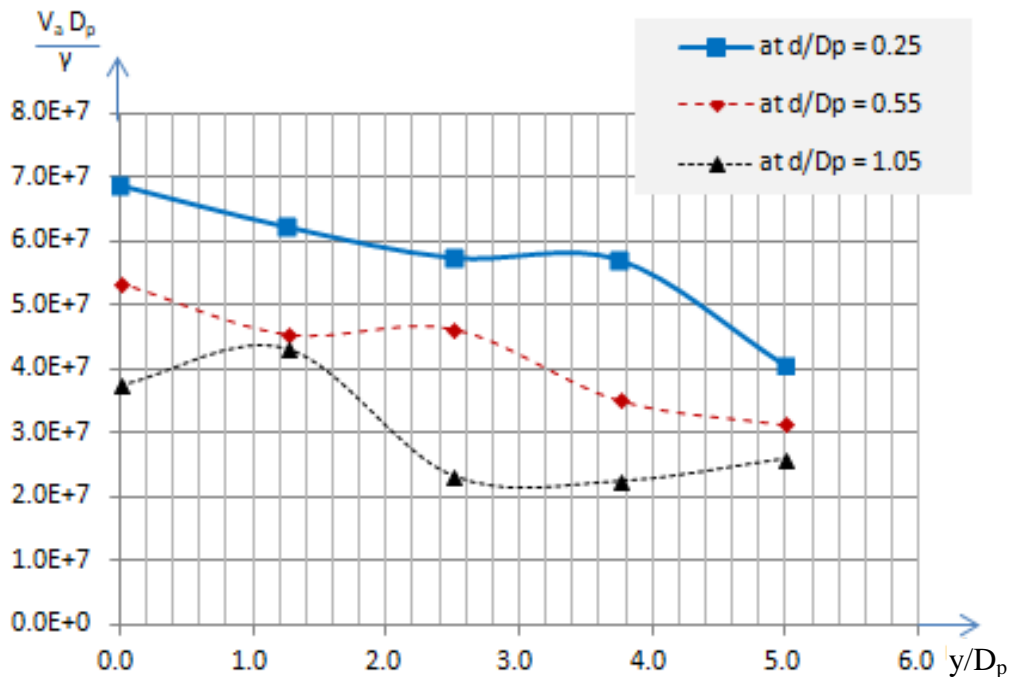


Figure 4.8i: Mean axial velocity along  $y/D_p$  at  $x/D_p = 25.5$

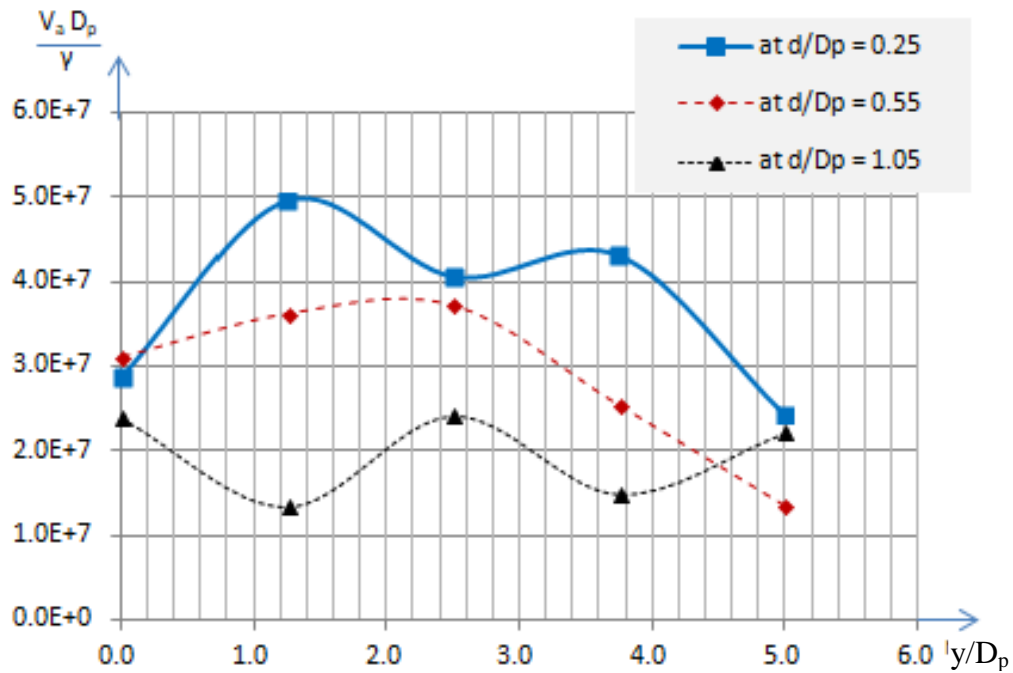


Figure 4.8j: Mean axial velocity along  $y/D_p$  at  $x/D_p = 30.5$

#### 4.3.5 The Characteristics of Mean Axial Velocity at the Depth of Measurement ( $d = 0.25D_p$ ) Closest to the Fluid Surface

One of the major purposes of conducting the experiment was to investigate the characteristics of flow at the fluid surface with respect to the variation of the major factors affecting propeller wake velocity field. But as the sensors need to be entirely submerged in fluid in order to acquire data, it was not possible to acquire data exactly at the fluid surface. Thus the measurements were done at a level just below the water surface, which was at  $d = 0.25D_p$ ; where 'd' is the vertical distance from the fluid surface. In previous sections, some plots show the change of the mean axial velocity along  $x/D_p$  for the three depths of measurements, including the depth of measurement at  $d = 0.25D_p$ . Section 4.3.1 illustrates the trend of the mean axial velocity of flow and the standard deviation along  $x/D_p$  for some cases, where the rest of the cases are shown in the test report (Amin et al., 2017). Therefore in this section the trend of

mean axial velocity along  $x/D_p$  is not discussed, rather the mean axial velocity along  $y/D_p$  is discussed.

There are three cases are studied to illustrate the characteristics of the mean axial velocity along  $y/D_p$  at different longitudinal positions ( $x/D_p =$  from 0.5 to 30.5) along the propeller wake downstream. In this section, only one case is shown and the other two cases are shown in Appendix 'D'. The three cases considered in the study show the effect of the factors on the characteristics of the mean axial velocity along  $y/D_p$  at  $d = 0.25D_p$ . Case 1 (from Figure 4.9 to Figure 4.11) shows the effect of propeller rotational speed 'n', and the experimental conditions considered are the same as considered in Section 4.3.2 (Table 4.4): experimental run #1, average of CP runs (#4, #7, #15 and #17), and run #16. The approach (OFAT) is the same described in Section 4.3.2.

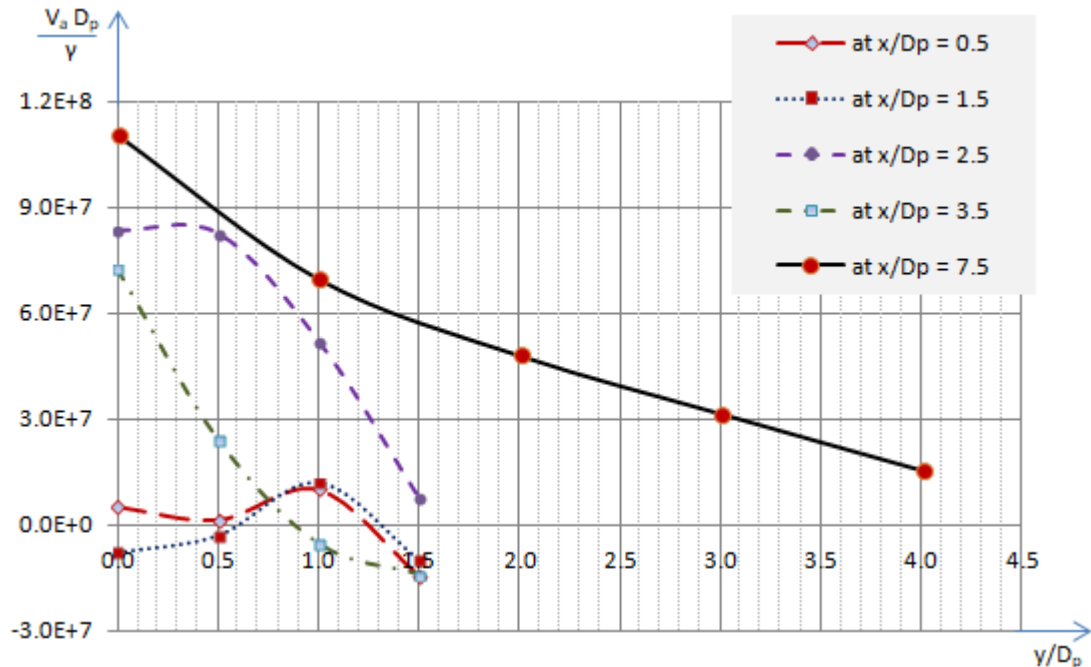


Figure 4.9a: Mean axial velocity along  $y/D_p$  at  $x/D_p = 0.50, 1.50, 2.50, 3.50$  and  $7.50$ ;

for  $n = 6$  rps,  $\theta = 4.5^\circ$  and  $H = 350$  mm

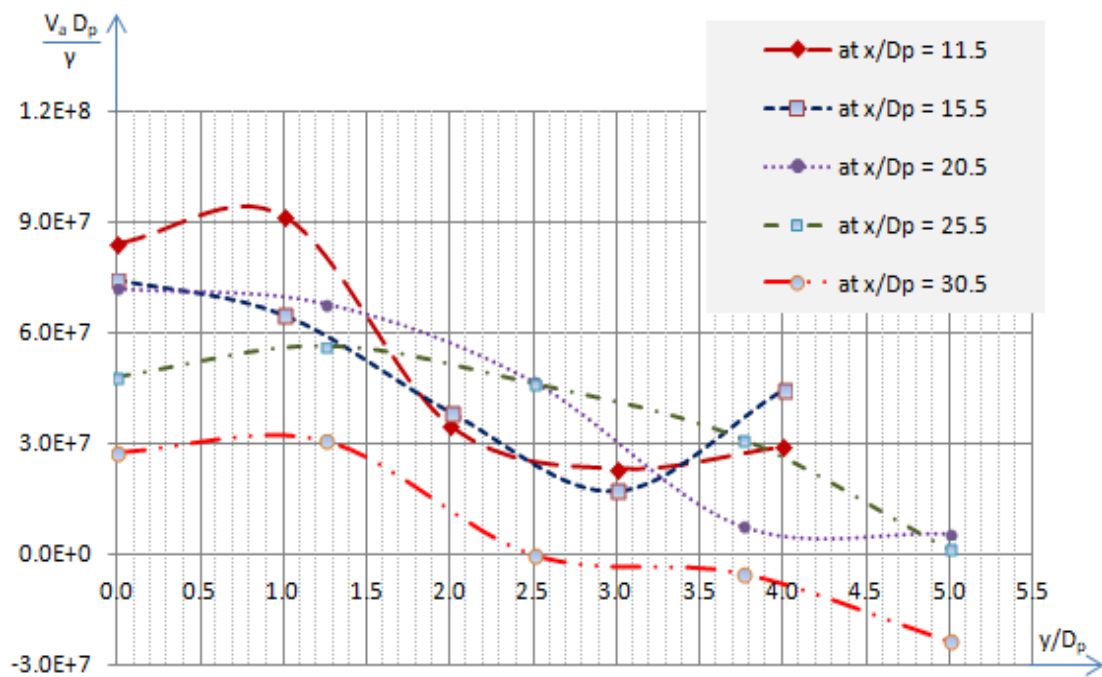


Figure 4.9b: Mean axial velocity along  $y/D_p$  at  $x/D_p = 11.50, 15.50, 20.50, 25.50$  and  $30.50$ ; for  $n = 6$  rps,  $\theta = 4.5^\circ$  and  $H = 350$  mm

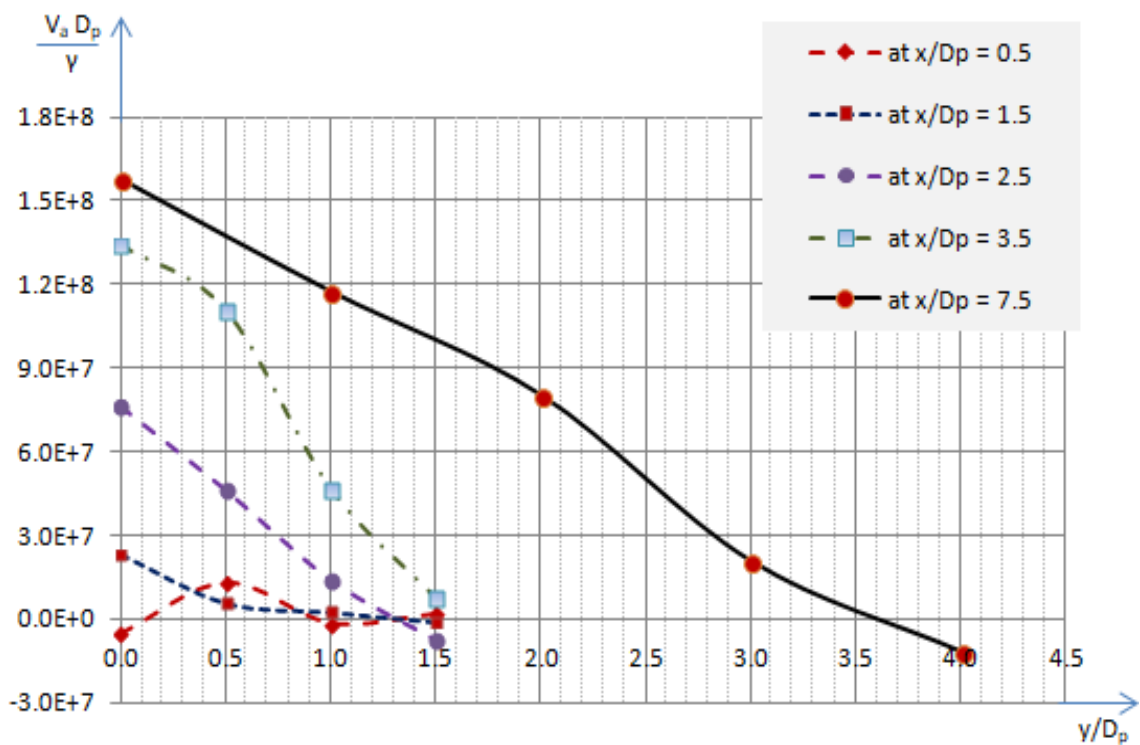


Figure 4.10a: Mean axial velocity with  $y/D_p$  at  $x/D_p = 0.50, 1.50, 2.50, 3.50$  and  $7.50$ ; for  $n = 9$  rps,  $\theta = 4.5^\circ$  and  $H = 350$  mm

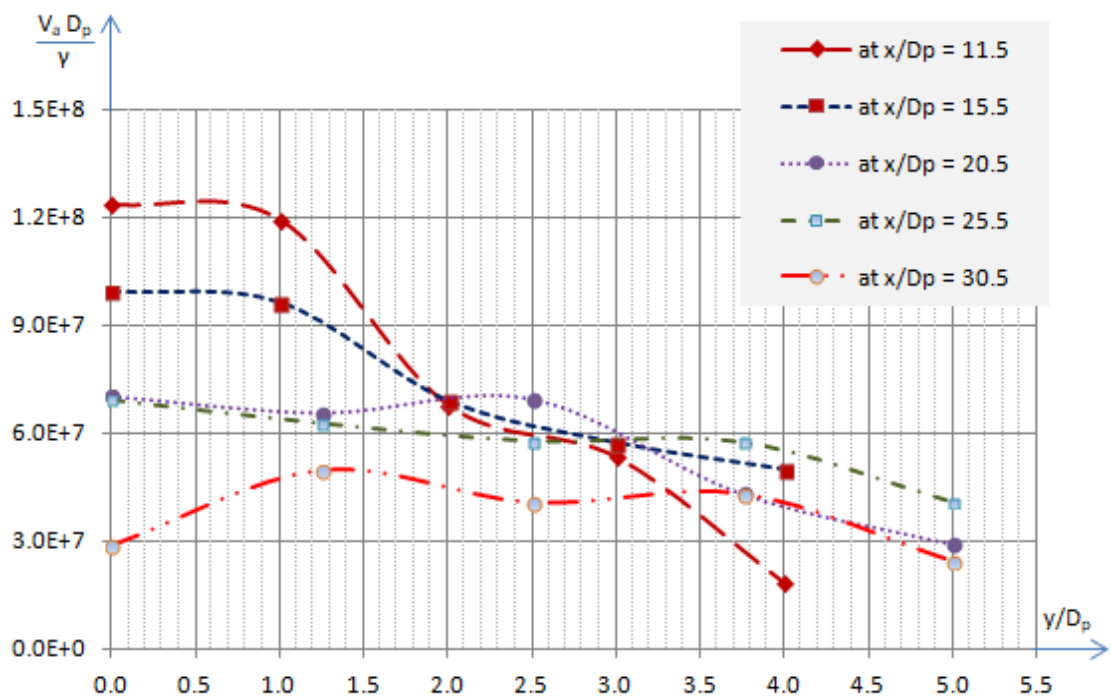


Figure 4.10b: Mean axial velocity with  $y/D_p$  at  $x/D_p = 11.5, 15.5, 20.5, 25.5$  and  $30.5$ ; for  $n = 9$  rps,  $\theta = 4.5^\circ$  and  $H = 350$  mm

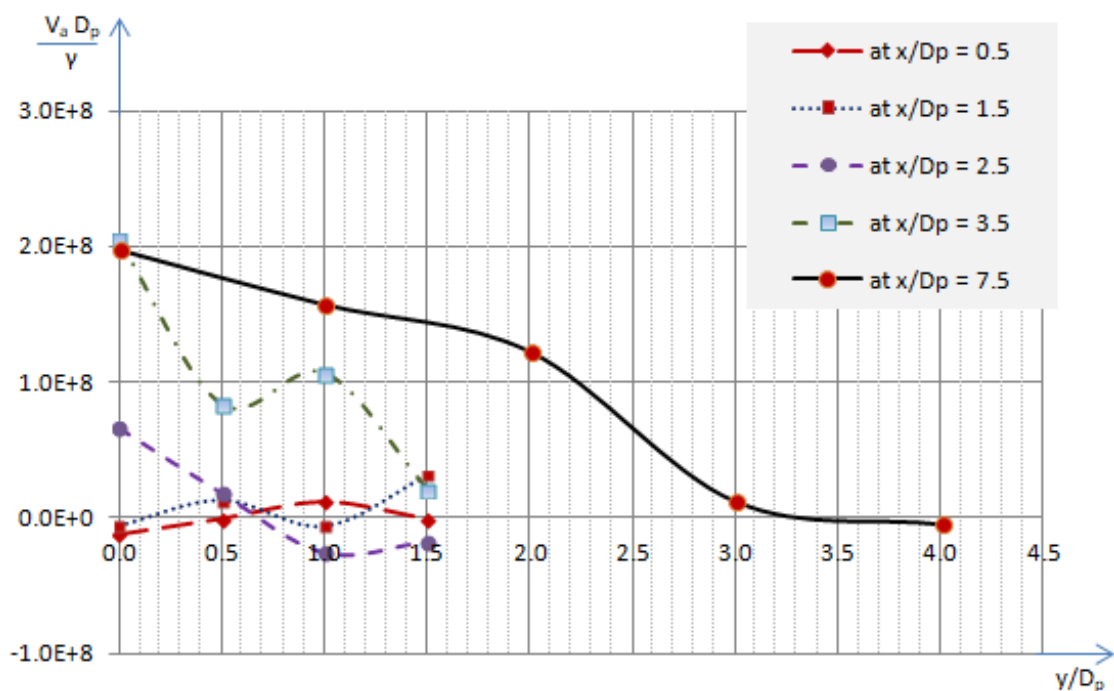


Figure 4.11a: Mean axial velocity with  $y/D_p$  at  $x/D_p = 0.5, 1.5, 2.5, 3.5$  and  $7.5$ ; for  $n = 12$  rps,  $\theta = 4.5^\circ$  and  $H = 350$  mm

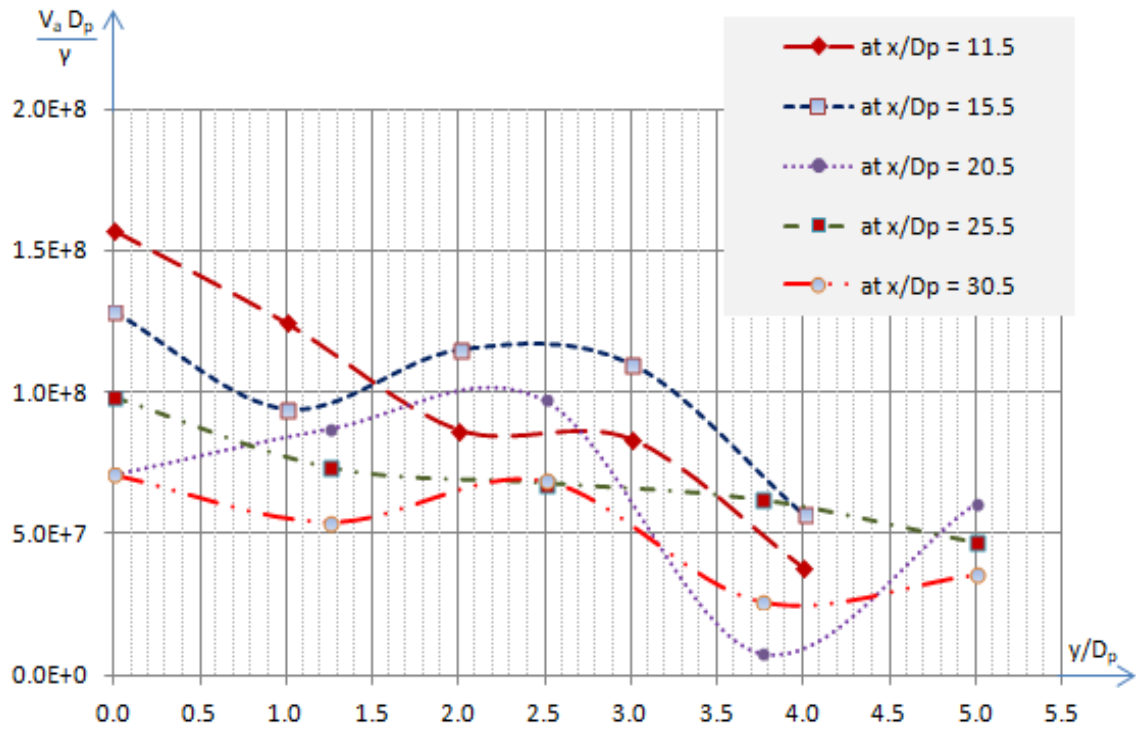


Figure 4.11b: Mean axial velocity with  $y/D_p$  at  $x/D_p = 11.50, 15.50, 20.50, 25.50$  and  $30.50$ ; for  $n = 12$  rps,  $\theta = 4.5^\circ$  and  $H = 350$  mm

It is noted from the above plots that, the maximum mean axial velocity of flow increases with the increase of propeller rotational speed. In Appendix 'D', more plots are shown to illustrate the effect of propeller inclination ' $\theta$ ' and propeller submergence ' $H$ ' on the maximum mean axial velocity of flow.

#### 4.3.6 Relationship among Factors, Location and Response Variables of Flow

This section describes the analyses of the experimental results to develop relationships among the factors, and the response variable(s) covering the entire wake field area considered in the experiment. The data analysis approach was stepwise regression, which means in the first place the relationship was developed in terms of simple linear regression equation without considering the quadratic terms. In that case, the prediction capacities ( $R^2$  values) for the most of the cases were found to be poor. After incorporating the quadratic terms, the predictions improved considerably. This means that the relationship among the experimental factors and the mean velocity (axial) of fluid at various locations along the propeller wake downstream is non-linear. All the parameters are non-dimensionalized. The functional relationship among non-dimensionalized response variable (non-dimensionalized mean axial velocity) and non-dimensionalized factors can be expressed as follows:

$$\frac{V_a D_p}{v} = f\left(\frac{n D_p^2}{v}, \theta, \frac{H}{D_p}\right)$$

The dimensional analysis technique ‘Buckingham- $\pi$  theory’ was used to develop the non-dimensionalized functional relationship among factors: propeller rotational speed ‘ $n$ ’, inclination of propeller ‘ $\theta$ ’, and depth of submergence of propeller ‘ $H$ ’, with the response variable of the study, mean axial velocity of fluid ‘ $V_a$ ’.

Assuming as follows:  $\frac{V_a D_p}{v} = V_A$ ,  $\frac{n D_p^2}{v} = X$ ,  $\theta = Y$ , and  $\frac{H}{D_p} = Z$ ; the common form of

the quadratic equation representing the relationship among the factors and the mean axial velocity can be written as given below:

$$V_A = K + aX + bY + cZ + a_1XY + b_1XZ + c_1YZ + a_2X^2 + b_2Y^2 + c_2Z^2 \quad \dots\dots (A)$$

There are ten unknown coefficients in the relationship among the factors and the response, values of which depend on the location  $\left(\frac{x}{D_p}, \frac{y}{D_p}, \frac{d}{D_p}\right)$  of measurement.

In the test report, values for coefficients for 168 locations along the propeller wake downstream are listed. In this section of the thesis, Table 4.5 and Table 4.6 only shows the list of coefficients for the prediction equations along the centre of the wake field (at  $y/D_p = 0$ ) with corresponding prediction capacity ( $R^2$ ), for 36 locations.

Table 4.5: List of coefficients K, a, b, c and  $a_1$  along the centre of the wake field

$x/D_p$	$d/D_p$	<b>K</b>	<b>a</b>	<b>b</b>	<b>c</b>	<b><math>a_1</math></b>	<b><math>R^2</math></b>
0.50	0.25	3.16E+08	9.01E+02	5.49E+06	-7.35E+08	5.49E-01	0.71
0.50	0.55	1.27E+09	1.62E+02	-6.11E+06	-1.57E+09	4.87E+01	0.95
0.50	1.05	-1.31E+09	1.31E+03	-8.12E+07	2.20E+09	7.94E+01	0.97
1.50	0.25	5.33E+08	9.86E+02	2.36E+07	-1.07E+09	3.51E+01	0.96
1.50	0.55	4.93E+08	6.00E+02	1.11E+07	-6.25E+08	-2.72E+01	0.95
1.50	1.05	-7.01E+08	5.07E+02	-1.16E+08	1.56E+09	3.94E+01	0.92
2.50	0.25	6.99E+08	-2.52E+02	2.55E+07	-7.27E+08	2.42E+01	0.95
2.50	0.55	1.94E+08	-6.19E+02	-2.58E+07	3.41E+08	9.60E+00	0.87
2.50	1.05	-7.75E+08	4.12E+02	-6.99E+07	1.35E+09	1.46E+01	0.90
3.50	0.25	2.29E+08	-2.00E+02	-1.79E+07	3.17E+07	4.18E+01	0.96
3.50	0.55	1.17E+08	-3.66E+02	-5.16E+07	4.06E+08	7.33E+01	0.97
3.50	1.05	-6.68E+08	1.16E+03	-6.75E+07	8.19E+08	2.18E+01	0.95
3.50	0.25	2.61E+07	7.94E+02	4.18E+06	-1.50E+08	1.06E+01	0.93
3.50	0.55	3.28E+08	-8.57E+02	-3.77E+07	2.45E+08	4.96E+01	0.95
3.50	1.05	-3.64E+08	2.50E+02	-4.31E+07	7.11E+08	5.03E+01	0.97
7.50	0.25	2.06E+08	-5.25E+02	-2.14E+07	1.54E+08	2.82E+01	0.89

$x/D_p$	$d/D_p$	<b>K</b>	<b>a</b>	<b>b</b>	<b>c</b>	<b>a<sub>1</sub></b>	<b>R<sup>2</sup></b>
7.50	0.55	3.46E+08	-6.63E+02	-2.08E+07	-2.68E+07	2.99E+01	0.49
7.50	1.05	1.92E+08	-3.63E+02	-3.39E+07	6.58E+07	3.51E+00	0.90
11.50	0.25	3.46E+07	2.39E+02	-1.63E+07	3.20E+07	7.25E+00	0.82
11.50	0.55	1.14E+08	-4.86E+02	5.23E+06	9.04E+07	2.05E+00	0.93
11.50	1.05	-2.27E+08	5.27E+02	-5.44E+06	2.21E+08	-1.43E+01	0.76
15.50	0.25	-1.96E+08	4.10E+02	-9.36E+06	2.41E+08	2.12E+01	0.70
15.50	0.55	1.92E+08	-4.70E+02	-1.08E+07	-3.10E+07	4.17E+00	0.86
15.50	1.05	-1.98E+07	-3.39E+02	1.92E+07	1.52E+08	-3.73E+01	0.87
15.50	0.25	8.89E+07	8.72E+00	2.22E+07	-1.32E+08	-1.17E+01	0.76
15.50	0.55	3.05E+08	-1.01E+03	-1.00E+07	3.51E+07	7.94E+00	0.81
15.50	1.05	-7.38E+07	1.66E+02	-3.62E+06	8.31E+07	-9.54E+00	0.87
20.50	0.25	5.79E+07	7.13E+01	-8.83E+06	1.90E+06	5.25E+01	0.81
20.50	0.55	9.91E+07	-4.32E+02	1.02E+07	9.13E+06	-1.72E+01	0.85
20.50	1.05	-3.46E+08	2.28E+02	2.41E+07	3.94E+08	-1.64E+01	0.77
25.50	0.25	-6.29E+07	-3.90E+01	1.63E+07	8.41E+07	-1.14E+01	0.84
25.50	0.55	-8.30E+07	2.72E+02	-1.03E+07	9.91E+07	1.53E+01	0.58
25.50	1.05	2.36E+07	1.07E+02	-8.30E+05	-3.58E+07	7.17E+00	0.73
30.50	0.25	1.12E+08	-2.02E+02	-8.55E+06	-4.00E+07	-5.49E+00	0.45
30.50	0.55	-1.79E+08	8.70E+02	-2.86E+06	-5.02E+07	-1.90E+01	0.78
30.50	1.05	-1.59E+08	4.02E-01	7.26E+06	2.09E+08	-7.15E+00	0.75

Table 4.6: List of coefficients  $b_1$ ,  $c_1$ ,  $a_2$ ,  $b_2$  and  $c_2$  along the centre of the wake field

$x/D_p$	$d/D_p$	$b_1$	$c_1$	$a_2$	$b_2$	$c_2$	$R^2$
0.50	0.25	-7.07E+01	4.91E+06	-7.32E-04	-1.30E+06	2.37E+08	0.71
0.50	0.55	-8.44E+02	-2.36E+07	9.06E-04	1.95E+06	6.31E+08	0.95
0.50	1.05	-5.26E+02	5.17E+07	-2.54E-04	-1.33E+06	-8.68E+08	0.97
1.50	0.25	-2.36E+02	-2.18E+07	-6.42E-04	-5.11E+05	3.92E+08	0.96
1.50	0.55	-4.63E+02	-3.85E+06	3.13E-04	2.28E+06	2.09E+08	0.95
1.50	1.05	-3.53E+02	9.48E+07	3.35E-04	-2.26E+06	-6.87E+08	0.92
2.50	0.25	-3.63E+02	-1.68E+07	6.68E-04	-2.56E+05	2.75E+08	0.95
2.50	0.55	-5.57E+02	2.02E+07	1.48E-03	5.10E+05	-1.19E+08	0.87
2.50	1.05	8.43E+00	5.40E+07	4.45E-05	-8.86E+05	-5.69E+08	0.90
3.50	0.25	-2.95E+02	1.49E+07	6.08E-04	-1.25E+06	-4.35E+07	0.96
3.50	0.55	-8.60E+01	1.50E+07	4.06E-04	4.83E+05	-2.09E+08	0.97
3.50	1.05	1.83E+02	4.33E+07	-9.87E-04	-5.77E+04	-3.85E+08	0.95
3.50	0.25	-4.62E+02	1.19E+07	5.44E-05	-1.63E+06	6.34E+07	0.93
3.50	0.55	-1.26E+02	2.11E+07	1.01E-03	-9.80E+05	-1.49E+08	0.95
3.50	1.05	6.24E+02	2.79E+07	-8.17E-04	-2.61E+06	-4.14E+08	0.97
7.50	0.25	-1.49E+00	1.38E+07	6.04E-04	-1.02E+06	-1.05E+08	0.89
7.50	0.55	3.90E+02	7.15E+06	1.43E-04	-1.81E+05	-8.95E+07	0.49
7.50	1.05	4.25E+02	1.46E+07	-6.61E-05	8.28E+05	-1.26E+08	0.90
11.50	0.25	2.39E+01	9.19E+06	-6.84E-05	9.01E+04	-4.72E+07	0.82
11.50	0.55	1.87E+02	6.41E+06	3.85E-04	-1.39E+06	-8.26E+07	0.93
11.50	1.05	-7.40E+00	6.31E+06	-2.45E-04	7.21E+04	-9.16E+07	0.76
15.50	0.25	-1.35E+02	5.84E+06	-1.83E-04	-6.10E+05	-7.26E+07	0.70
15.50	0.55	5.35E+00	1.01E+07	5.30E-04	-2.73E+05	-4.17E+06	0.86
$x/D_p$	$d/D_p$	$b_1$	$c_1$	$a_2$	$b_2$	$c_2$	$R^2$

15.50	1.05	1.04E+02	-2.16E+06	-1.24E-04	1.01E+06	-4.36E+07	0.87
15.50	0.25	6.56E+01	-3.10E+06	-3.53E-04	-1.19E+06	-8.39E+06	0.76
15.50	0.55	3.96E+01	1.48E+06	5.52E-04	-2.16E+05	-1.46E+07	0.81
15.50	1.05	-9.00E+01	-6.54E+06	3.61E-05	-8.43E+05	-1.12E+08	0.87
20.50	0.25	1.14E+02	4.37E+06	4.70E-05	-1.60E+06	-5.49E+07	0.81
20.50	0.55	1.66E+01	8.84E+06	-3.21E-04	-8.41E+05	-5.02E+07	0.85
20.50	1.05	7.30E+01	2.15E+06	-1.76E-04	-7.74E+05	-5.00E+06	0.77
25.50	0.25	4.50E+01	8.75E+06	1.75E-04	-1.24E+05	-8.59E+05	0.84
25.50	0.55	9.47E+01	9.85E+06	-8.02E-04	-9.20E+04	-1.48E+07	0.58
25.50	1.05	-4.60E+01	-2.41E+06	1.39E-04	-1.37E+04	-5.88E+07	0.73
30.50	0.25	1.04E+02	-2.16E+06	-1.24E-04	1.01E+06	-4.36E+07	0.45
30.50	0.55	6.56E+01	-3.10E+06	-3.53E-04	-1.19E+06	-8.39E+06	0.78
30.50	1.05	3.96E+01	1.48E+06	5.52E-04	-2.16E+05	-1.46E+07	0.75

By using the values of coefficients that are presented in Table 4.5 and Table 4.6, the regression equations illustrating the relationships among factors and response along the centre of the wake at three different depths ( $d/D_p = 0.25, 0.55$  and  $1.05$ ) and at different longitudinal locations can be determined. The average prediction capacity of these equations for locations along the centre of the wake is 84%. The average prediction capacity of all the regression equations for 168 locations throughout the wake is 71%. The average value of coefficients should be taken for locations that coincide. Design Expert 9.0 statistical analysis software was used to do the regression analysis of the experimental data by following the response surface composite design (CCD) method, as described in earlier sections.

Further analysis was done to minimize the total number of equations, through developing relationship among the ten coefficients ( $K$ ,  $a$ ,  $b$ ,  $c$ ,  $a_1$ ,  $b_1$ ,  $c_1$ ,  $a_2$ ,  $b_2$ ,  $c_2$ ) and the three parameters for defining locations ( $x/D_p$ ,  $d/D_p$  and  $y/D_p$ ). ‘Fit Regression Model’ tool of Minitab 18.0 software was used for the statistical analysis. The objective of the analysis was to express each coefficient in terms of the three parameters that define the location of measurement under three zones (near field, intermediate field, and far field). In that case, there should be 30 ( $10 \times 3$ ) equations replacing 168 equations, where each equation will express the relationship among response, factors, and parameters that define the location of measurement. The regression analysis approach considered was ‘stepwise’, where the software automatically carries out the analysis progressively by incorporating lower to higher order terms that may significantly affect the response variable. The program was given the instruction to do analysis up to cubic polynomial terms in order to obtain regression equations having good prediction capacities, but the prediction capacities of the equations for most of the cases were found to be unacceptable. Therefore, the results of the analysis are not incorporated in the thesis. In order to predict the response variable at a particular location, the corresponding values of the coefficients should be used directly for the best results.

The results that can be obtained from the prediction models are validated for a particular experimental configuration: propeller rotational speed of 9 rps, propeller inclination angle of  $4.5^\circ$ , and depth of propeller submergence of 350 mm. Table 4.7 shows the validation of regression equations only along the centre of the wake field (at  $y/D_p = 0$ ) for the experimental configuration.

Table 4.7: Validation of prediction equations at the centre of the wake field

Location #	$x/D_p$	$d/D_p$	Results from Prediction Model	Experimental Results	Difference %
1	0.50	0.25	2.41E+06	-5.13E+06	147
2	0.50	0.55	5.57E+06	1.64E+07	66
3	0.50	1.05	4.41E+08	4.44E+08	1
4	1.50	0.25	2.09E+07	2.28E+07	8
5	1.50	0.55	1.02E+08	1.09E+08	7
6	1.50	1.05	3.86E+08	4.01E+08	4
7	2.50	0.25	6.90E+07	7.59E+07	9
8	2.50	0.55	1.65E+08	1.69E+08	2
9	2.50	1.05	2.90E+08	2.89E+08	0
10	3.50	0.25	1.30E+08	1.34E+08	3
11	3.50	0.55	1.88E+08	1.89E+08	1
12	3.50	1.05	2.32E+08	2.29E+08	-1
13	3.50	0.25	1.28E+08	1.34E+08	5
14	3.50	0.55	1.88E+08	1.92E+08	2
15	3.50	1.05	2.50E+08	2.50E+08	0
16	7.50	0.25	1.51E+08	1.57E+08	4
17	7.50	0.55	1.36E+08	1.32E+08	-3
18	7.50	1.05	1.11E+08	1.14E+08	2
19	11.50	0.25	1.23E+08	1.24E+08	0
20	11.50	0.55	1.15E+08	1.15E+08	0
21	11.50	1.05	9.58E+07	9.37E+07	-2
22	15.50	0.25	1.02E+08	9.94E+07	-2

Location #	$x/D_p$	$d/D_p$	Results from Prediction Model	Experimental Results	Difference %
23	15.50	0.55	6.86E+07	6.70E+07	-2
24	15.50	1.05	6.14E+07	6.17E+07	1
25	15.50	0.25	1.02E+08	1.01E+08	-2
26	15.50	0.55	6.34E+07	6.21E+07	-2
27	15.50	1.05	5.92E+07	6.13E+07	3
28	20.50	0.25	7.38E+07	7.01E+07	-5
29	20.50	0.55	5.33E+07	5.36E+07	0
30	20.50	1.05	6.35E+07	6.31E+07	-1
31	25.50	0.25	6.97E+07	6.90E+07	-1
32	25.50	0.55	5.28E+07	5.34E+07	1
33	25.50	1.05	3.78E+07	3.75E+07	-1
34	30.50	0.25	3.26E+07	2.86E+07	-14
35	30.50	0.55	3.11E+07	3.10E+07	0
36	30.50	1.05	2.54E+07	2.39E+07	-6

In the above table, the differences for locations #1 and #2 are unacceptably large and thus the fit is found to be poor in those locations. For most of the remaining cases, the results from the prediction model are close to experimental results.

The two factorial interaction effects (2FI) regarding the three experimental factors are considered within the analysis by incorporating the multiplication terms XY, XZ and YZ in equation (A). As the statistical analysis was done for each location, it is possible to generate 3D surface plot for each location to explain the interaction effect of factors. As an example, Figure 4.12 shows the change in response variable (fluid velocity) in terms of the variation of propeller rotational speed and propeller

inclination, for the location (location #9 in Table 4.7) at  $x/D_p = 2.50$ ,  $d/D_p = 1.05$ , and  $y/D_p = 0.0$ . Similarly, interaction effects at any location can be explained by developing the related 3D surface plot for that location. Section 5 explains the results that are described in this section.

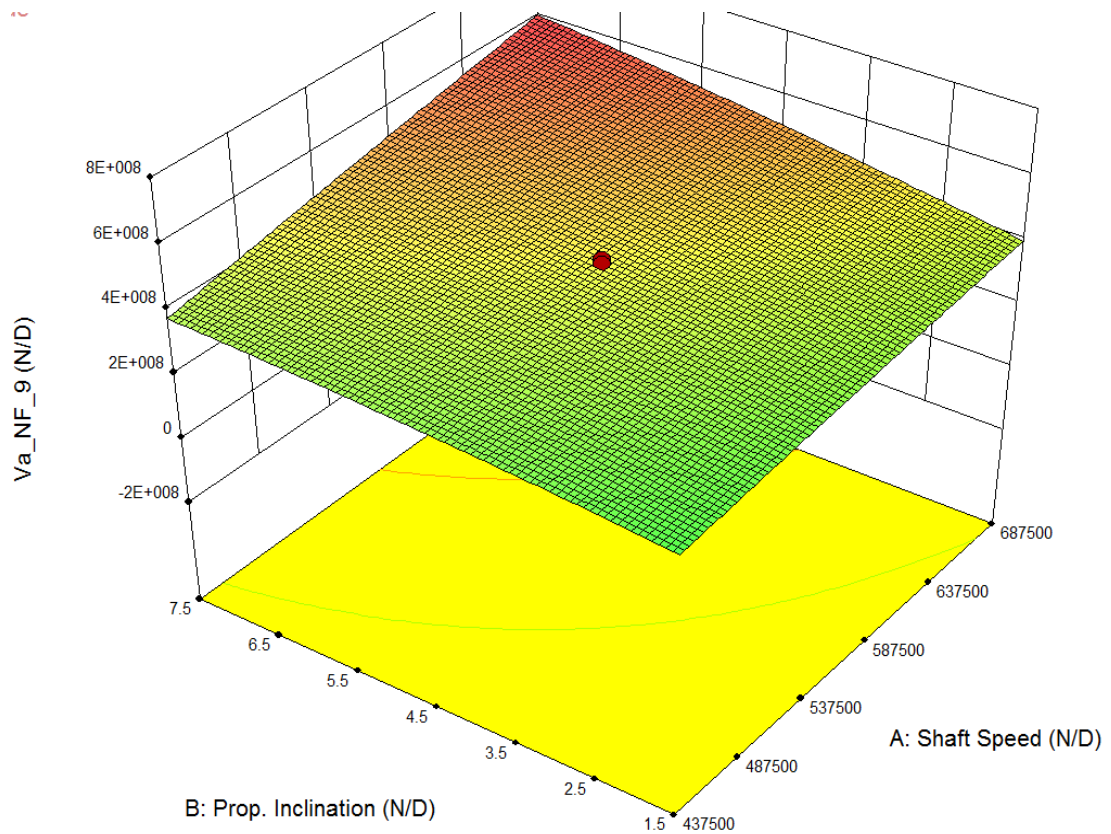


Figure 4.12: 3D surface plot at location #9 ( $x/D_p = 2.50$ ,  $d/D_p = 1.05$ , and  $y/D_p = 0.0$ ), showing the change of non-dimensional mean axial velocity with non-dimensional shaft rotational speed and propeller inclination

As the variability  $\left(\frac{\sigma_{D_P}}{v}\right)$  of flow for each location was also recorded, the relationship among factors and variability can also be developed in the same way.

#### 4.3.7 Characteristics of the Mean Axial Velocity of Flow along $d/D_p$ and near the Fluid Surface

The characteristics of the response surface within the flow depend on the configuration of factors and the position of propeller. The variations of these factors affect the response variable in different ways along the propeller wake downstream. For the same shaft rotational speed, if the propeller inclination is increased, then the component of jet velocity directed towards the fluid surface will increase, resulting in an increase in the overall fluid velocity near the surface. The distribution of fluid velocity along the wake may be different, even resulting in a reduction of velocity along the wake field. In this section, Figure 4.13 to Figure 4.15 show the trend of the non-dimensionalized fluid axial velocity with  $x/D_p$  along the centre of the wake ( $y/D_p = 0.0$ ) at 3 different depths, and for 3 different propeller conditions.

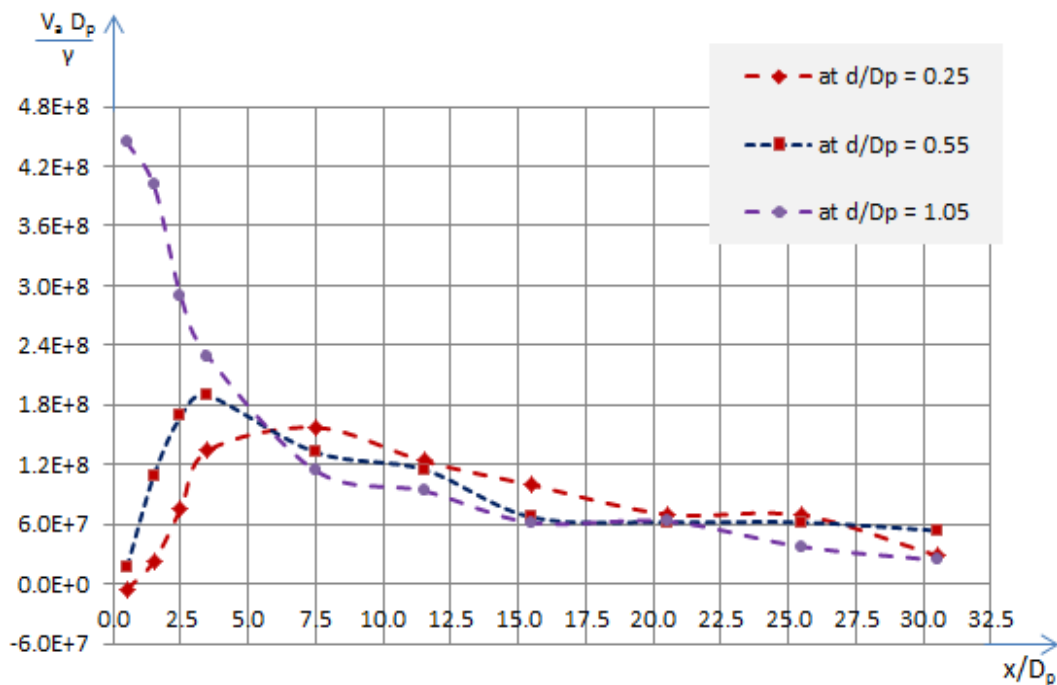


Figure 4.13: Mean axial velocity along  $x/D_p$  at  $y/D_p = 0.0$  for 3 depths, for propeller condition:  $n = 9$  rps,  $\theta = 4.5^\circ$ , and  $H = 350$  mm

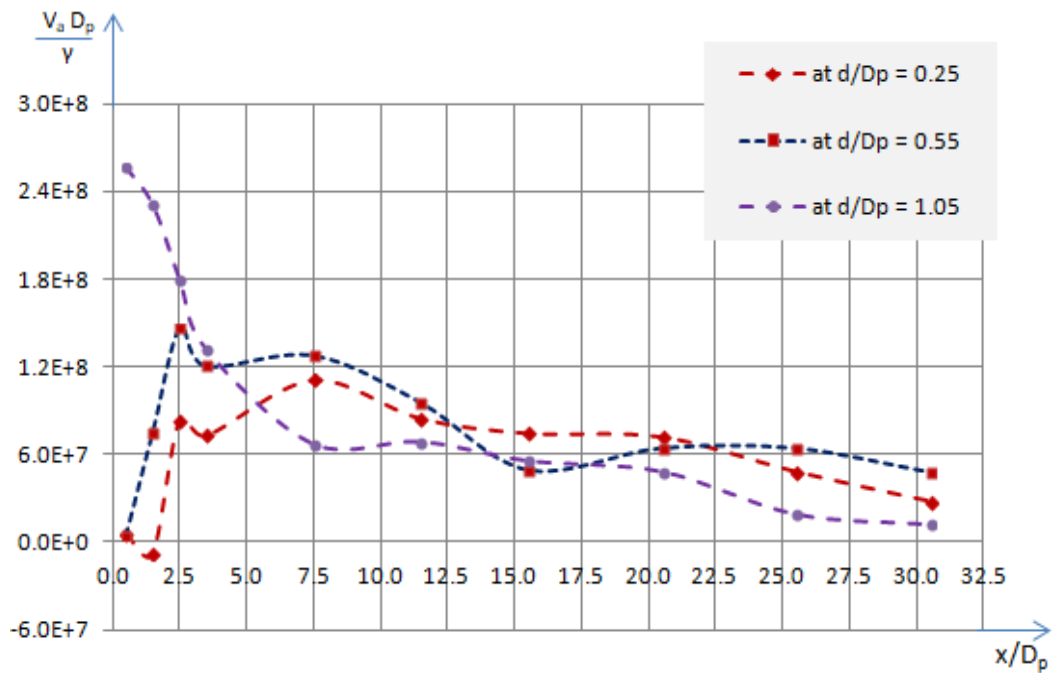


Figure 4.14: Mean axial velocity along  $x/D_p$  at  $y/D_p = 0.0$  for 3 depths, at propeller condition:  $n = 6$  rps,  $\theta = 4.5^\circ$ , and  $H = 350$  mm

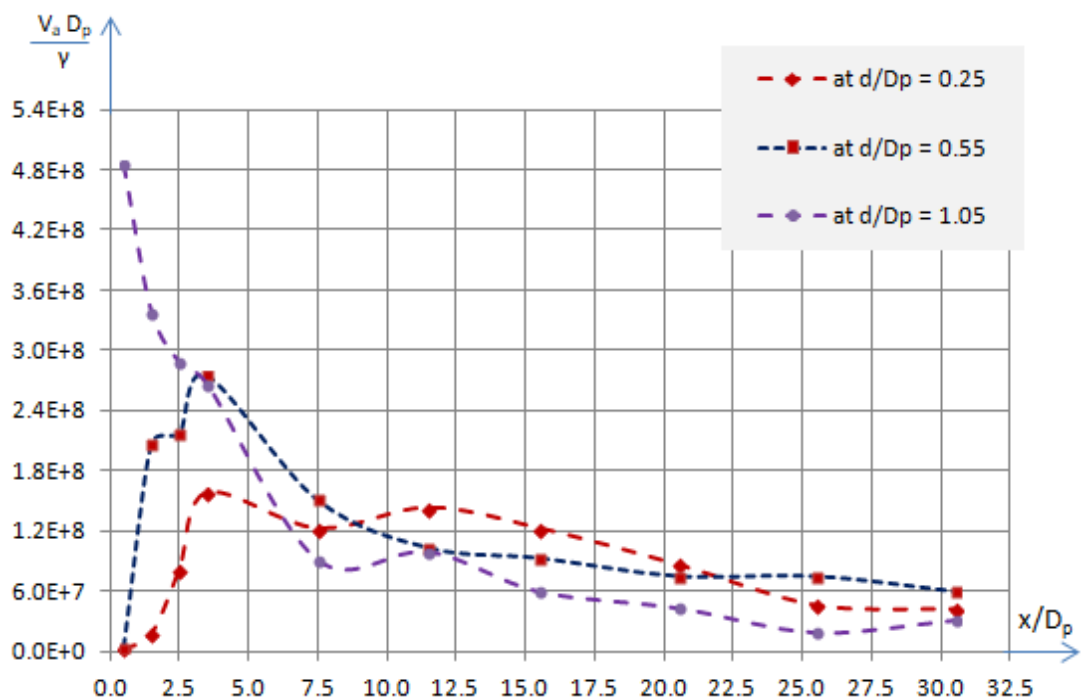


Figure 4.15: Mean axial velocity along  $x/D_p$  at  $y/D_p = 0.0$  for 3 depths, at propeller condition:  $n = 9$  rps,  $\theta = 9^\circ$ , and  $H = 350$  mm

To illustrate the interaction effect of  $x/D_p$  and  $d/D_p$  on axial velocity, a 3D surface plot for a particular propeller condition ( $n = 9$  rps,  $\theta = 4.5^\circ$ , and  $H = 350$  mm) was developed. Figure 4.16 shows the mean axial velocity in terms of  $x/D_p$  and  $d/D_p$  at the centre of the wake (at  $y/D_p = 0.0$ ). From the surface plot it is noted that until  $x/D_p \approx 6.0$ , the fluid velocity increases with  $d/D_p$ , and with the increase of  $x/D_p$ , the increase rate of axial velocity with  $d/D_p$  decreases drastically. The prediction equations for  $d/D_p = 0.25$  can be used to approximately predict the response variable at  $d/D_p \approx 0.0$  (at fluid surface) in terms of the three factors considered in the study.

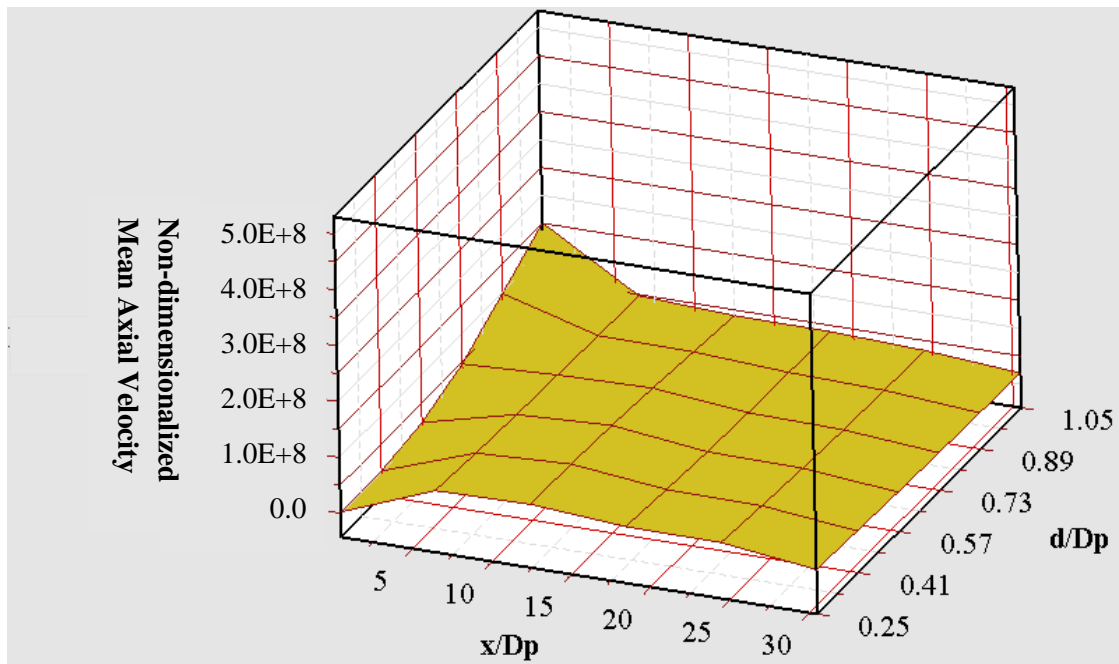


Figure 4.16: A Minitab plot showing the trend of the mean axial velocity against  $x/D_p$  and  $d/D_p$  at  $y/D_p = 0.0$ , for propeller condition:  $n = 9$  rps,  $\theta = 4.5^\circ$ , and  $H = 350$  mm

## CHAPTER 5 - DISCUSSION OF RESULTS

The objective of the experiment was to develop models to predict the mean velocities of fluid, as well as the corresponding variabilities along the propeller wake downstream in terms of the most significant factors affecting propeller wake wash. As the propeller and flow Reynolds numbers for the lowest rotational speed (6 rps) considered in the experiment are higher than the limiting Reynolds number, it is expected that the prediction models can be used for full scale assessments. Also the parameters used in the prediction equations are non-dimensionalized, which means the equations are independent of the units of the parameters. The maximum mean axial velocities for the five rotational speeds considered in the experiment were measured, and compared with the calculated efflux velocities for the corresponding rotational speeds. The difference between the measured mean axial velocity and the calculated efflux velocity for each propeller rotational speed was found to be insignificant.

The results are analyzed only for the axial component of fluid velocity in a propeller wake field. In the thesis, the analyses are done from various aspects to characterize the axial fluid velocity throughout the effective area of the propeller wake field, in terms of the variation of the factors considered in the present study.

The standard deviation was recorded for each measurement in order to capture the variability in the flow. Section 4.3.1 of the thesis, and Section 4.1 of the test report (Amin et al., 2017) present the plots for the mean axial velocities and the corresponding standard deviations along  $x/D_p$  of the wake field for all the propeller conditions considered in the experiment. The trends of the mean axial velocities and the standard deviations along  $x/D_p$  are found to be reasonable for all cases.

One of the major purposes of the experiment was to investigate the individual effect of the factors on the propeller wake velocity field. For this purpose, an approach known as OFAT is applied to develop some plots to evaluate how significantly each of the three factors affects the propeller wake field, as described in Section 4.3.2 of the thesis. It is noted from Figure 4.4a to Figure 4.6a that, along the centre of the wake field (at  $y = 0.0$ ) as the propeller rotational speed increases, the axial velocities along  $x/D_p$  also increase for all three depths of measurements, keeping other two factors unchanged. Also, the plots illustrate the trend of the mean axial velocities along  $x/D_p$  with the variation of propeller rotational speed. At the deeper level ( $d/D_p = 1.05$ ), the trend is different from the trend at shallow depth. Figure 4.4b to Figure 4.6b illustrate the effect of propeller inclination on the mean axial velocity. With the increase of propeller inclination, the mean axial velocities at different longitudinal locations of the wake field also increase. But at deeper level ( $d/D_p = 1.05$ ), the effect of propeller inclination diminishes. With respect to propeller submergence, the lower the propeller submergence, the higher was the mean axial velocity at the shallowest depth. At deeper level ( $d/D_p = 1.05$ ), the effect of propeller submergence is inconsistent. From Figure 4.4c to Figure 4.6c illustrate the effect of propeller submergence on the mean axial velocity along the propeller wake.

On the basis of all the plots that illustrate the individual effect of factors on the mean axial velocity, it can be concluded that the mean axial velocity is proportional to the propeller rotational speed and the propeller inclination, where the mean velocity is inversely proportional to the depth of submergence, for a particular propeller condition. Also the effect of factors is less pronounced at deeper levels within the wake field. From the plots it can also be concluded that the propeller rotational speed

and the propeller inclination are more influential than the propeller submergence. In Section 4.3.6 of the thesis and in Section 4.2 of the test report (Amin et al., 2017), some 3D surface plots are shown to explain the 2 factorial interaction effect of factors on the mean axial velocity, and to illustrate the most influential factor. From these plots it is found that the rate of change of the mean axial velocity is higher due to propeller rotational speed, than the rate of change due to propeller inclination. Propeller rotational speed is the most influential factor affecting the mean axial velocity positively, which is in agreement with the findings of the earlier research (Ferrieri et al., 2013; Bastin, 2014).

The experimental results are compared with the results derived from the mathematical model of Bastin (2014) for 3 propeller conditions, or configurations of factors that were used in the experiment, along the centre of the wake field. The experimental mean axial velocities are found on the higher side, comparing to those obtained from the mathematical model, as shown by the plots presented in Section 4.3.3 and in Appendix 'C'.

The characteristics of the mean axial velocities along transverse locations (along  $y/D_p$ ) were investigated for 1 propeller condition. It is expected that the pattern of the trend of the mean axial velocity will be the same for other propeller conditions. In Section 4.3.4 of the thesis, the plots illustrate the trend of the mean axial velocities along  $y/D_p$  at different longitudinal locations of the wake field. In the near field region ( $x/D_p \leq 3.50$ ), the distribution of the mean axial velocities along  $y/D_p$  for 3 different depths of measurements ( $d/D_p = 0.25, 0.55$  and  $1.05$ ) at different longitudinal locations indicate that, the mean axial velocities along  $y/D_p$  increase with  $x/D_p$  for all 3 depths of measurements. At  $x/D_p = 7.50$ , all the curves for the 3 depths show higher mean axial

velocities along  $y/D_p$  than that at any other longitudinal locations ( $x/D_p$ ) of the wake field. This indicates that the most effective region of the wake field is at  $x/D_p \approx 7.50$  for the selected propeller condition ( $n = 9.0$  rps,  $\theta = 4.5^\circ$ , and  $H = 350$  mm). It is expected that, as ' $\theta$ ' increases the most effective region of the wake field will be closer to the propeller, and vice versa. From the plots (from Figure 4.8a to Figure 4.8j), it is also noted that the curves become flatter within  $x/D_p = 25.50$  and  $x/D_p = 30.50$ , which indicates that the size of the effective wake field is located in between  $x/D_p = 25.50$  and  $x/D_p = 30.50$ , for the propeller condition selected to study.

One of the major interests of the experiment was to investigate the change in the characteristics of the mean axial velocity along the wake field at the fluid surface in terms of the major factors affecting the propeller wake field, which was not possible to do, as described in Section 4.3.5. In Section 4.3.5 and Appendix 'D' of the thesis, a study on the trend of the mean axial velocity at the depth of measurement closest to the fluid surface (at  $d/D_p = 0.25$ ) is described considering the individual effect of factors. The assessment is similar to what is done in Section 4.3.2. From the plots (from Figure 4.9a to Figure 4.11b), it is noted that as ' $n$ ' increases, the mean axial velocities throughout the wake field also increase. The mean axial velocities along  $y/D_p$  increase with the increase of  $x/D_p$  up to a certain extent (mostly until  $x/D_p \approx 7.50$ ), and then the mean velocities along transverse locations gradually decrease with the increase of  $x/D_p$ . This is applicable for all 3 propeller rotational speeds considered for the study. From these plots, the length of the effective wake field can also be determined, in the same way as described earlier for Section 4.3.4, as well as the most effective zone (the zone where the mean axial velocities are higher than others) in the wake field. Figure D1 to Figure D4 illustrate the effect of propeller inclination ' $\theta$ ' on

the mean axial velocity, and it is noted that as ' $\theta$ ' increases, the overall mean axial velocities in the wake field also increase. Figure D5 to Figure D8 illustrate the effect of propeller submergence ' $H$ ' on the mean axial velocity, and it is noted that ' $H$ ' has a reverse effect in increasing the mean axial velocities along the downstream of propeller wake field.

Section 4.3.6 of this thesis, and Section 4.3 of the test report (Amin et al., 2017) contain all the prediction models that are developed through the study, which show the relationships among the response variable and the factors considered in the study. The statistical analysis was done by using Design Expert 9.0 software to generate the regression equations (prediction models), which include up to quadratic terms to achieve a good prediction capacity. There are 9 locations which coincide, and for those locations the equation having higher prediction capacity should be used. The equations along the centre of the wake field ( $y = 0.0$ ) are checked for a particular condition ( $n = 9.0$  rps,  $\theta = 4.5^\circ$ , and  $H = 350$  mm). A 3D surface plot is shown in Section 4.3.6, and more plots are shown in Section 4.2 of the test report (Amin et al., 2017). From these plots it is noted that propeller rotational speed ' $n$ ' is more influential than propeller inclination ' $\theta$ ' to affect the mean axial velocity of flow in a propeller wake field, particularly in the intermediate field ( $3.5 \leq x/D_p \leq 15.5$ ) and near field ( $x/D_p \leq 3.50$ ) zones. In the near field zone ( $x/D_p \leq 3.50$ ), the effects of ' $n$ ' and ' $\theta$ ' on the mean velocity are almost the same, and the mean axial velocity increases with the increase of ' $n$ ' and ' $\theta$ '. As  $x/D_p$  increases, the effect of ' $n$ ' increases over ' $\theta$ '. In the far field zone ( $x/D_p \leq 15.50$ ), the mean axial velocity increases with ' $\theta$ ' up to a certain extent, and then the mean axial velocity decreases gradually with the increase of ' $\theta$ '.

Section 4.3.7 of the thesis presents the analysis to characterize the trend of the mean axial velocity near the water surface along  $x/D_p$ , through developing some relationship among the mean axial velocity,  $x/D_p$ , and  $d/D_p$ . For this purpose, initially 3 propeller conditions are considered to study the pattern of the change of the mean axial velocity with  $d/D_p$  along  $x/D_p$ . From Figure 4.13 to Figure 4.15, it is noted that in the near field zone ( $x/D_p \leq 3.5$ ) for shallow depths (at  $d/D_p = 0.25$  and  $0.55$ ) the mean axial velocity increases with  $x/D_p$ . At  $d/D_p = 1.05$ , the phenomena are reversed. Also for  $d/D_p = 1.05$ , the decay rate of the mean axial velocity (along  $x/D_p$ ) is the highest in the near field zone ( $0.0 \leq x/D_p \leq 3.5$ ), then the decay rate decreases within about  $3.5 \leq x/D_p \leq 7.5$ , and after about  $x/D_p = 7.5$  there is a decreasing trend of axial velocity having fluctuation within a small range, for all propeller conditions. For shallow depths (at  $d/D_p = 0.25$  and  $0.55$ ), the increase rates of axial velocities within near field are high reaching to almost their peaks, followed by gradual decay of axial velocity with  $x/D_p$ , and then it fluctuates within a small range. Moreover, the propeller submergence 'H' for all 3 conditions was the same (350 mm), and if 'H' reduces then the velocity at shallow depth, and at the fluid surface will increase, as studied in Section 4.3.5.

In Figure 4.16, a 3D surface plot for a particular propeller condition ( $n = 9$  rps,  $\theta = 4.5^\circ$ , and  $H = 350$  mm) was developed, which shows the relationship among the mean velocity,  $x/D_p$ , and  $d/D_p$ . From the 3D surface plot it is noted that, at lower  $d/D_p$ , the mean velocity increases with  $x/D_p$ . As  $d/D_p$  increases, the trend of the mean axial velocity along  $x/D_p$  changes, showing gradually a decreasing trend of the axial velocity, particularly at higher  $d/D_p$ .

At the intermediate field ( $3.5 \leq x/D_p \leq 15.5$ ) and the far field ( $15.5 \leq x/D_p \leq 30.5$ ) zones, the maximum mean axial velocity is at the centre of the wake field ( $y = 0.0$ ), and thus this transverse location is of particular interest for the present research. Therefore in the thesis, the experimental results are analyzed mostly for this transverse location. The data for all the 168 locations considered for the research are presented in the thesis, and in the test report (Amin et al., 2017).

## CHAPTER 6 - CONCLUSION

From the present research, the propeller rotational speed is found as the most influential factor affecting the propeller wake velocity field. The higher the propeller rotational speed, the higher the mean axial velocity downstream in a wake field will be, and thus the more clearing of pack ice will take place. Propeller inclination also causes the mean axial velocity at the surface in a wake field to increase, but in a different way from propeller rotational speed. Propeller submergence affects the mean axial velocity near the free surface adversely. The findings of the research are in agreement with the findings of the earlier research by Ferrieri (2012) and Bastin (2014).

This study also covers the determination of the approximate size of the effective wake field, and provides some idea about the characteristics of the mean axial velocity throughout the propeller wake field for different combinations of factors used in the experiment. The prediction equations developed from the study can be applied to a large scale assessment, and most of the equations have good prediction capacities.

The experimental results are compared with the model results (Bastin, 2014) for three conditions at three different depths of measurements. The pattern of dissimilarities are found the same at each depth for all conditions, and the differences among the results are found to be considerable, particularly at higher depth ( $d/D_p = 1.05$ ). The comparison plots indicate the scopes for upgrading the mathematical model (Bastin, 2014). This research does not cover the study of the presence of turbulence along the propeller wake field, particularly at the near field zone, which was one of the major limitations of Bastin's model. The presence of turbulence in the vicinity of propeller

can be explained by the variability recorded during the experiment. Nevertheless, the axial component of velocity is the major contributor at the intermediate field, and at the far field zones in a propeller wake, which are typically more important than the near field zone from the context of clearing pack ice, as those zones cover most of the wake field. Also this study does not cover the interaction of the propeller jet with an ice floe, which was modeled by Bastin (2014).

The experimental results should be verified against some full-scale data, or the results obtained from a similar experiment performed by using some advanced measuring equipment, like PIV (Photo Image Velocimetry) or LDV (Laser Doppler Velocimetry). The experimental results can be used as a benchmark for CFD or similar numerical approaches.

One limitation of the current study is that the wake was assumed to be symmetrical and measurements were taken on only one side of the propeller centerline. This assumption was taken to provide more detail in the measured wake within the limitations of time and resources. For a single propeller, the wake may not be symmetrical and even the axial velocity distribution may be influenced by the direction of propeller rotation. Thus further work could be undertaken to determine the degree of lateral asymmetry in the wake field. Subsequently, more works need to be done to optimize the number of equations, developing only one prediction equation for fluid velocity.

## REFERENCES

- Albertson, M. L., Dai, Y. B., Jensen, R. A., Rouse, H. 1950. Diffusion of Submerged Jets. ASCE (American Society of Civil Engineers) Transactions, Paper no. 2409, Vol. 115, PP 639-697.
- Alfonski, G., Brambilla, S., and Chiuch, D. 2003. The use of Ultrasonic Doppler Velocimeter in Turbulent Pipe Flow. *Journal of Experiments in Fluid*, 35 (2003), Page 553-559
- Amin, A., Veitch, B., and Colbourne, B. 2017. Experimental Study on Propeller Wake Velocity Field. OERC (Ocean Engineering Research Centre) Report, Memorial University of Newfoundland, Report no. 2017-008.
- Anderson, K. G., McDonald, D., Mitten, P., Nicholls, S., and Tait, D. 1986. Management of Small Ice Masses. Environmental Studies Revolving Funds, Report no. 042.
- Bastin, T. 2014. Mathematical Modeling of Propeller Wake Wash for Pack-ice Management. *Master's Thesis*, 2014. Memorial University of Newfoundland, Canada.
- Bernal, L. P. and Scherer, J. 1997. Free Surface turbulent flows. American Institute of Aeronautics and Astronautics, Inc. University of Michigan, Ann Arbor.
- Blaauw, H. G., Van de Kaa, E. J. 1978. Erosion of Bottom and Sloping Banks caused by the Screw race of Maneuvering Ships. Delft Hydraulics laboratory, Netherlands, Report no. 202.
- Brewster, P. M. 1997. Modeling the Wash from a Ship's Propeller. *Ph.D Thesis*, Queen's University of Belfast, UK.

Crocker, G., Wright, B., Thistle, S., Bruneau, S. 1998. An assessment of current iceberg management capabilities. Report for: National Research Council Canada, Prepared by C-Core and B. Wright & Associates, Ltd.. Program of Energy Research and Development / CHC, Report no. 20-33.

Design Expert 9.0 software. The software which is used to develop the 3D surface plots and regression equations showing the relationship among factors and response.

Eik, K. J. 2009. Ice Management. The 4<sup>th</sup> Norway-Russia Arctic Offshore Workshop, Statoil Hydro Research Centre, Norway.

Ferrieri, J. M., Veitch, B. and Akinturk, A. 2013. Experimental Study on Ice Management through the use of Podded Propeller Wash. Third Symposium on Marine Propulsors, Australia.

Ferrieri, J. M. 2012. Experimental Study on Ice Management through the use of Podded Propeller Wash. *Master's Thesis*, Memorial University of Newfoundland, Canada.

Fuehrer, M., Romisch, K. 1977. Effects of Modern Ship Traffic on Islands and Ocean Waterways and their Structures. Proceedings 24th Congress P.I.A.N.C., Leningrad, Sections 1-3.

Hamill, G.A., and Johnson H. T. 1993. The decay of Maximum velocity within the initial stages of a Propeller Wash. *Journal Hydrodynamic Research Delft Tech. University*.

Hamill, G. A., Johnson H. T., Wilson, P. R., Ryan, D. 2013. Influence of a Boundary on the development of Propeller Wash. *Journal of Ocean Engineering*, 61, 50-55

Hamill, G. A. 1987. Characteristics of the Screw Wash of a Maneuvering Ship and the resulting Bed Scour. *PhD Thesis*. Queen's University of Belfast, UK.

Hamilton, J. M. 2011 The challenges of deep water Arctic Development. Proceedings of International Offshore and Polar Engineering Conference, Hawaii.

Hamilton, J. M., Holub, C. J., Blunt, J. 2011. Simulation of IM fleet operations using two decades of Beaufort Sea Ice Drift and Thickness Time Histories. Proc. of the 21st International Offshore and Polar Engineering Conference.

Hashmi, H. N. 1993. Erosion of a granular bed at a Quay wall by a Ship's Screw Wash. *PhD Thesis*. Queen's University of Belfast, UK.

Hisette, Q., Jochmann, P., Bronsart, R. 2014. Simulation of Ice Management Operations. Proc. of the 24th International Ocean and Polar Engineering Conf. (ISOPE).

Hout, R. V., Gulitski, A., Barnea, D., Shemer, L. 2002. Experimental investigation of the velocity field induced by a Taylor bubble rising in stagnant water. *International Journal of Multiphase Flow*.

Keinonen, A.J., Lohi, P. 2000. Azimuth and multipurpose icebreaker technology for arctic and non-arctic offshore. *Proceedings, Offshore and Polar Engineering Conference*, Seattle.

Keinonen, A. J. 2008. Ice management for ice offshore operations. Proceedings, Offshore Technology Conference, Houston.

Keinonen, J. A., Browne, R., Lam, E., Jolles, W. 2006. Six years in Sakhalin Offshore Oil - Management of Risk and Operations in Ice. Conference Paper (ICETECH 2006)

Keinonen, J. A., and Martin, E. 2010. Ice Risk Management for Stationary Vessel Operations in moving Pack Ice in ice Offshore Experience and State of Art. ICETECH Conference, 2010.

Lam, W. H., Hamill, G. A., Robinson, D., Raghunathan, S. 2010. Observations of the initial 3D flow from a Ship's Propeller. *Journal of Ocean Engineering*, 37, 1380- 1388.

Lam, W., Robinson, D. J., Hamill, G. A., and Raghunathan, S. 2010a. Axial velocity distribution at the Efflux of a stationary unconfined Ship's Propeller Jet. OMAE Conference.

Lam, W. H., Hamill, G. A., Song, Y. C. 2011. Experimental Investigation of the decay from a Ship's Propeller. *China Ocean Engineering*, 25:2, 265-284.

Lam, W., Robinson, D. J., Hamill, G. A., Raghunathan, S. 2012. Semi-empirical methods for determining the Efflux velocity from a Ship's Propeller. *Journal of Applied Ocean Research*, 2012

Lam, W. H., Hamill, G. A., Raghunathan, S., Song, Y. C. 2012a. Analysis of the 3D zone of flow establishment from a Ships Propeller. *KSCE Journal of Civil Engineering* 16(4): 465-477.

Lam, W., Robinson, D. J., Hamill, A. 2013. Initial wash profiles from a Ship's Propeller using CFD method. *Journal of Ocean Engineering*, 2013.

Loufer, J. 1953. The structure of turbulence in fully developed pipe flow. Report no. 1174 for National Advisory Committee for Aeronautics.

Lye, L. ENGI 9516: Design of Experiment Methodology - Course Lecture Notes. Memorial University of Newfoundland, Canada.

Madnia, K., and Bernal, L. P. 1994. Interaction of a turbulent round Jet with the Free Surface. *Journal of Fluid Mechanics*, Vol. 261, 305-322. Department of Aerospace Engineering, The University of Michigan, Ann Arbor.

Martin, H. E., Keinonen, J. A., Brown, H. 2008. Ice Management Effectiveness Predictions. ICETECH Conference, 2008.

McGarvey, J. A. 1996. The influence of the Rudder on the Hydrodynamics and the resulting bed Scour of a Ship's Screw Wash. *PhD Thesis*. Queen's University of Belfast, UK.

Montgomery, D. C. 2013. Design and Analysis of the experiments. 8th edition. John Wiley & Sons. Inc, New York , USA.

Palmer, A. and Croasdale, K. 2012. Arctic Offshore Engineering. World Scientific Publishing Company.

Stewart, D. P. J. 1992. Characteristics of a Ship's Screw Wash and the influence of Quay Wall Proximity. *PhD Thesis*. Queen's University of Belfast, UK.

Taylor, R. 2016. Arctic Offshore Engineering Course Lecture Notes. Memorial University of Newfoundland, Canada.

Tian, J. 2011. Free Surface confinement effects on a round Jet. *Master's Thesis*. University of Windsor.

Timco, G. 2007. Grand Banks Iceberg Management. NRC Publications, Canada.

Verhey, H. J. 1983. The Stability of Bottom Banks subjected to velocities in the Propeller Jet behind Ships. 8<sup>th</sup> International Harbor Congress, Belgium, 1983.

Walker, D. T., Chen, C. Y., Willmarth, W. W. 1995. Turbulent structure in Free Surface Jet flows. *J. Fluid Mechanics*, 291, 223-262

Wynanski, I., Fiedler, H. 1969. Some Measurements in the Self-Preserving Jet. *Journal of Fluid Mechanics*, 38 (3), 577-612.

## **APPENDICES**

### Appendix 'A' - More Plots for the Mean Axial Velocity and the Variability of Flow (Standard Deviation)

In Appendix 'A', the plots mentioned in Section 4.3.1 for the other 2 cases are shown. The plots show the 'mean axial velocity' and 'mean  $\pm$  standard deviation' along  $x/D_p$  at the centre of the wake. Case 1 shows the plots for experimental run #1, where the propeller rotational speed = 6 rps, inclination angle =  $4.5^\circ$ , and depth of submergence of propeller = 350 mm. Then Case 2 shows the plots for experimental run #2, where the propeller rotational speed = 9 rps, inclination angle =  $9^\circ$ , and depth of submergence of propeller = 350 mm.

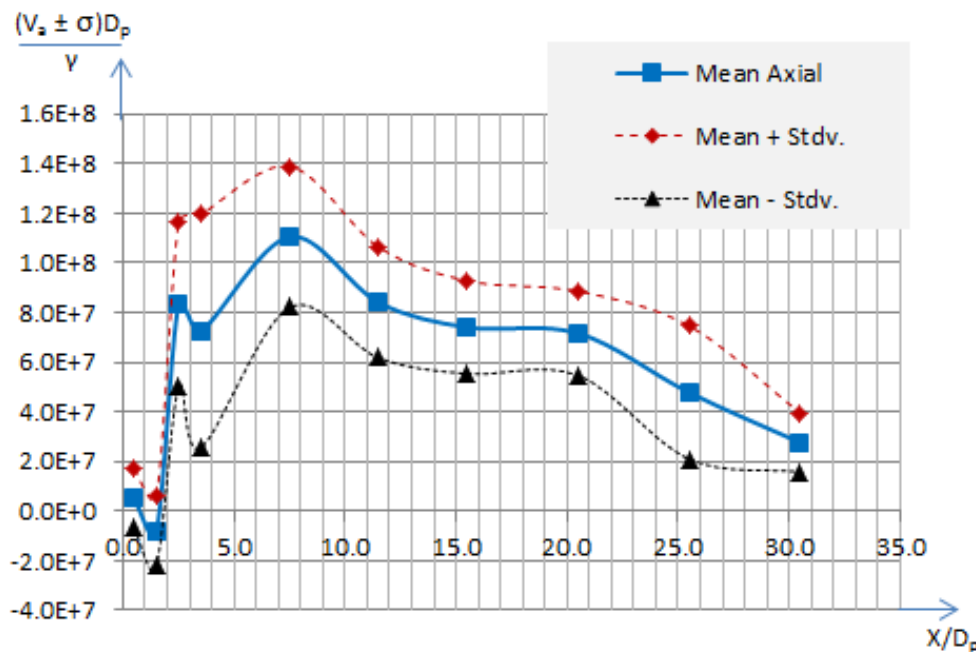


Figure A1: Mean axial velocity and mean velocity incorporating standard deviation along  $x/D_p$  at a depth of  $0.25D_p$  from water surface and at  $y/D_p = 0.0$  for **Case 1**

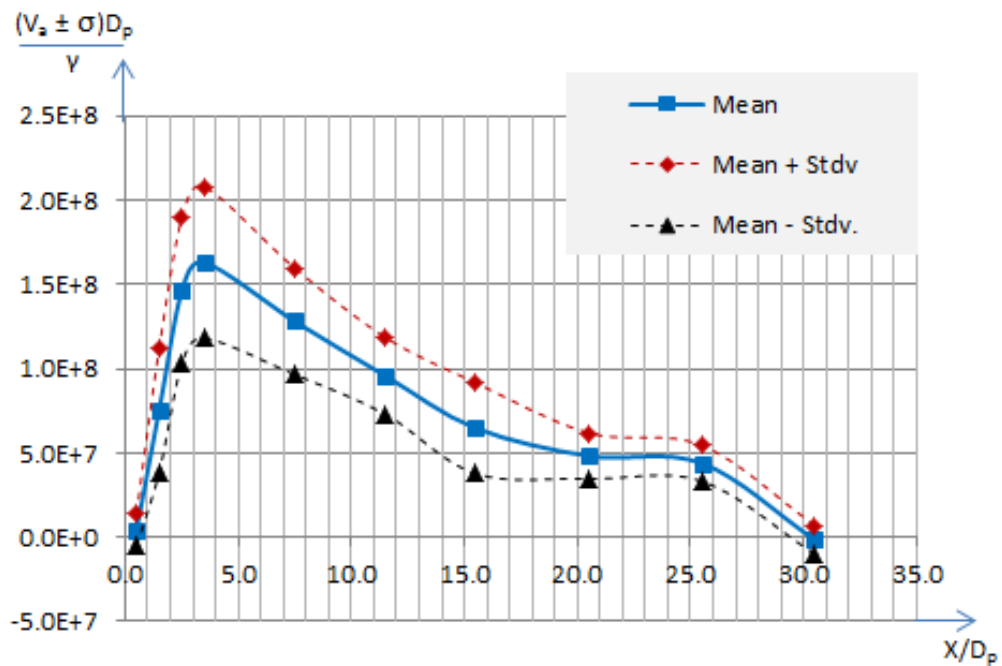


Figure A2: Mean axial velocity and mean velocity incorporating standard deviation along  $x/D_p$  at a depth of  $0.55D_p$  from the water surface and of  $y/D_p = 0.0$  for **Case 1**

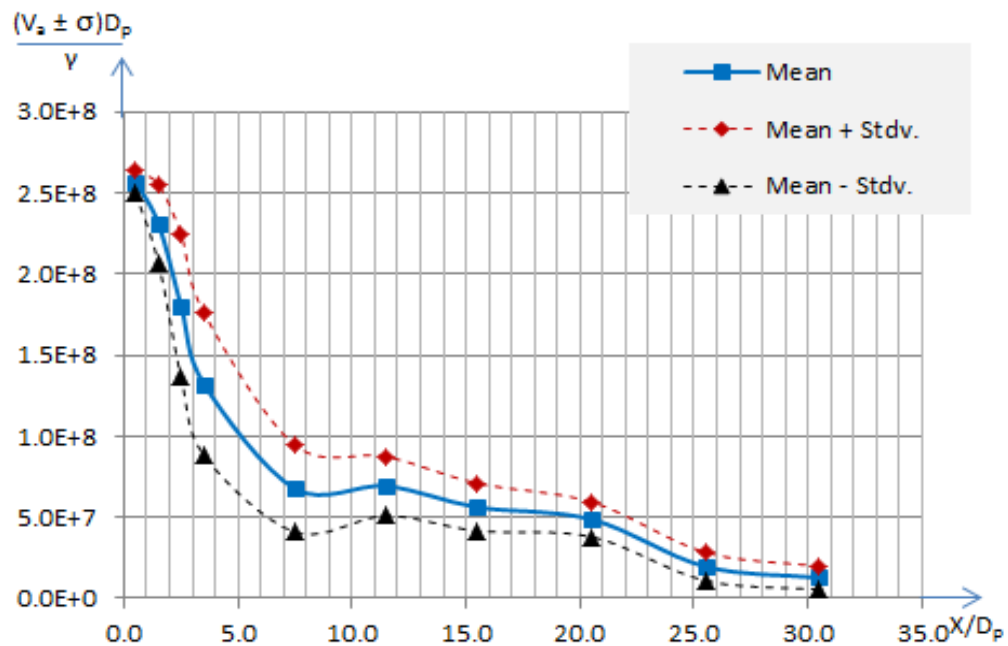


Figure A3: Mean axial velocity and mean velocity incorporating standard deviation against  $x/D_p$  at a depth of  $1.05D_p$  from the water surface and at  $y/D_p = 0.0$  for **Case 1**

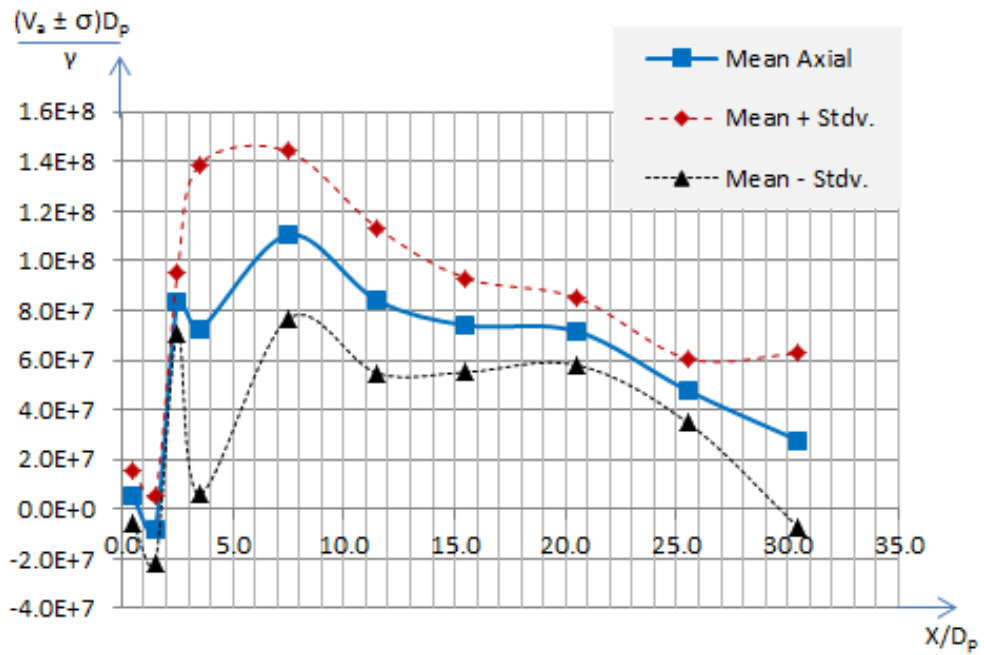


Figure A4: Mean axial velocity and mean velocity incorporating standard deviation against  $x/D_p$  at depth of  $0.25D_p$  from the water surface and at  $y/D_p = 0.0$  for **Case 2**

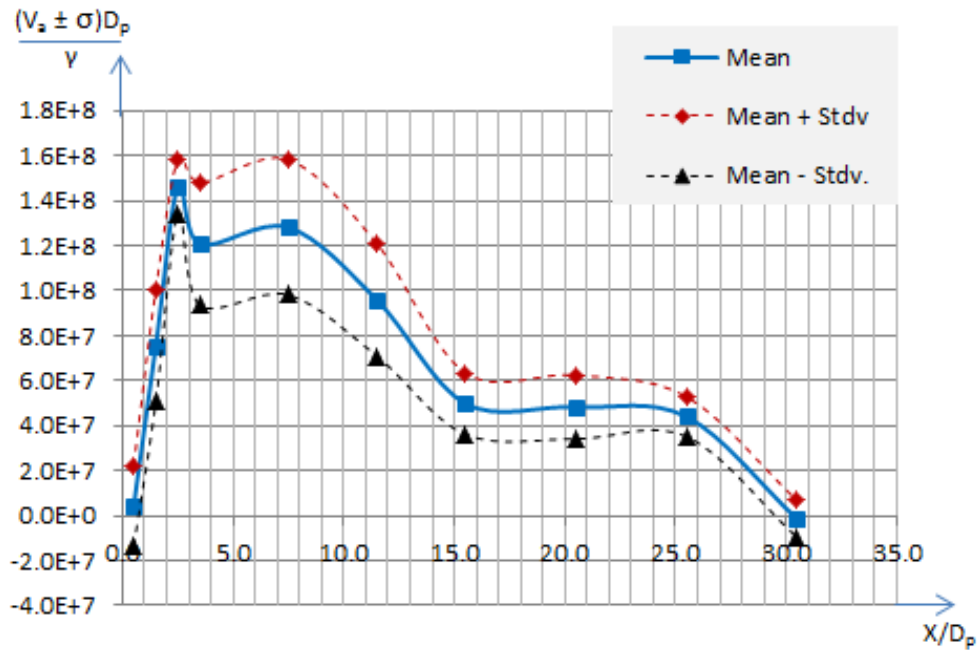


Figure A5: Mean axial velocity and mean velocity incorporating standard deviation along  $x/D_p$  at depth of  $0.55D_p$  from the water surface and at  $y/D_p = 0.0$  for **Case 2**

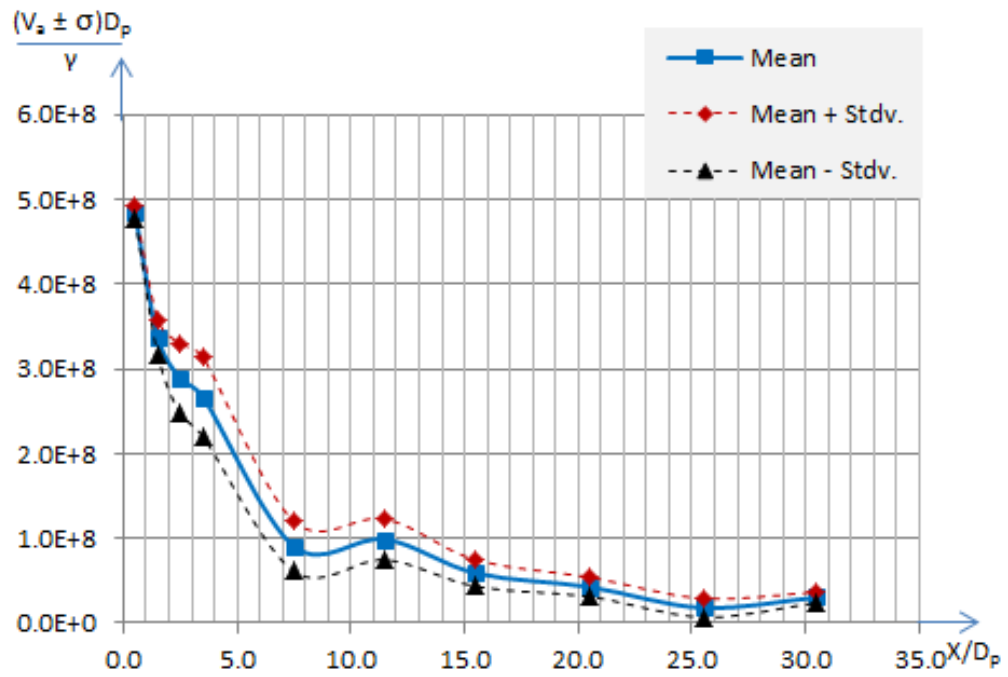


Figure A6: Mean axial velocity and mean velocity incorporating standard deviation along  $x/D_p$  at a depth of  $1.05D_p$  from the water surface and at  $y/D_p = 0.0$  for **Case 2**

### Appendix 'B' - More Plots showing the Individual Effect of Factors

In Appendix 'B', the plots mentioned in Section 4.3.2 for the other case are shown. The plots illustrate the mean axial velocity along  $x/D_p$  at  $y = 250$  mm (transversely 250 mm offset from the centre of the wake field) for the same propeller conditions as described in Section 4.3.2, in order to show the individual effect of the factors on fluid velocity by applying OFAT. Firstly, from Figure B1 to Figure B3 show the mean axial velocity of flow along  $x/D_p$  for 3 different shaft rotational speeds at  $y/D_p = 1.0$  (or  $y = 250$  mm). Similarly, from Figure B4 to Figure B6, and from Figure B7 to Figure B9 show the mean axial velocity of flow along  $x/D_p$  at 3 different propeller inclinations and depths of submergence, respectively.

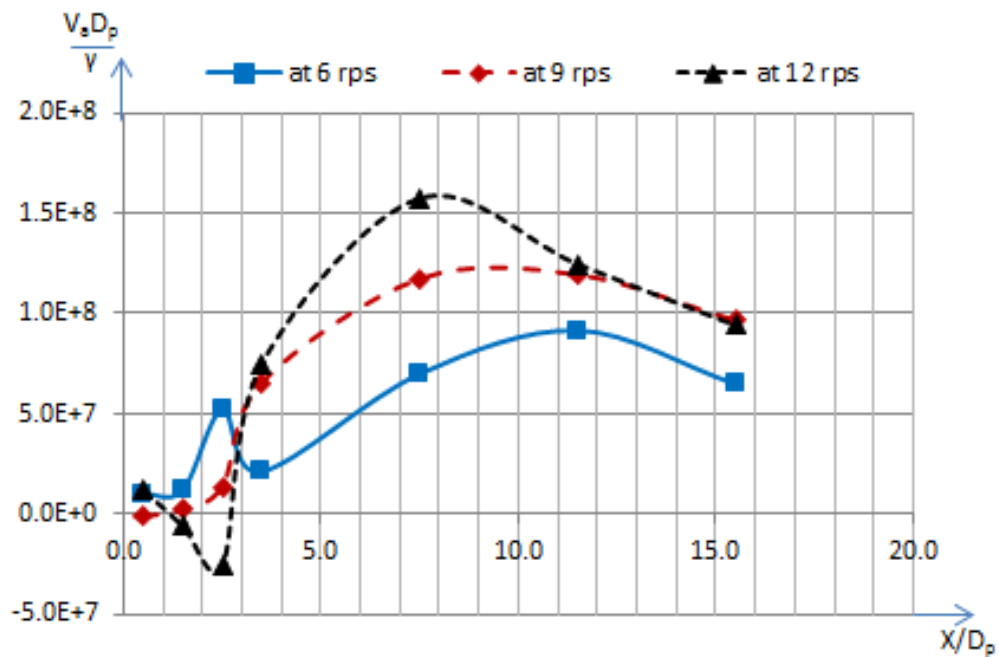


Figure B1: Mean axial velocity at different rotational speeds along  $x/D_p$  for  $H = 350$  mm and  $\theta = 4.5^\circ$  at a depth of  $0.25D_p$  from the water surface and at  $y/D_p = 1.0$

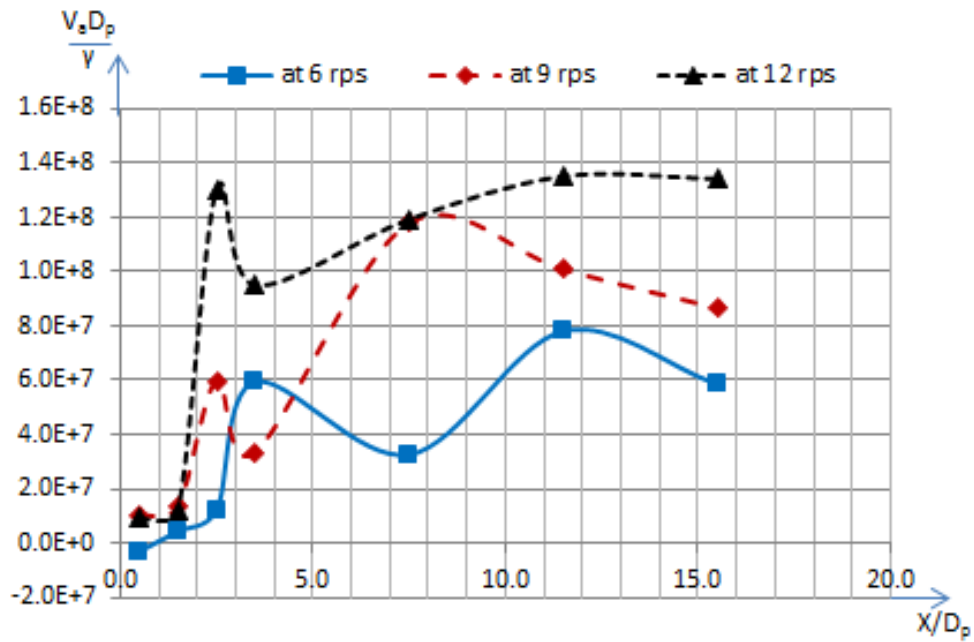


Figure B2: Mean axial velocity at different rotational speeds along  $x/D_p$  for  $H = 350$  mm and  $\theta = 4.5^\circ$  at a depth of  $0.55D_p$  from the water surface and at  $y/D_p = 1.0$

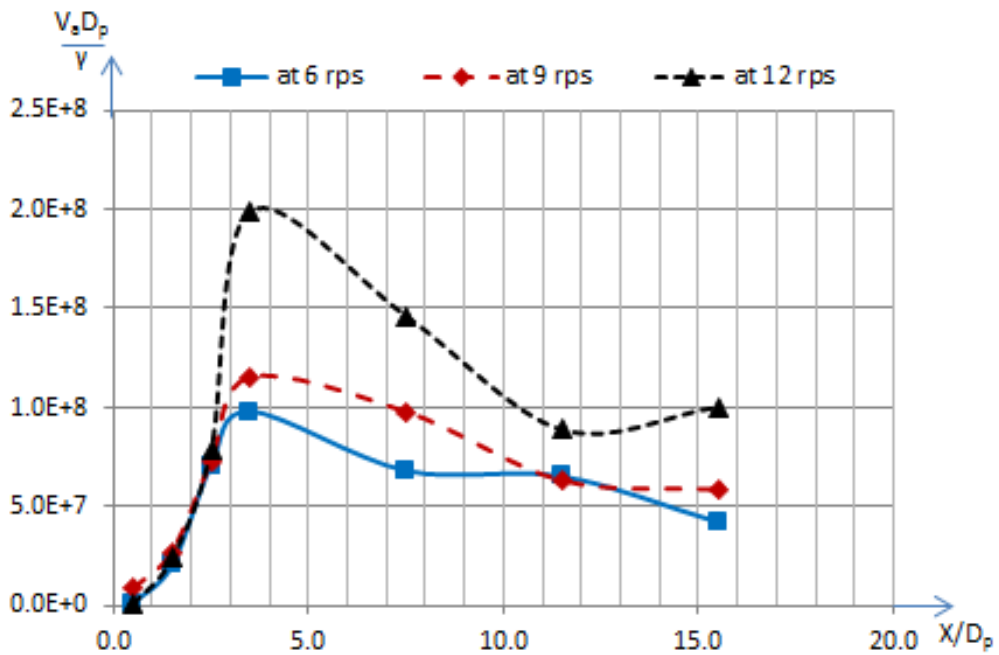


Figure B3: Mean axial velocity at different rotational speeds along  $x/D_p$  for  $H = 350$  mm and  $\theta = 4.5^\circ$  at a depth of  $1.05D_p$  from the water surface and at  $y/D_p = 1.0$

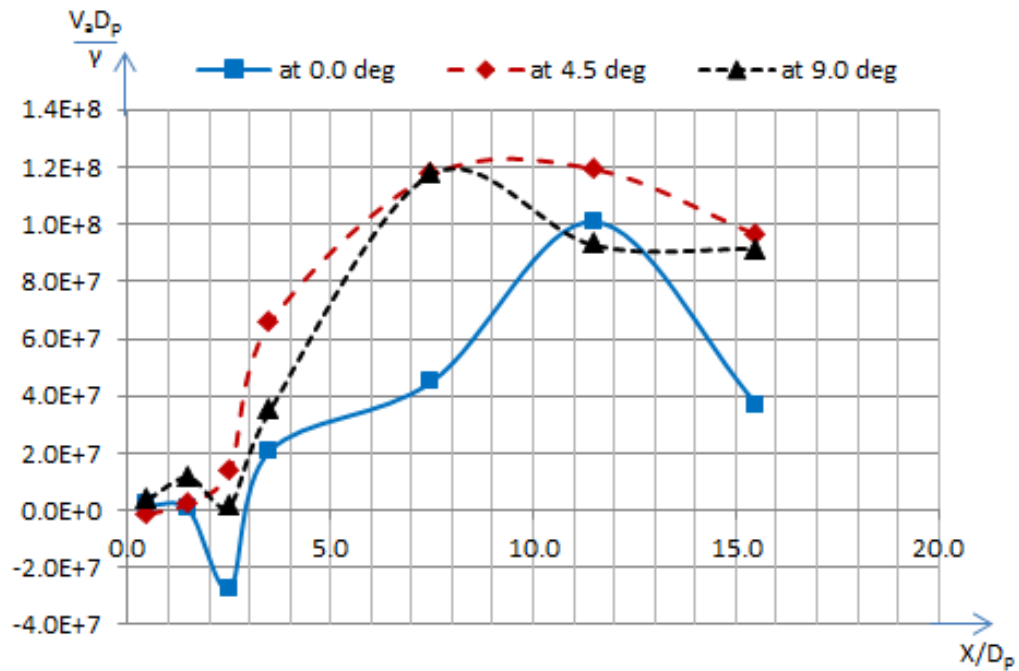


Figure B4: Mean axial velocity at different propeller inclinations along  $x/D_p$  for  $H = 350$  mm and  $\theta = 4.5^\circ$  at a depth of  $0.25D_p$  from the water surface and at  $y/D_p = 1.0$

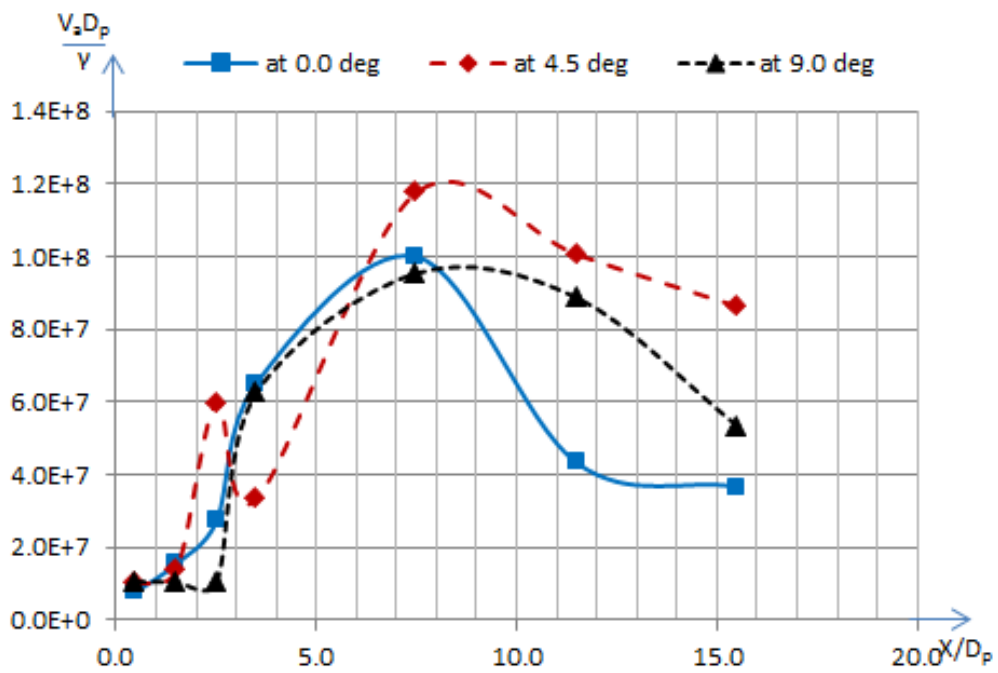


Figure B5: Mean axial velocity at different propeller inclinations along  $x/D_p$  for  $H = 350$  mm and  $\theta = 4.5^\circ$  at a depth of  $0.55D_p$  from the water surface and at  $y/D_p = 1.0$

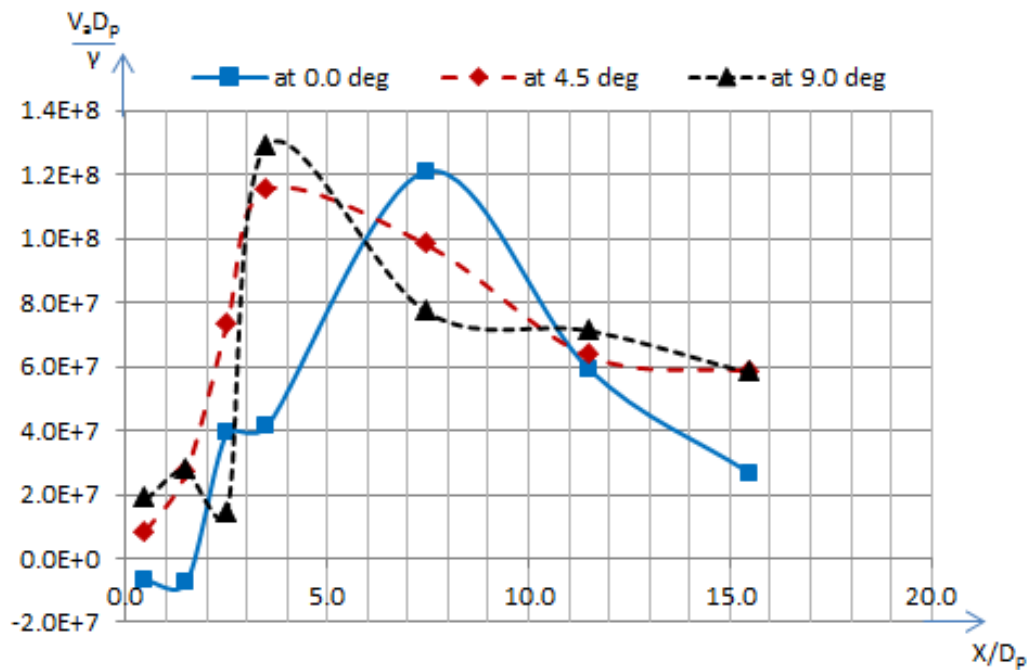


Figure B6: Mean axial velocity at different propeller inclinations along  $x/D_p$  for  $H = 350$  mm and  $\theta = 4.5^\circ$  at a depth of  $1.05 D_p$  from the water surface and at  $y/D_p = 1.0$

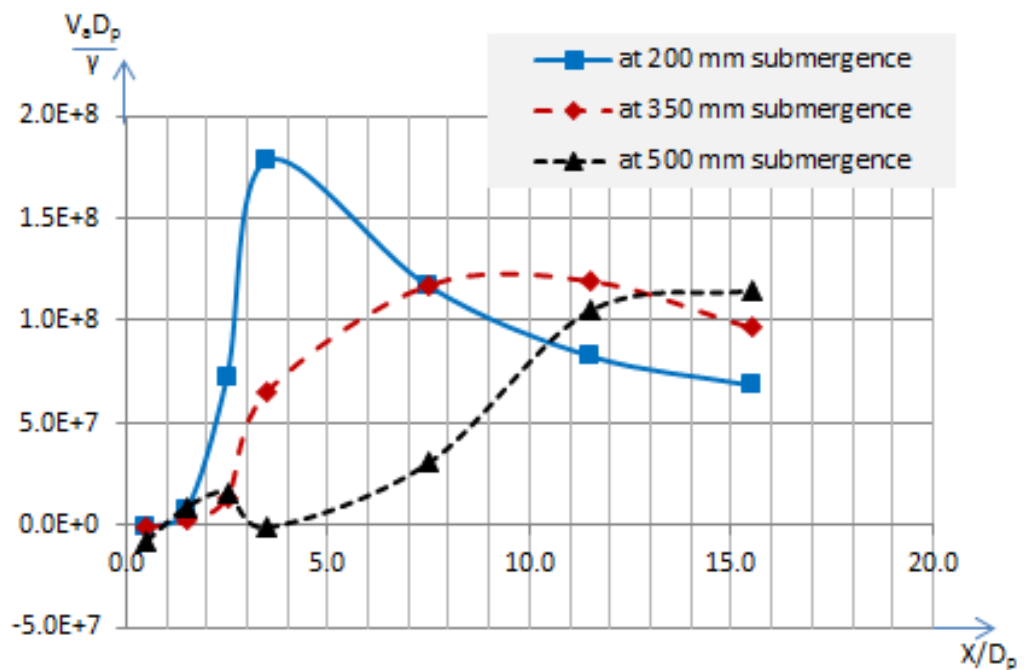


Figure B7: Mean axial velocity at different propeller submergence along  $x/D_p$  for  $H = 350$  mm and  $\theta = 4.5^\circ$  at a depth of  $0.25 D_p$  from the water surface and at  $y/D_p = 1.0$

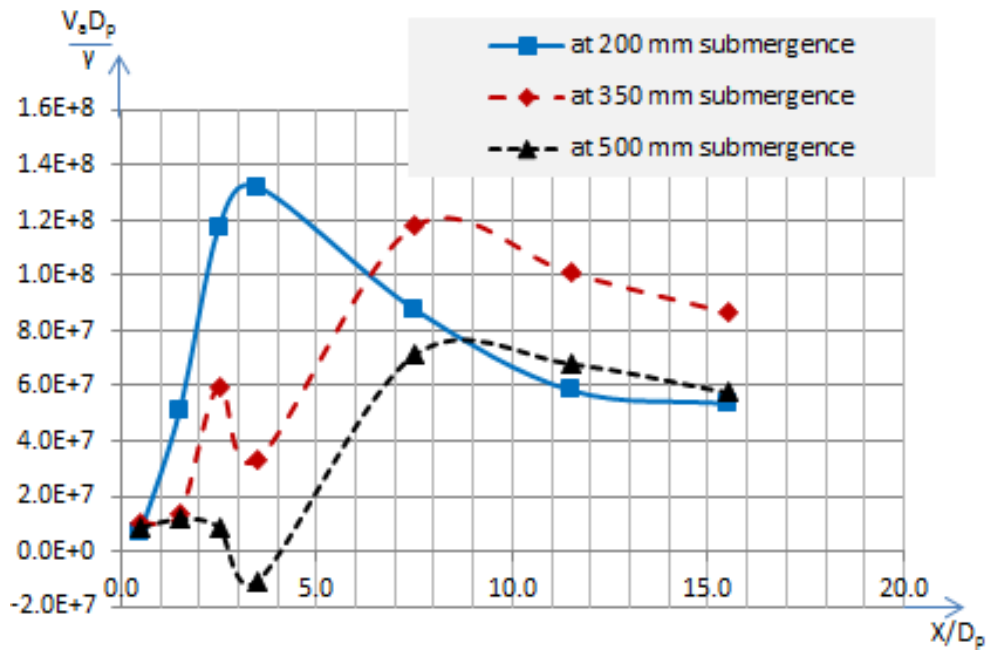


Figure B8: Mean axial velocity at different propeller submergence along  $x/D_p$  for  $H = 350$  mm and  $\theta = 4.5^\circ$  at a depth  $0.55D_p$  from the water surface and at  $y/D_p = 1.0$

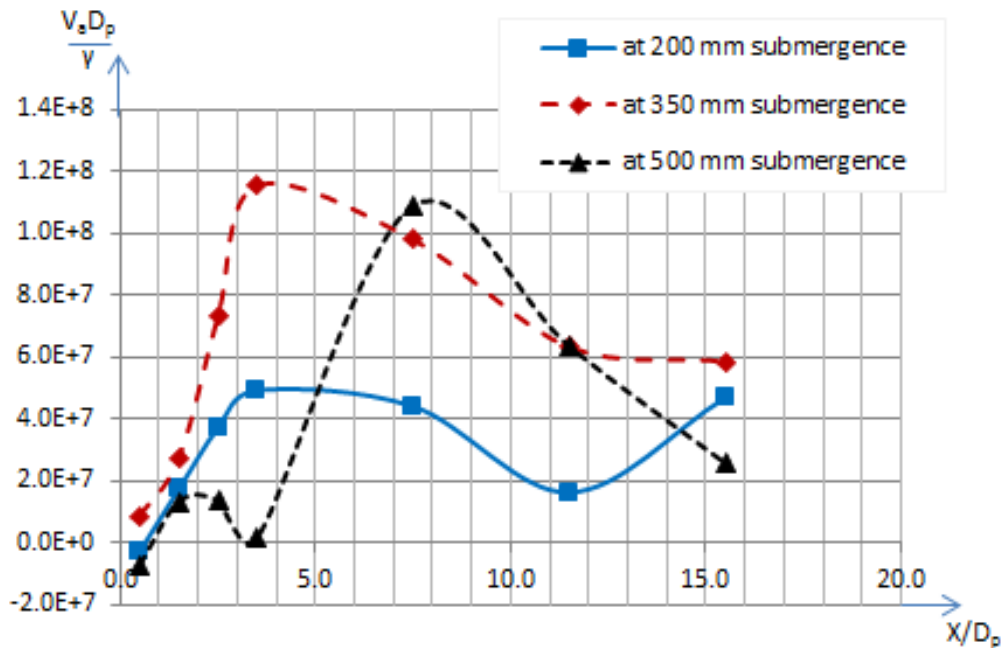


Figure B9: Mean axial velocity at different propeller submergence along  $x/D_p$  for  $H = 350$  mm and  $\theta = 4.5^\circ$  at a depth of  $1.05D_p$  from the water surface and at  $y/D_p = 1.0$

**Appendix ‘C’ - More Plots showing the Comparison of Experimental Results  
with Model Results (Bastin, 2014)**

The plots mentioned in Section 4.3.3 for the other 2 cases are shown. The plots show the mean axial velocity along  $x/D_p$  at the centre of the wake. Case 1 shows the plots for the propeller configuration: propeller rotational speed = 6 rps, propeller inclination angle =  $4.5^\circ$ , and depth of submergence of propeller from fluid surface = 350 mm. Then Case 2 shows the plots for the propeller configuration: propeller rotational speed = 9 rps, propeller inclination angle =  $9^\circ$ , and depth of submergence of propeller = 350 mm.

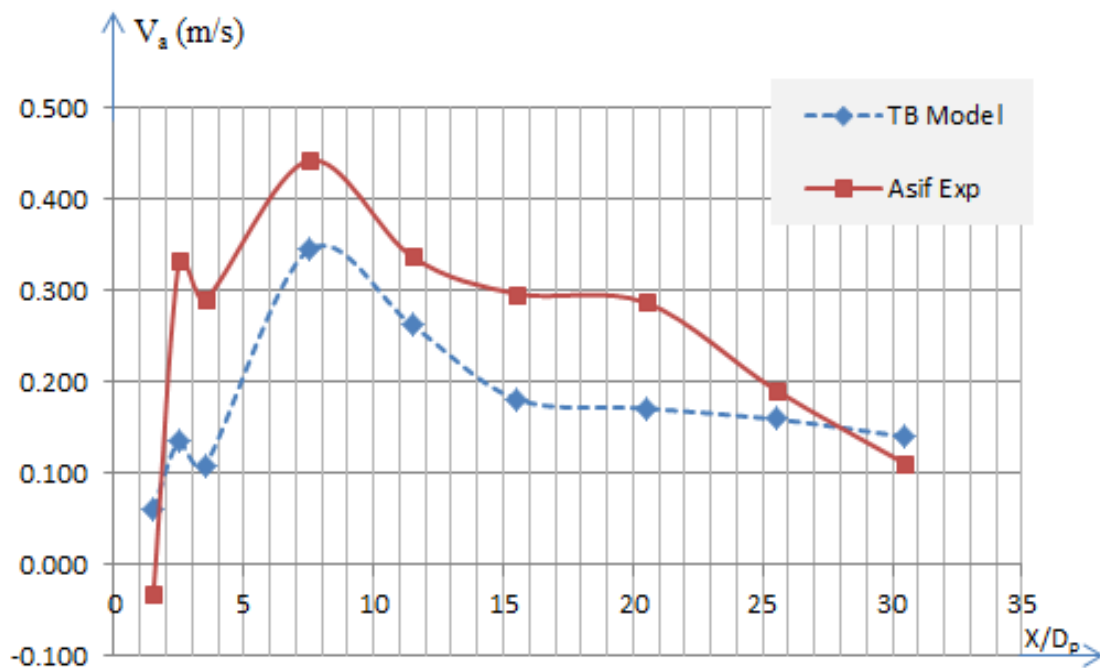


Figure C1: Mean axial velocity (m/s) along  $x/D_p$  at a depth of  $0.25D_p$  from the water surface and at  $y/D_p = 0.0$  for **Case 1**

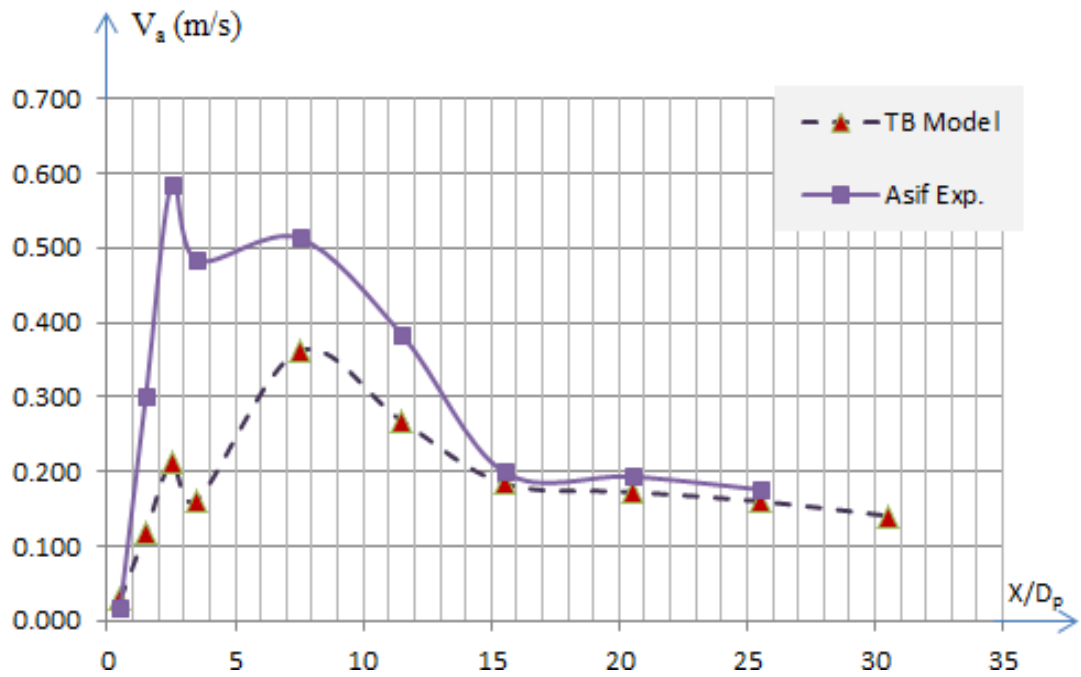


Figure C2: Mean axial velocity (m/s) along  $x/D_p$  at a depth of  $0.55D_p$  from the water surface and at  $y/D_p = 0.0$  for **Case 1**

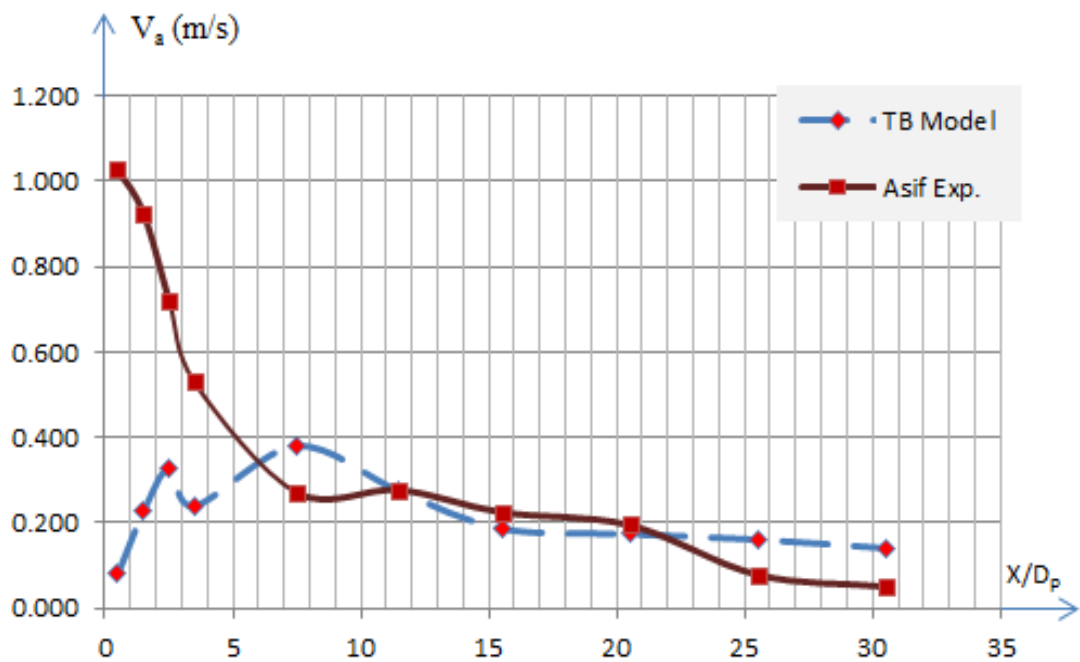


Figure C3: Mean axial velocity (m/s) along  $x/D_p$  at a depth of  $1.05D_p$  from the water surface and at  $y/D_p = 0.0$  for **Case 1**

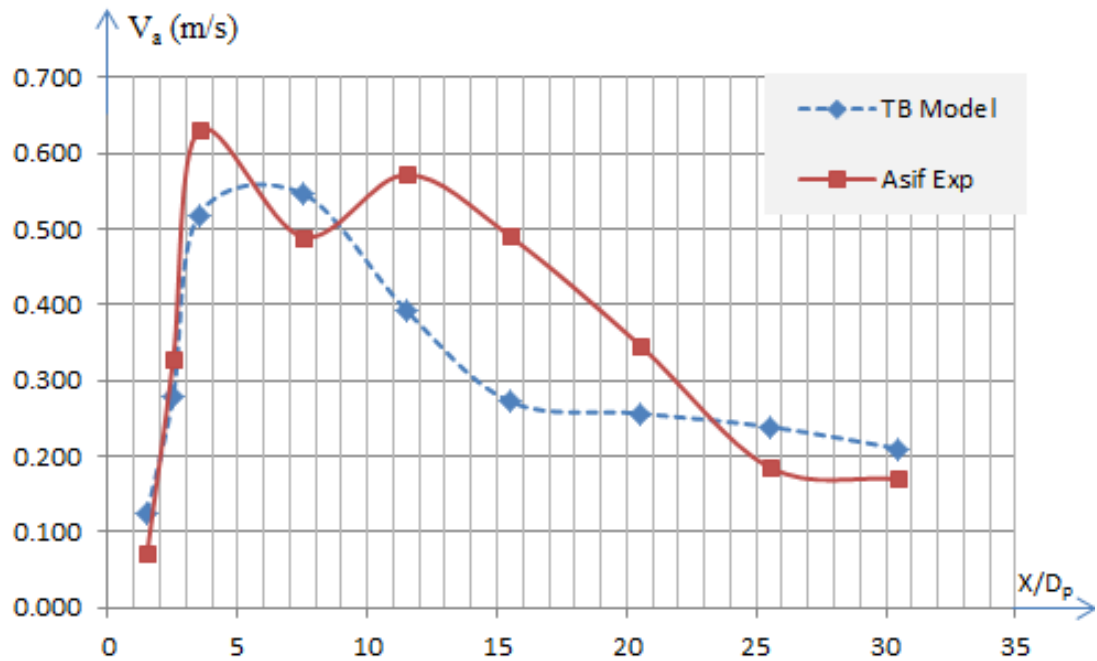


Figure C4: Mean axial velocity (m/s) along  $x/D_p$  at a depth of  $0.25D_p$  from the water surface and at  $y/D_p = 0.0$  for **Case 2**

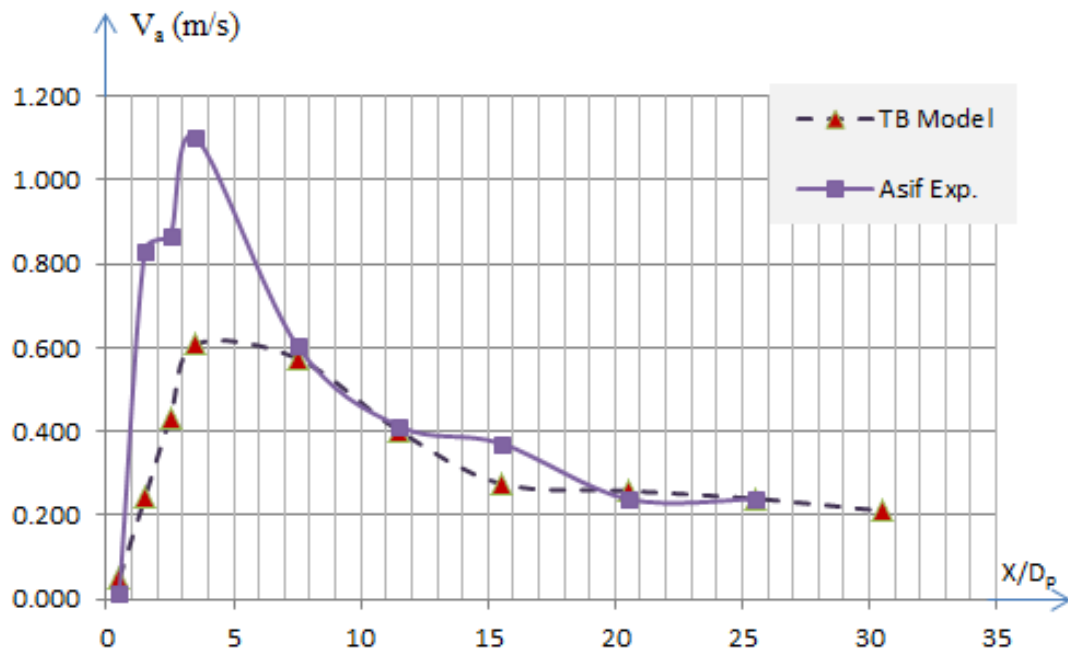


Figure C5: Mean axial velocity (m/s) along  $x/D_p$  at a depth of  $0.55D_p$  from water surface and at  $y/D_p = 0.0$  for **Case 2**

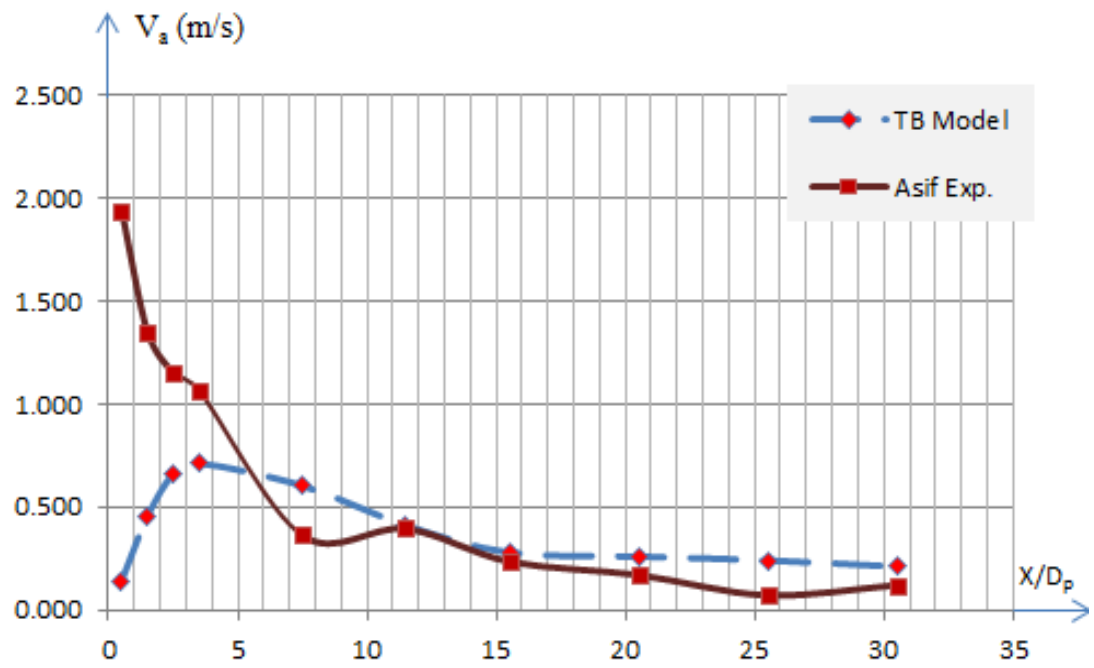


Figure C6: Mean axial velocity (m/s) along  $x/D_p$  at a depth of  $1.05D_p$  from the water surface and at  $y/D_p = 0.0$  for **Case 2**

**Appendix ‘D’ - More Plots showing the Characteristics of the Mean Axial  
Velocity along  $x/D_p$  at  $d/D_p = 0.25$**

In Section 4.3.5, some plots are shown to illustrate the effect of propeller rotational speed ‘n’ on the trend of the mean axial velocity of flow along  $y/D_p$  downstream of the propeller wake at  $d/D_p = 0.25$ . In this section, the effect of propeller inclination ‘ $\theta$ ’ and propeller submergence ‘H’ are shown by providing the rest of the plots mentioned in Section 4.3.5. To explain the effect of ‘ $\theta$ ’ on the mean axial velocity the 3 experimental conditions considered are the same as considered for the analysis in Section 4.3.2: experimental run #5, average of CP runs, and run #2. From Figure D1 to Figure D4 illustrate the remaining plots that show the effect of propeller inclination.

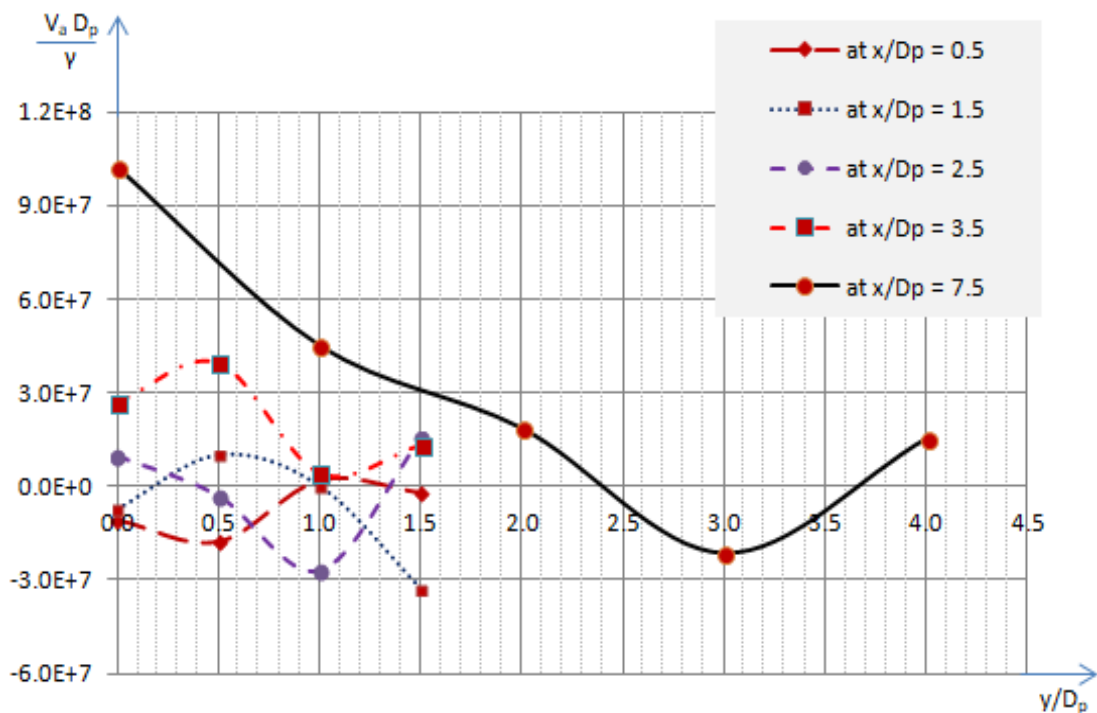


Figure D1: Mean axial velocity along  $y/D_p$  at  $x/D_p = 0.50, 1.50, 2.50, 3.50$  and  $7.50$ ;

for  $n = 9$  rps,  $\theta = 0^\circ$  and  $H = 350$  mm

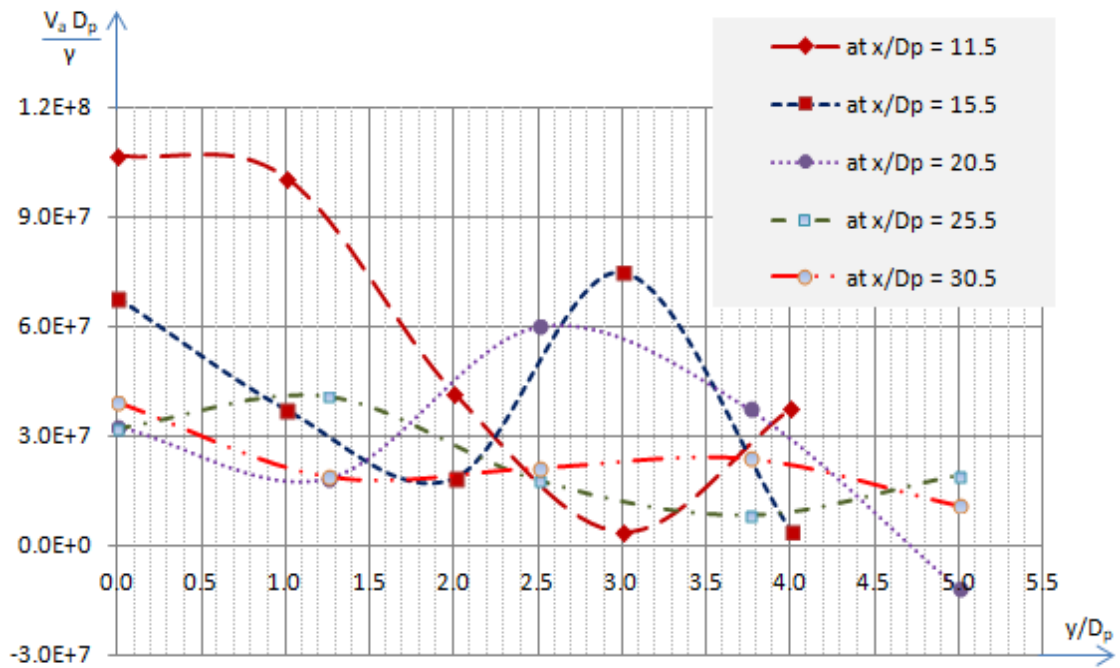


Figure D2: Mean axial velocity along  $y/D_p$  at  $x/D_p = 11.5, 15.5, 20.5, 25.5$  and  $30.5$ ; for  $n = 9$  rps,  $\theta = 0^\circ$  and  $H = 350$  mm

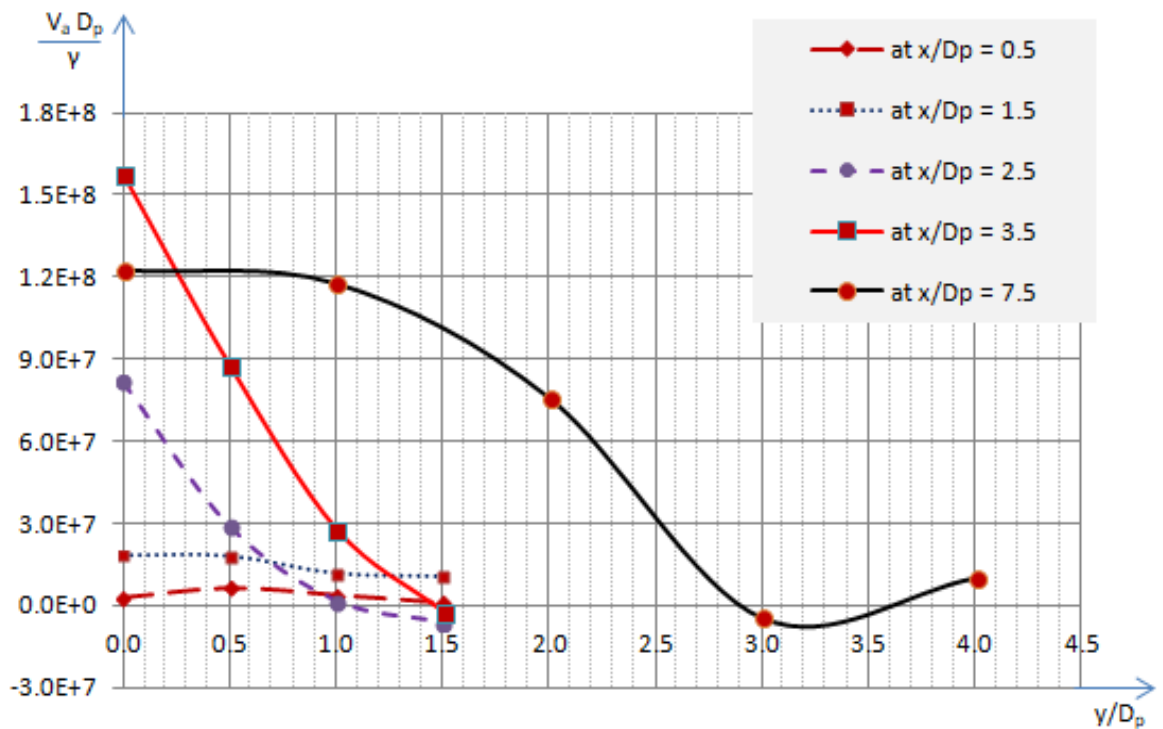


Figure D3: Mean axial velocity along  $y/D_p$  at  $x/D_p = 0.5, 1.5, 2.5, 3.5$  and  $7.5$ ; for  $n = 9$  rps,  $\theta = 9^\circ$  and  $H = 350$  mm

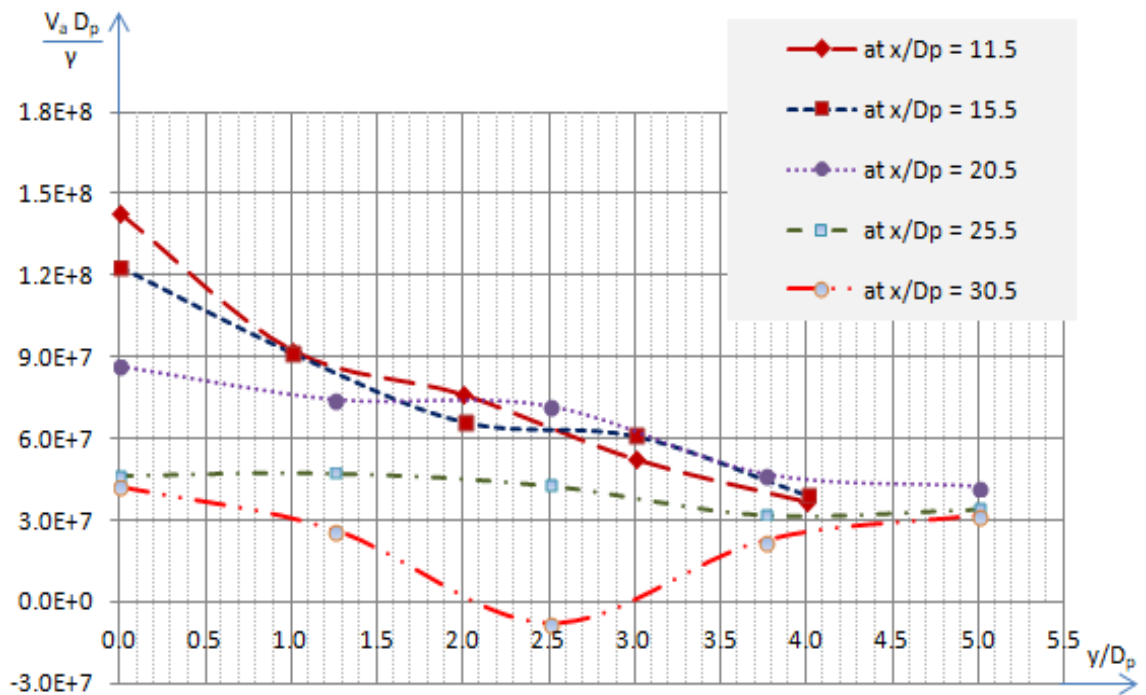


Figure D4: Mean axial velocity along  $y/D_p$  at  $x/D_p = 11.50, 15.50, 20.50, 25.50$  and  $30.50$ ; for  $n = 9$  rps,  $\theta = 9^\circ$  and  $H = 350$  mm

To explain the effect of ‘H’ on the mean axial velocity the following 3 experimental conditions are considered, which are the same as considered for the analysis shown in Section 4.3.2: experimental run #14, average of CP runs, and run #13. From Figure D5 to Figure D4, the remaining plots that illustrate the effect of propeller submergence are shown.

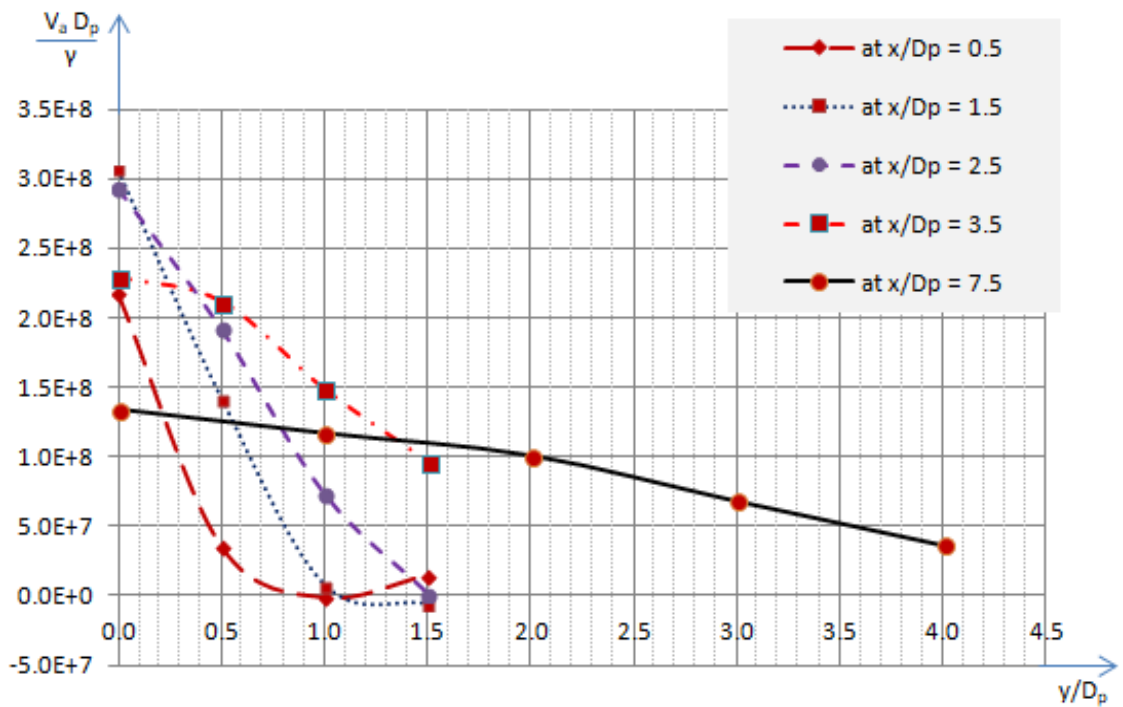


Figure D5: Mean axial velocity along  $y/D_p$  at  $x/D_p = 0.5, 1.5, 2.5, 3.5$  and  $7.5$ ;

for  $n = 9$  rps,  $\theta = 4.5^\circ$  and  $H = 200$  mm

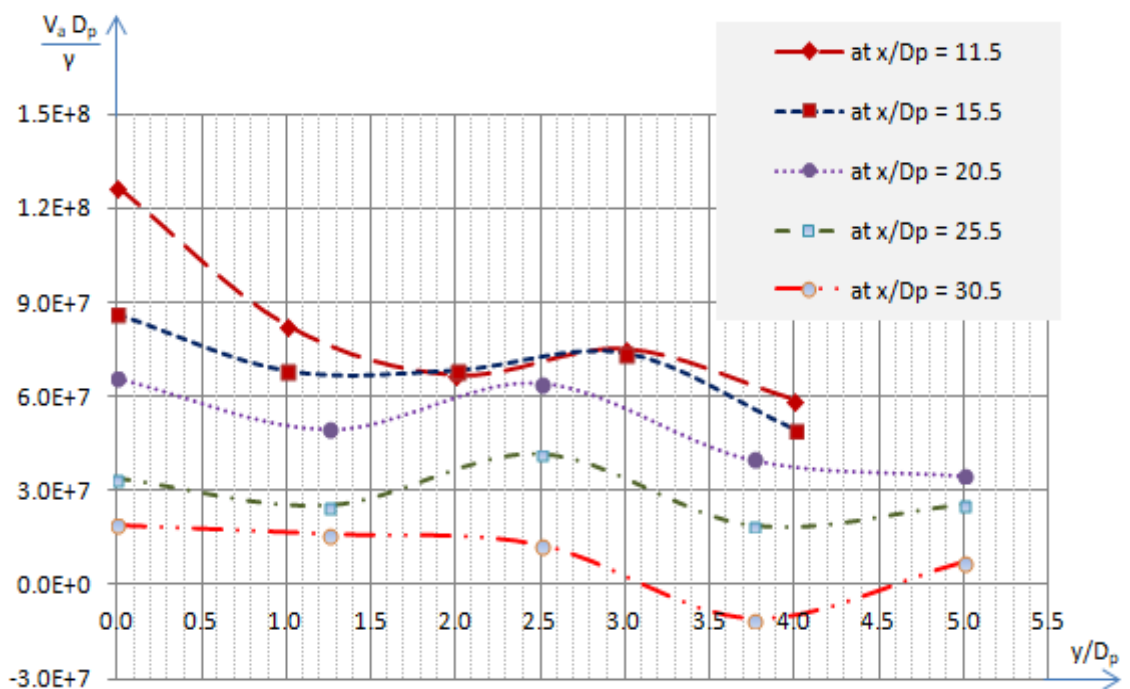


Figure D6: Mean axial velocity with  $y/D_p$  at  $x/D_p = 11.5, 15.5, 20.5, 25.5$  and

$30.5$ ; for  $n = 9$  rps,  $\theta = 4.5^\circ$  and  $H = 200$  mm

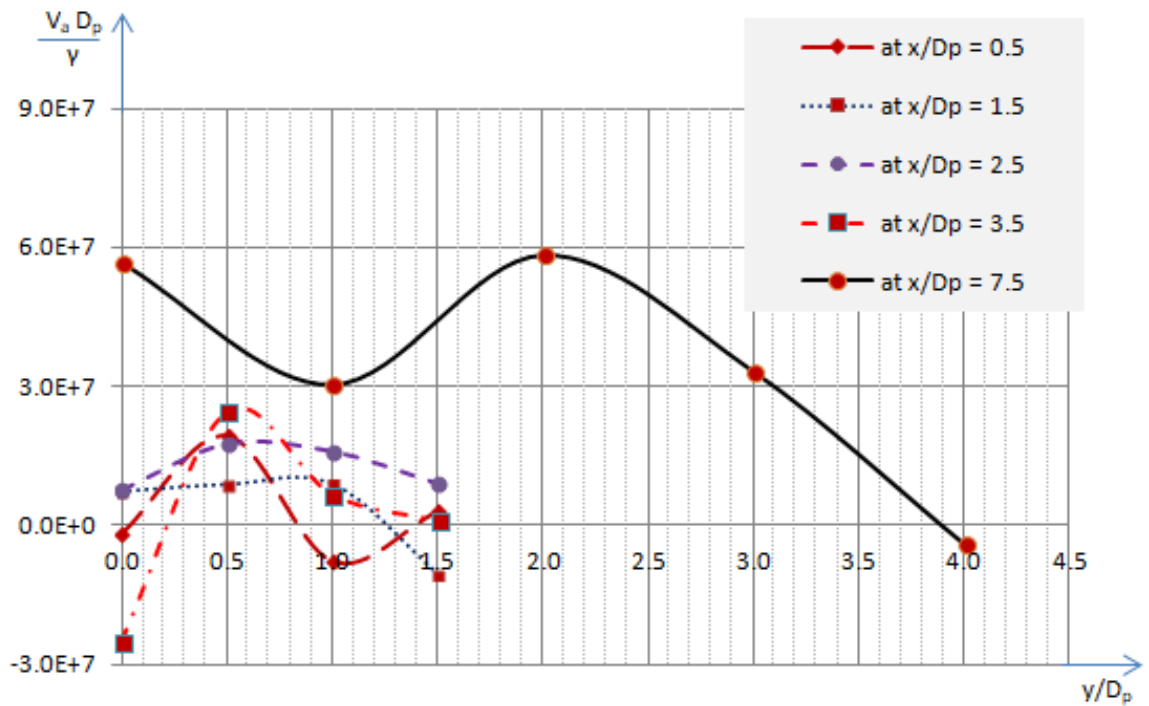


Figure D7: Mean axial velocity along  $y/D_p$  at  $x/D_p = 0.50, 1.50, 2.50, 3.50$  and  $7.50$ ;

for  $n = 9$  rps,  $\theta = 4.5^\circ$ , and  $H = 500$  mm

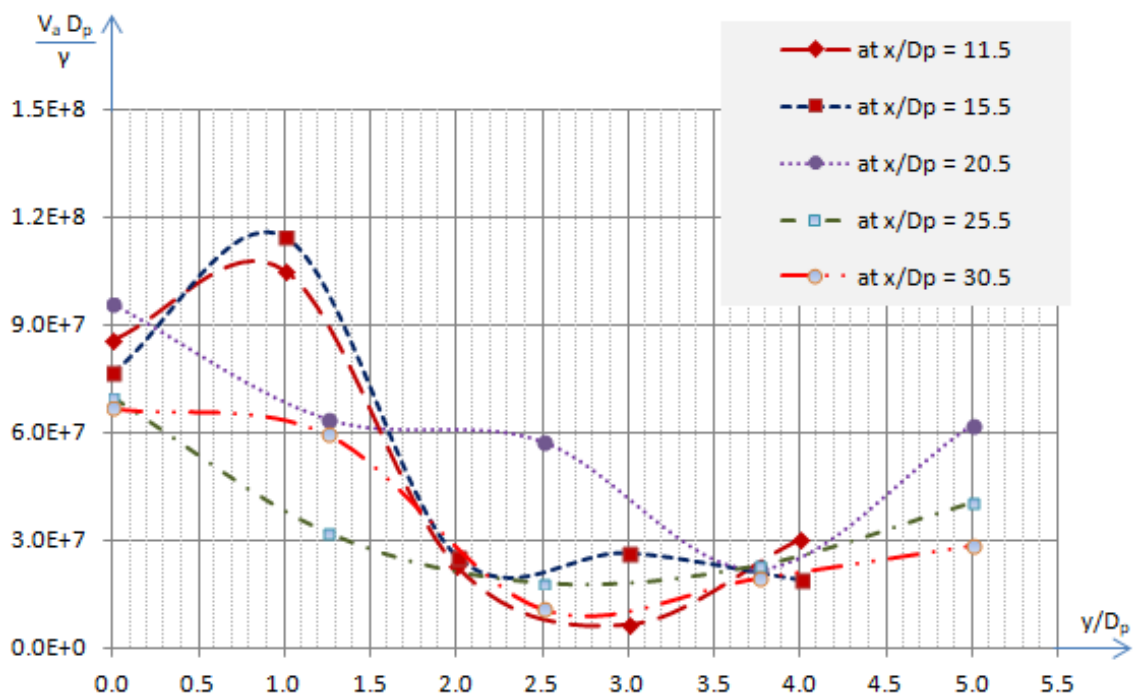


Figure D8: Mean axial velocity with  $y/D_p$  at  $x/D_p = 11.50, 15.50, 20.50, 25.50$  and

$30.50$ ; for  $n = 9$  rps,  $\theta = 4.5^\circ$ , and  $H = 500$  mm

## Appendix 'E' – Certificate of Calibration for EMCM Package



## CERTIFICATE OF CALIBRATION

Certificate Number: 47639

Issued: 21/12/2016

Customer Details:

McQuest Marine Sciences Ltd  
 489 Enfield Road  
 Burlington  
 Ontario  
 T7T 2X5  
 Canada

Instrument Details:

Model: 0802 5.5 Discus DUAL

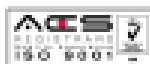
Serial Number: 57336

Traceability:

The instrument has been calibrated and found to be within our published specification at all measured points. A results sheet is attached. All measurements taken are traceable to national standards through the following equipment:

Hewlett Packard 34401A Digital Multimeter  
 Serial number: US36049071  
 Certificate number: C21976A

Calibrated on 20/12/2016 by A. Cox

Signed: 

Valeport Limited, St. Peter's Quay, Totnes, Devon, TQ9 5EW UK  
 Tel: +44 (0)1803 899202 Fax: +44 (0)1803 899203  
 E-mail: sales@valeport.co.uk Web: www.valeport.co.uk

VAT No: GB 165 6753 67 Registered in England No: 1950444

